

**Inferring Cerebral White Matter
Fibres from Diffusion Tensor
Magnetic Resonance Images**

Chengliang Hu

Doctor of Philosophy

University of York

Computer Science

August 2018

Abstract

The dissertation presents the research work on the inference of cerebral white matter fibres from diffusion tensor MR images. It also describes some preliminary work on sulci characterisation in structural MR images, in order to explore the graph based methods for shape analysis. The methodology is subsequently extended to diffusion MRI analysis. The overall research involves computer vision and statistical pattern recognition techniques.

We propose a framework for inferring white matter fibres from diffusion MR images. Graph based methods are used to represent the diffusion MR images and to extract features. Feature selection and machine learning techniques are used for the classification of the white matter fibres. An evaluation of the methodology is conducted.

In the white matter fibre inference, four similarity measures are adopted for fibre classification, namely the Riemannian affine invariant metric and Log-Euclidean metric; and the proposed shape-angle measure and the heuristic method. Among them, the heuristic method achieves the best average classification rates. On an average, they are 74.58% using one brain, 85.56% using two brains and 87.86% using three brains, based on diffusion tensor MR images.

As a preliminary study, we also propose a framework for sulci characterisation. Graph based methods are explored; and the average classification accuracy rate in 30 runs is 86.56% using the heat kernel signature, and it is 87.33% using the zeta function traces.

Contents

1	Introduction	16
1.1	Background	16
1.2	Aim and motivation	19
1.3	Research questions	20
1.4	Contributions	21
1.5	Methodology	22
1.6	Overview of the dissertation	23
1.7	Summary	24
2	Literature Review	25
2.1	The anatomy of the human brain	26
2.2	Neuroimaging modalities	28
2.3	Magnetic resonance imaging	30
2.3.1	Diffusion MRI	31
2.3.2	Diffusion tensor MRI	32
2.4	Statistical pattern recognition for shape analysis	34
2.5	Graph theory for shape analysis	36
2.5.1	Shape descriptor	37

2.5.2	Dissimilarity measurement	39
2.5.3	Graph theory in medical image analysis	40
2.6	Shape analysis in non-Euclidean space	41
2.7	Summary	43
3	Characterising the Sulci in Structural MR Images	45
3.1	The sulci of the human brain	46
3.2	Methodology of the sulci classification in MR images	46
3.2.1	MRI data and preprocessing	47
3.2.2	Graph representation and sampling	48
3.2.3	Spectral graph theory and Laplacian matrix	49
3.2.4	Graph characterisation using heat kernel signature	53
3.2.5	Graph characterisation using zeta function trace	55
3.2.6	Graph characterisation using zeta function derivative at the origin	58
3.3	Principal component analysis	58
3.4	Linear discriminant analysis	59
3.5	Sulci classification and evaluation	62
3.6	Results of sulci classification	64
3.6.1	The confusion matrix	64
3.6.2	Classification using heat kernel signature	65
3.6.3	Classification using zeta function trace	66
3.7	Summary and discussions	66
4	Shape Analysis for Diffusion MR images	69
4.1	Theory and concepts of diffusion MRI	70

4.1.1	Diffusion MR imaging	70
4.1.2	The diffusion tensor	71
4.1.3	Diffusion tensor estimation	72
4.1.4	Parameters derived from the diffusion tensor	73
4.1.5	Riemannian geometry	75
4.1.6	The connection structure	76
4.1.7	Exponential and logarithmic maps	77
4.1.8	Riemannian metrics and other measures	77
4.1.9	Spectral graph theory	81
4.1.10	Support vector machine	82
4.2	Methodology for diffusion MRI analysis	84
4.2.1	The HARDI data	84
4.2.2	Data transformation from HARDI to DTI images	85
4.2.3	Diffusion tensor visualisation	86
4.2.4	Extracting quantitative parameters from DTI	86
4.3	Tests: the brain structure detection	91
4.3.1	The effects of graph size	99
4.3.2	Distribution of voxelwise geodesic distances in DT-MR images	101
4.4	Conclusion	102
5	Feature Selection for Inferring White Matter Fibres from DTI	107
5.1	Contributions	108
5.2	An outline for inferring the white matter fibres from DTI	108

5.3	The detailed framework of inferring white matter fibres from DTI	110
5.3.1	The HARDI data and samples	110
5.3.2	Semi-automatic sample labelling	111
5.3.3	Feature extraction from the elementary symmetrical polynomials	113
5.3.4	Feature selection	120
5.3.5	Machine learning and SVM classification	123
5.3.6	Cross validation of the SVM	123
5.4	Exploring geometric relationship of the tensors	124
5.4.1	Test 1: Shape-angle distance vs. affine invariant distance	125
5.4.2	Test 2: The effects of changing the angle of the tensor .	127
5.4.3	Test 3: The effects of the ratio of eigenvalues	130
5.4.4	Test 4: Affine invariant metric vs. shape-angle measure	132
5.5	Summary	134
6	Evaluation of Methodology for Inferring White Matter Fibres	136
6.1	Datasets and experiment design	137
6.2	Selection of samples	138
6.3	Training of SVM models	140
6.3.1	Choosing parameters	140
6.3.2	Ten-fold cross validation	145
6.4	Testing of SVMs on the unseen data	151
6.5	Experimental methods	151
6.6	Results	153

6.7	Summary	160
7	Conclusion and future work	164
7.1	Summary of contributions	166
7.2	The factors that could affect the inference of white matter fibres	168
7.3	Future work	170
	Appendices	172

List of Tables

3.1	Mean and standard deviation of three types of features: the second eigenvalues, the first moment of zeta function trace values, and the derivatives of the zeta function.	58
3.2	A confusion matrix for two-class classification	64
3.3	Results of classification using HKS features.	65
3.4	Results of classification using zeta function trace features. . . .	66
6.1	Data Description	137
6.2	One-Brain Case 1: Training and testing both using Dataset1 .	154
6.3	One-Brain Case 2: Training and testing both using Dataset2 .	154
6.4	One-Brain Case 3: Training and testing both using Dataset3 .	154
6.5	One-Brain Case 4: Training and testing both using Dataset4 .	155
6.6	One-Brain Case 5: Training and testing both using Dataset5 .	155
6.7	Two-Brain Case 1: Train: Dataset2; Test: Dataset3	156
6.8	Two-Brain Case 2: Train: Dataset2; Test: Dataset4	156
6.9	Two-Brain Case 3: Train: Dataset3; Test: Dataset4	157
6.10	Two-Brain Case 4: Train: Dataset3; Test: Dataset2	157
6.11	Two-Brain Case 5: Train: Dataset4; Test: Dataset2	158
6.12	Two-Brain Case 6: Train: Dataset4; Test: Dataset3	158

6.13	Three-Brain Case1:Train:Dataset2+Dataset3;Test:Dataset4 . .	159
6.14	Three-Brain Case2:Train:Dataset2+Dataset4;Test:Dataset3 . .	159
6.15	Three-Brain Case3:Train:Dataset3+Dataset4;Test:Dataset2 . .	160

List of Figures

1.1	Differences of animal bone shapes	17
1.2	An illustration of the white matter tracts in human brain . . .	19
2.1	White matter in the human brain	26
2.2	Brownian motion of extracellular water molecules and inside the cells	31
2.3	Königsberg seven bridges and a graph	37
3.1	The sulci of the human brain.	47
3.2	A regular graph representing an image of 3×3 pixels	48
3.3	A regular graph representing $3 \times 3 \times 2$ MR images.	49
3.4	The coordinates of a point in 3D MR images are chosen at the cross hair position (3 views).	50
3.5	The second smallest eigenvalues of 100 graphs derived from the 100 samples.	52
3.6	The t interval value used during the heat kernel signature value production.	55
3.7	The zeta function trace values of the first moment.	57
3.8	The zeta function derivative values at origin.	59

3.9	Projected heat kernel signature values using PCA.	60
3.10	Projected zeta function trace values using PCA.	60
4.1	Diffusion tensor shapes	74
4.2	The connection structure for a manifold.	76
4.3	Exponential and logarithmic maps.	77
4.4	Image transformation: from diffusion-weighted MR images to diffusion tensor image.	85
4.5	A diffusion tensor image of the human brain (axial view) . . .	87
4.6	A diffusion tensor images of the human brain; (a) coronal view and (b) sagittal view.	88
4.7	(a) A fractional anisotropy (FA) image; (b) A mean diffusion (MD) image.	90
4.8	A brain MR image overlaid by the principal eigenvectors of the tensor and the FA values (axial view).	91
4.9	A brain MR image overlaid by the principal eigenvectors of the tensors and FA values (coronal and sagittal views).	92
4.10	Left: A sequence of diffusion tensor images of corpus callu- son(slices 60-64, sagittal); Right: their second eigenvector im- ages.	94
4.11	Left: A sequence of diffusion tensor images of corpus calluson (slices 65-69, sagittal); Right: their second eigenvector images.	95
4.12	Left: A sequence of diffusion tensor images of corpus calluson (slices 20-23, axial); Right: their second eigenvector images.	96
4.13	A diffusion tensor image of the ventricle and its first 5 eigen- vectors' images	97

4.14	The shape-angle measure is used for computing the pairwise distances between the tensors.	98
4.15	Tensor distance maps and histograms, based on the tensor image of the CSF.	103
4.16	Tensor distance maps and histograms, based on the tensor image of the background.	104
4.17	Tensor distance maps and histograms, based on the tensor image of the CSF in part and its background.	105
5.1	A label map and an associated tensor image (Dataset2). Three diffusion tensor images are used to create the label map. . . .	114
5.2	A histogram of the log10 eigenvalues of the covariance matrix of the feature data matrix.	119
5.3	The relationship between geodesic distance and the angle of pairwise tensors of a data graph. The affine invariant Riemannian metric is used to compute the tensor distance.	125
5.4	The relationship between geodesic distance and the angle of pairwise tensors of a data graph. The shape-angle measure is used to compute the geodesic distance of paired tensors. . . .	126
5.5	The relationship between the affine invariant distance and the shape-angle distance, different measures are used.	127
5.6	Tensors in the circular field.	128
5.7	The second and the third eigenvalues vs. radial distance along the X-axis.(a) without adding noise; (b) Gaussian noise is added to the eigenvalues(sd.0.005).	129
5.8	A map of the ratio values of eigenvalue1 to eigenvalue2	131

5.9	A map of the ratio values of eigenvalue1 to eigenvalue3	131
5.10	A map of the ratios of eigenvalue2 to eigenvalue3	132
5.11	The curves show the changing geodesic distance, measured by Pennec’s affine invariant metric.	133
5.12	The tensor distance computed by the shape-angle measure. . .	134
6.1	The characteristics of the samples from dataset5.	141
6.2	Choosing parameters with affine invariant metric.	143
6.3	Choosing parameters with Log-Euclidean metric.	143
6.4	Choosing parameters with Shape-Angle measure.	144
6.5	Choosing parameters with Heuristic method.	144
6.6	A diagram of ten-fold cross validation.	145
6.7	Ten-fold cross validation in SVM training: the affine invariant metric is used for tensor distance measure.	147
6.8	Ten-fold cross validation in SVM training: the Log-Euclidean metric is used for tensor distance measure.	148
6.9	Ten-fold cross validation in SVM training: the shape-angle measure is used for tensor distance measure.	149
6.10	Ten-fold cross validation in SVM training: the heuristic method is used for tensor distance measure.	150
6.11	Features generated from the elementary symmetric polynomi- als, derived from spectral graph theory.	163

Acknowledgements

First, I would like to thank my supervisor, Prof. Susan Stepney, for her support and helpful advice on my research and writing up. I am very grateful for her constructive comments on my dissertation and encouragement.

I want to thank my former supervisor, Prof. Edwin Hancock, for his valuable advice and expertise in the graph theory and statistical pattern recognition, and directing me during my early research.

My sincere thanks goes to Dr. Nick Pears, Dr. Fiona Polack and Prof. Jiancheng Sun for their advice and discussions.

Special thanks are due to my examiners Prof. Xiaohong Gao and Dr. Daniel Kudenko for their time, assessment and comments.

Appreciation goes to Prof. Gary Green and Prof. Tony Morland, of the York NeuroImaging Centre, for providing me the MRI datasets used in this research, and for permitting me to use their research facilities.

Many thanks to Prof. Tim Andrews, Department of Psychology, the University of York, for accepting me to attend his Cognitive Neuroscience lecture course, and allowing me to attend a dissection class to explore the human brain.

I am grateful to the Department of Computer Science for supporting me

to attend the 2014 International Medical Imaging Summer School held in Sicily, Italy, where I enjoyed many inspiring lectures given by experts in medical image analysis, especially that by Prof. Michael Brady and Dr. Xavier Pennec.

Finally, my heartfelt thanks go to my family, for their love, support and encouragement.

This dissertation is dedicated to my late parents.

Declaration

I declare that this thesis is a presentation of original work and I am the sole author. This work has not previously been presented for an award at this, or any other, University. All sources are acknowledged as References.

List of Abbreviations

MRI	Magnetic Resonance Imaging
DWI	Diffusion Weighted MRI
DTI	Diffusion Tensor MRI
DT-MRI	Diffusion Tensor MRI
HARDI	High Angular Resolution Diffusion-weighted Imaging
FA	Fractional Anisotropy
HKS	Heat Kernel Signature
SNR	Signal to Noise Ratio
SVM	Support Vector Machine
ESP	Elementary Symmetric Polynomial
SFS	Sequential Forward Selection (algorithm)

Chapter 1

Introduction

1.1 Background

The main theme of this dissertation is the inference of the white matter fibres in diffusion tensor magnetic resonance (MR) images of the brain. It starts with a preliminary study on the sulci characterisation in structural MR images, exploring the feasibility of using graph based methods.

This chapter describes the core concepts of shape analysis and medical imaging techniques, the aim and motivation of the research, and the structure of the dissertation.

We live in the world surrounded by objects: trees, buildings, cars and people, etc. The geometry of an object is known as a shape. A shape can be represented by identifiable points known as landmarks. An object can be depicted by a boundary model using points, curves or surfaces, or a transformation model like splines or a graph. A structure of the brain is considered as a shape, too.

The study of shape and structure is a fundamental topic in computer vision and pattern recognition. Kendall gives a definition in mathematical terms: shape is “what is left when the differences which can be attributed to translations, rotations, and dilations have been quotiented out” [40]. Human vision is capable of recognising shapes, no matter how they are arranged, projected and even partially occluded. Computer vision aims to replicate such a remarkable functionality of the human vision system to some extent.

The concept of shape was realised early in scientific research. In 1638, Galileo [36] illustrated the difference in shape of the bones of small and large animals (Fig.1.1).

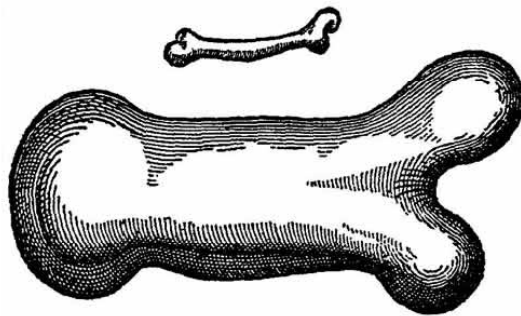


Figure 1.1: Differences of animal bone shapes [36]

Shape analysis plays an important role in object classification and scientific research. For example, the shapes of human skulls assist archaeologists to identify the races and time; and the shapes of leaves can identify certain plant species [32]. In neuroscience, a change in brain structure could be an indicator of neural degeneration or a damage. Early diagnosis is crucial for a better treatment response and prognosis. For instance, cerebral atrophy, enlarged ventricles are associated with Alzheimer’s disease. In psychiatry, studies suggest that white matter diseases and unusual neural fi-

bre organisation are linked to abnormal human behaviors[61][49]. As Crow states, “schizophrenic symptoms have their origin in the variations in inter-hemispheric connections”[24].

The detection of white matter fibres is not trivial. Before magnetic resonance imaging MRI was invented in the 1980s, invasive methods were applied for the detection. For example, postmortem dissections were used to find the white matter tracts [18]. In 1795, Johann Reil (1759-1813), Professor of anatomy, developed a method based on soaking a specimen of the human brain in alcohol to make it easier for dissections [58]. He found the white matter bundles running beneath the major convolutions of the brain, which were confirmed by Karl Burdach a decade later. Reil and Burdach discovered a number of major white matter tracts, laying a foundation of neuroscience. Theodor Meynert (1833-1892), Professor of psychiatry, further advanced the discoveries and associated the white matter tracts with brain function and mental illness. Meynert also categorised the white matter fibres as *project* fibres that consist of ascending and descending pathways arising and terminating in the cortex, *commissural* fibres connecting cortex between the cerebral hemispheres, and *association* fibres connecting cortical regions within a hemisphere [50]. These studies were conducted on cadaver brains. Some of the neural fibre tracts are illustrated in Figure 1.2.

The first water self-diffusivity measurements using nuclear magnetic resonance were reported by Carr and Purcell in 1954 [16]. This led to the discovery of diffusion MRI in the mid-1980s, also its successful application to tissue characterisation [66]. Diffusion MRI can be used for noninvasive examination of the living brain, called *in vivo*. Derived from diffusion MRI,

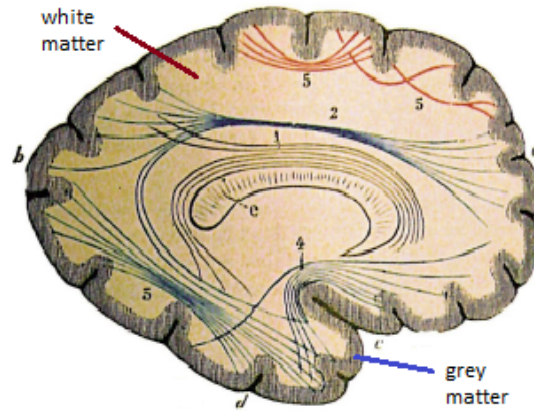


Figure 1.2: An illustration of the white matter tracts in human brain, showing the U-shaped fibres (red) and the long association bundles (blue). [18].

diffusion tensor MR images provide new means to explore tissue structure at different levels of hierarchical human brain organisation.

In structural MR images, the white matter is shown as a uniform grey mass, no white matter fibres can be seen. To exploit fully the potential of diffusion MRI, and provide a new paradigm of characterising white matter fibres, this dissertation describes how white matter fibres can be inferred by using computer vision, statistical pattern recognition, and machine learning (Chapters 4-6). These techniques are initially used for the characterisation of the sulci in the simpler case of T1-weighted MR images (chapter 3).

1.2 Aim and motivation

The first mathematical model of diffusion MRI was proposed by Basser et al. in 1994 [7]. It provides useful geometrical information for quantitative measurements of the three-dimensional anisotropy in tissues.

However, the diffusion model has its limitations. It assumes a single diffusing process that propagates in time and space in a Gaussian manner, which does not reflect reality. This can result in inaccurate quantitative measurements. The diffusion model is also unable to deal with the white matter fibre crossing problem, but the diffusion model itself is not the subject of this study.

Furthermore, partial volume effect exists in MR images, meaning multiple types of tissues and/or multiple white matter fibres occupy one image voxel. Given these obstacles, this study aims to find a way of characterising white matter fibres, using the geometric information derived from diffusion tensor MR images.

The aim of this research is to develop a graph based framework for the inference of the cerebral white matter fibres from diffusion tensor MR images, and develop novel shape descriptors to produce features for machine learning and MR image analysis. A preliminary study on sulci detection in structure MR images is also conducted.

The motivation is to assist the diagnosis of neurological diseases and psychiatric disorders related to the white matter fibres, and presurgical planning. The primary goal of the research is to develop a workable framework and creating shape descriptors for inferring white matter fibres from diffusion MRI.

1.3 Research questions

The research questions are

- (1) can spectral graph approaches and machine learning methods be used

for sulci characterisation? if so, how to establish a framework for that?

(2) can spectral graph approaches and machine learning methods be extended for the white matter fibre inference? if so, how to establish a framework for that?

(3) can feature selection be used for the white matter fibres classification on a manifold? if so, how to select the best features? and what is the optimal number of features?

1.4 Contributions

The contributions described in this dissertation are

(1) proposing a novel graph based framework of characterising the sulci in structural MR images of the brain, and creating useful features, from both the heat kernel signature and the zeta function trace, for discriminant analysis classification.

(2) proposing a novel graph based framework of inferencing white matter fibres from diffusion MR images of the brain, and creating useful features from the elementary symmetric polynomials for the inference of white matter fibres.

(3) using a feature selection method for the white matter fibre classification on manifolds; with small numbers of features, optimal classification results are achieved.

(4) developing a semi-automatic system for the diffusion tensor sample labelling.

(5) evaluating the methodology of the inference of white matter fibres us-

ing real diffusion MR images. With small numbers of datasets, the evaluation proves that the methodology is useful.

1.5 Methodology

The research work begins with a preliminary study for the characterisation of the sulci in structural MR images, to gain insight into how well the graph based approaches work for MR image analysis. After a successful trial, the methodology is then extended to the inference of the white matter fibres in diffusion tensor MR images.

The methodology of this research includes

(1) statistical shape analysis. The structural MR images (sMRI) are analysed in Euclidean space; while the diffusion tensor MR images (DT-MR) are analysed on the Riemannian manifold, where angular data can be expressed and computed properly. This is needed because diffusion tensor images have both magnitudes and angles.

(2) spectral graph theory is used for shape representation and analysis. The heat kernel signature and the zeta function are used as features extracted from structural MR images, while symmetric elementary polynomials are used as features, extracted from diffusion tensor MR images.

(3) Linear discriminant analysis is applied to the sulci classification, while feature selection and support vector machine (SVM) are used for the fibre classification, while linear discriminant analysis is applied to the sulci classification.

1.6 Overview of the dissertation

The structure of the dissertation is:

Chapter 2 is a review of the literature. The first part is about the theoretical aspects, such as the anatomy of the human brain, MR physics, diffusion MRI, graph theory, and machine learning. The second part reviews the related methodologies, including shape analysis techniques for diffusion MRI, especially those for inferring the white matter fibres and detecting the sulci.

Chapter 3 presents a preliminary study, concerning the detection of the brain sulci in structural MRI. Both the heat kernel signature and the zeta function trace are used to extract features respectively. The results of classification are presented.

Chapter 4 presents the experimental work on inferring white matter fibres from diffusion tensor MR images. It describes the work on exploring the properties of diffusion MRI, which could be useful for the white matter fibre inference.

Chapter 5 describes a framework for the inference of white matter fibres from diffusion tensor MRI. Elementary symmetric polynomials are used to extract features. Feature selection and support vector machine are used for classification. The results of fibre classification are shown and analysed.

Chapter 6 presents an evaluation of the methodology used to infer the white matter fibres, which is conducted on real diffusion tensor MR images of several brains.

Chapter 7 is a conclusion, discussions and the future work.

1.7 Summary

This chapter describes the context of research and some core concepts. It also describes the aim and the motivation of the research, as well as the contributions, and the structure of the dissertation.

The research concerns the inference of the white matter fibres from diffusion tensor MR images, driven by its medical relevance. We believe that the research outcomes not only can be applied to deepen our understanding of the human brain, but also benefit neurological and psychiatric studies.

Chapter 2

Literature Review

The goal of the research is to characterise the white matter fibres in diffusion MR images. White matter fibres cannot be detected directly, however they could be inferred by diffusion tensor image analysis.

As a preliminary study, the characterisation of the sulci in structural MRI is also explored. The related work is first reviewed briefly.

To appreciate the related state-of-the-art methodologies and to identify the gaps in MRI research, a review of literature is presented. It covers the following main topics:

1. The anatomy of the human brain, which introduces the sulci and the white matter fibres.
2. Neuroimaging modalities, leading to the importance of magnetic resonance imaging, especially diffusion MRI and structural MRI.
3. Statistical pattern recognition, focusing on structure detection and classification in image analysis. This includes feature selection and machine learning.

4. Spectral graph theory for shape analysis.

2.1 The anatomy of the human brain

The human brain is the most complex organ in the body. Brain structures vary in shape across individuals. Hence the detection and classification of brain structures are technically demanding. The human brain comprises of the white matter, grey matter and the cerebrospinal fluid (CSF).

The brain has around 100 billion neurons [10], which are the most important cells of the central nervous system. A neuron is an electrically excitable cell that receives, processes and transmits information through electrical and chemical signals. It has the main cell body, a bundle of axon or white matter fibres and a branch of synapses (Fig.2.1). Neurons are linked together electrically and chemically through synaptic connections, which form the neural network that allows information passing. In short, neurons sense the changes, communicate the changes to other neurons and command the body's responses to these sensations[10].



Figure 2.1: White matter in the human brain [75].

Figure 2.1 (left) shows the structure of a neuron. It consists of the cell

body with the nucleus, the synaptic terminals for inputting signals, the axon for conducting signals, and the dendritic branches for outputting signals. The axon is known as the white matter fibre, which is 5-10 micrometer (μm) in diameter. Figure 2.1 (right) shows that neurons are wired together by the axons. White matter fibres in an image element (voxel) are referred as a fibre bundle.

White matter fibres enable the communication of different regions of the brain, receive information and control the biological systems in the human body. The white matter fibres develop over a person's lifetime. They can be damaged by brain injuries, diseases and ageing.

The neural network plays an important role in normal cognition, perception and motor skills. Any damage to the neural network can have devastating consequences, such as schizophrenia[35]. Currently, little is known about human brain connectivity. Therefore the identification of the white matter fibres in medical images is crucial for neuroscience in general, and for brain connectivity studies in particular.

This identification is a long-standing and challenging task, due to the large number of regions, pathways and individual variability in the brain anatomy, and also the complex relationship between region and interregional connectivity, as well as the limitations of neuroimaging technologies and image analysis methods.

2.2 Neuroimaging modalities

Neuroimaging is used to examine the brain structures, in order to develop effective therapeutic interventions, and improve our ability to correlate behavioural deficits with structural or functional dysfunction.

For different purposes, a number of neuroimaging modalities have been used for imaging the brain, such as computed tomography (CT), positron emission tomography (PET), electroencephalography (EEG), magnetoencephalography (MEG), and magnetic resonance imaging (MRI)[10].

CT captures a series of X-ray images of the head from different directions. It produces good quality images of the brain within a few minutes. A CT scan is able to show swelling from tissue damage in the brain, bleeding and the ventricle size. It is often used in an emergency as a diagnostic imaging modality for head trauma, stroke and haemorrhage, due to its accuracy, reliability, safety and wide availability.

PET is a functional imaging modality that produces three dimensional images of the body. It requires a positron-emitting radionuclide (tracer) to be injected into the body to enable the concentrations of tracer to be detected, which reflects the tissue metabolic activity. This is useful for assisting tumor and cancer diagnosis.

EEG is the recording of the brain's spontaneous electrical activity in the scalp over time (20-40 minutes). It is primarily used to diagnose epilepsy, sleep disorders, coma and brain death.

MEG is a functional neuroimaging technique that records the magnetic field produced by electrical currents occurring naturally in the brain. MEG is used for determining the function of different regions of the brain, so it is also

called functional MRI (fMRI). fMRI measures blood-oxygen-level dependent (BOLD) signals which reflect the brain activity [37].

MRI includes structural MRI (sMRI), diffusion MRI (dMRI) and functional MRI. sMRI shows the general appearance of the anatomical structures in the brain, such as the ventricles, grey matter and white matter. However, the white matter fibres cannot be seen in MR images.

Diffusion MRI (dMRI) is able to capture the diffusion process of water molecules in biological tissues *in vivo* and noninvasively. The intensity of each image element (voxel) reflects the best estimate of the rate of water diffusion at that location. In the early days, dMRI was used to detect acute brain ischemia successfully [52]. Later it has been used for cancer detection and the investigation of the brain connectivity, in order to understand certain brain diseases and neurological disorders [29].

These imaging modalities offer opportunities for us to deepen our understanding of the human brain. They have advantages and disadvantages. EEG equipment cost is low but it cannot detect electrical signals in the deep brain. PET and fMRI can measure localised changes in cerebral blood flow that is related to neural activity, but PET requires positron-emitting radioisotopes with short half-lives, produced by a cyclotron close to the PET imaging facility. EEG and MEG have high temporal resolution when measuring brain activity, but it is difficult to localise that activity. fMRI is better at localising brain activity with good spatial resolution, but provides little information about temporal interactions between the brain regions. These imaging modalities are complementary. For example, in the human connectome project, fMRI, dMRI, MEG and EEG data are all used to char-

acterise the brain function and connectivity, and their variability in healthy adults[70].

For shape analysis of the human brain, structural MRI and diffusion MRI provide more superior and relevant information. Diffusion MRI is unique in probing water diffusion in tissue micro structure, so it can be used to infer the white matter fibers in the living brain.

2.3 Magnetic resonance imaging

In 1945, nuclear magnetic resonance (NMR or MR) was discovered by Purcell et al.[56]. In the following year, Bloch et al. independently investigated nuclear induction and nuclear magnetic resonance [14]. Purcell and Bloch received the 1952 Nobel Prize in Physics for their work on nuclear magnetic induction.

In 1973, Lauterbur proposed the mathematical formation for MR images [42]. In 1977, Mansfield created the slice selection imaging technique for spin based MRI [46]. The following year, Mansfield produced the first MR images of the whole live human body successfully[47]. Lauterbur and Mansfield jointly won the Nobel Prize in Physiology or Medicine in 2003, for the development of magnetic resonance imaging. This is one of the most important breakthroughs in modern medicine.

The principles of MRI are described as follows: The human body consists of around 65% water; when the body is placed in a strong and highly uniform magnetic field, interactions of the protons (namely hydrogen-1 nuclei) of the water within the body and the magnetic field occur. The spins of the

protons of free water generate the signal of a tissue. After a high radio frequency pulse is applied to excite the spins, the incurred net magnetisation starts to precess around the main magnetic field with a resonant frequency [72]. Then the MR signals are amplified and collected for the MR image reconstruction. By using different imaging protocols, or sequences, a variety of MR images with different image contrast can be generated, and certain tissues and structures can be emphasised. For example, T1-weighted MR images show detailed tissues and bone structures, while T2-weighted MR images depict fluid, ligaments and fatty tissues very well.

2.3.1 Diffusion MRI

Diffusion MRI is a type of magnetic resonance imaging, related to water diffusion. In 1827, Robert Brown first noticed particles of pollen floating in water moving randomly [15]. It was named as Brownian motion (Fig.2.2). In 1905, Albert Einstein explained the molecular diffusion, based on the random motion of molecules caused by their thermal energy.

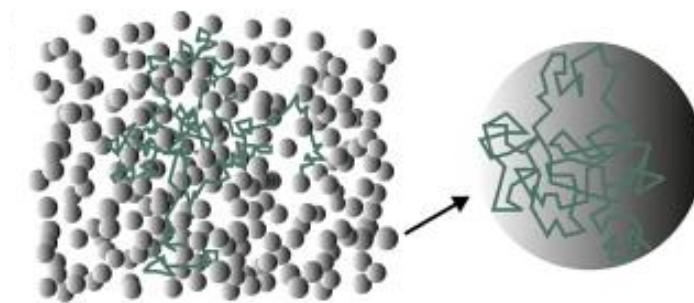


Figure 2.2: Left: Biological cells may hinder the Brownian motion of extra-cellular water molecules; Right: Inside each cell, diffusion may be restricted by the cellular membranes [8].

In 1985, the pioneering work of Le Bihan and Breton showed that water diffusion in the brain could be imaged through magnetic resonance imaging, and that water diffusion could provide unique information on the tissue architecture [29]. These are the principles of diffusion nuclear magnetic resonance.

In 1990, Moseley et al. discovered that water diffusion in white matter fibres was anisotropic, faster in the direction of the fibres and slower perpendicularly to them [52]. The experiments were carried out on cats. These discoveries established the theoretical foundation of inferring the existence of neural fibres in the human brain by examining the rate of water diffusion [28].

In 1994, Basser et al. proposed the first mathematical model of diffusion MRI[7]. It can be used to extract fibre direction in the brain images, but fails in regions containing multiple fibre orientations. The limitation of the model is due to the fact that it describes a white matter population in one voxel, and assumes a single Gaussian diffusion compartment for each voxel. Therefore, it is unable to adequately describe diffusion functions when there are white matter crossings [69]. Several studies have been conducted to improve the diffusion model, but this has not been successful[28]. The limitation could affect the inference of the white matter fibers.

2.3.2 Diffusion tensor MRI

To determine the true direction of the highest diffusivity properly, Basser et al. published their experimental work on diffusion tensor imaging (DTI)[7]. DTI is a special form of diffusion MRI, it can be mathematically transformed

from diffusion-weighted MR images.

In a diffusion tensor image, every image element (voxel) is a positive definite tensor, defined as a 3×3 symmetric matrix. The tensor is depicted by an ellipsoid, or a sphere in a special case. The tensor can be decomposed to produce 3 eigenvalues and 3 eigenvectors. The eigenvalues describe the axis lengths of the ellipsoid, while the eigenvectors indicate the directions of the 3 perpendicular axes [1]. The tensor has both magnitude and orientation. The direction of the longest axis length is indicated by the principal eigenvector, which determines the orientation of the tensor.

Diffusion tensor images contain information about the orientation of cerebral white matter fibres, it can be used to study human brain connectivity, which can be visualised by DTI fibre tractography [68]. DTI fibre tractography can produce coherently ordered fibre tract trajectories within the brain. This is based on the idea that in ordered fibrous tissues, the eigenvector associated with the largest eigenvalue within a voxel is parallel to the local fibre direction [7]. There are deterministic tractography and probabilistic tractography. For the former, the streamline tractography algorithm integrates voxelwise fibre orientations into fibre pathways [51]; the seed point is required and error propagation can occur. For the latter, the accuracy of the probability distribution model can be affected by the diffusion from non-principal orientations [39]. There is high uncertainty in the principal diffusion direction where fibre crossing exists. Image noise can also affect the DTI fibre trajectories [11].

Algorithms were developed at the end of 1990s to enable fibre tracking by connecting those tensor voxels. However, fibre tracking is not the goal

of this study. As stated, this dissertation focuses on the inference of the white matter fibres. We hope that the combination of new shape descriptors derived from diffusion MR images, feature selection and machine learning techniques could create a new paradigm for the characterisation of the white matter fibres.

2.4 Statistical pattern recognition for shape analysis

Statistical pattern recognition, especially together with machine learning, is a powerful paradigm for shape analysis. The theories are expressed by Devijver and Kittler [26].

Statistical learning theories [71] state:

- (a) in some instances mathematical models can be derived from the data, as the variability of the pattern representation;
- (b) statistical distributions are often used as a model for the pattern generation, and the classification problem can be treated as a test of hypothesis, or a special case of the statistical decision theory problem;
- (c) statistical decision theory applies statistical decision functions, their merits and optimality criteria.

There are limitations to the theories. The outcomes of classification usually are a clear-cut (yes or no) answer, and it is therefore unable to deal with contextual or structural information. For this reason, some conditions are specified for a classification task. For example, the distance between two

pattern representations, as a similarity measurement, is usually integrated into a decision making process in machine learning. This assumes that a one-to-one relationship between the condition and the similarity exists, but this is not realistic in some circumstances.

Statistical pattern recognition is useful for detecting anatomical structures in medical images. It is sometimes related to statistical shape modeling. In 1992, Cootes et al. proposed the point distribution models (PDM) for shape variability modeling [22]. It assumes that points in a shape tend to move in a correlated way. A set of aligned shapes is then described by (1) finding the mean shape and the deviations from it; (2) calculating the covariance matrix of the data, and computing the eigenvalues and eigenvectors of the matrix; and (3) finding the modes of variation defined by eigenvectors. With a set of training images, geometric variability of the anatomical structures can be modeled through parameterisation. However, shape variations and image noise can make point-to-point correspondence difficult.

The work of sulci line automatic detection is described by Counce and Taylor in 2001[19]. Both the PDM and the active shape models (ASM) [21] are applied for statistical modeling. The ASM iteratively deforms to fit to an example of the object in a new image, while the iterative closest point (ICP) algorithm [12] is used to find the global alignment of the points and the specific point correspondences. Although these examples are about shape modeling, the use of the eigensystem is thought provoking.

Most work on statistical shape analysis has applied linear methods. The drawback is that the assumptions of multivariate Gaussian model cannot always be met. For instance, there is the intrinsic heterogeneity within the

tissue classes in the MR images. This imposes a difficulty in the process of statistical pattern recognition.

2.5 Graph theory for shape analysis

In the 18th century, the problem of the seven bridges of Königsberg led to the development of Eulerian graph theory and topology [31]. It was about finding a path through the seven bridges in the city and crossing each bridge once only. For this, a graph was produced in which each area serves as a node, and each bridge becomes an edge (Figure 2.3). In this example, an object or a scene is represented by a graph, which describes the relation between objects at an abstract level. This was the root of graph theory; a graph can be a mathematical model for analysing real world problems topologically, being used in physics, chemistry and medical images.

Relational graphs are an important representation of image structure in high level computer vision tasks [76]. In 1971, Barrow and Popplestone [6] described their seminal work on using a relational graph representation of the scenic structure. Since then graph representations for computer vision research have been flourishing. One of the advantages of using a graph based approach is that image processing relies on topological relations, rather than on exact scene measurements. However, the computation would be expensive when it is based on pairwise graph nodes.

With a graph representation, mathematical methods can be performed concisely. This is the rationale of using graph based approaches in this study, for the detection of the brain structures in MR images.

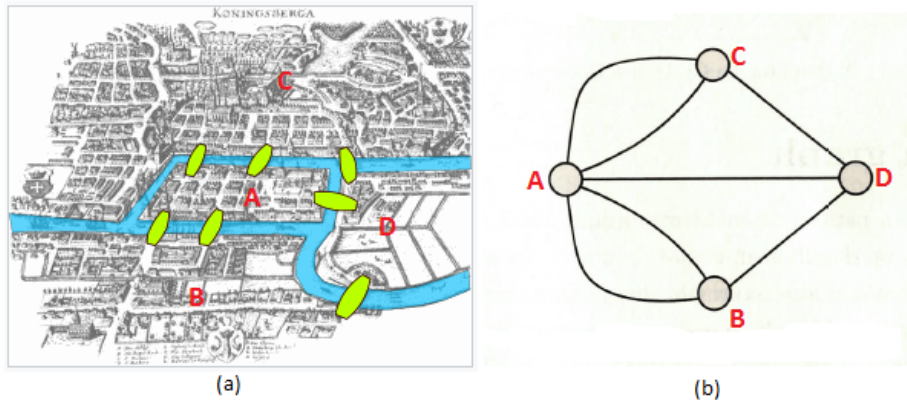


Figure 2.3: Königsberg seven bridges and a graph.(a) a map of Königsberg in Euler's time, with the Pregel River and seven bridges highlighted. Four areas are represented as A, B, C and D; (b) is a graph for (a). The nodes denote the four areas and the graph edges depict the seven bridges. Modified from en.wikipedia.org.

Graph characterisation refers to the study of graph properties, which is related to shape analysis. Graph properties have been explored in the literature. e.g. the heat kernel trace is used to specify the flow of information across a network [65], or on a manifold [79]. The solution to the heat kernel is computed by the exponentiation of the Laplacian eigensystem over time [60]. Graph approaches can be coupled with machine learning.

Next, we discuss three important aspects of shape analysis using graph theory: (a) shape descriptor; (b)(dis)similarity measurement; and (c) applications.

2.5.1 Shape descriptor

A shape descriptor contains geometrical information of the shape of an object, which is used for (semi)automatic object recognition in image analysis.

Some existing shape descriptors are:

Heat kernel signature

In 2009, Sun et al. proposed a shape descriptor called the *heat kernel signature* (HKS) to depict shape properties [65]. Geometric information is derived from the graph Laplacian matrix.

In 2011, Castellani et al. describe a new shape descriptor for brain structure classification in MR images [17]. The structures are characterised by pairwise dissimilarities. The local heat kernel values at each data point are used to construct a histogram, and the histograms from all the data points are merged into a feature vector, known as the global heat kernel signature (GHKS):

$$GHKS(M) = [hist(H_{t_0}(M), \dots, hist(H_{t_n}(M))]$$

where $H_{t_i}(M) = \{h_{t_i}(x, x), \forall x \in M\}$ and M is a manifold; and $hist(\cdot)$ is the histogram operator. This shape descriptor encodes the distribution of local heat kernel values. The Jensen-Shannon divergence is used as the dissimilarity measure on histograms. This method is, however, sensitive to image noises.

Zeta function trace

In 2009, Xiao et al. report that the trace of the zeta function can be used for graph characterisation[79]. Some useful permutation invariants are identified:

1. the trace of the heat kernel;
2. the heat content, which can be expanded as a power series in time; and

3. the derivative of the zeta function.

McKay also found that the derivative of the zeta function at the origin is linked to the number of spanning trees in a graph [48]. Ren et al. propose a spectral analysis method for graph characterisation, using the polynomial coefficients of Ihara zeta function [59].

Wave kernel signature

The heat kernel signature (HKS) has a limitation. It is dominated by information from low frequencies that describe the global properties of the shape, so that high precision shape analysis is difficult to achieve. To overcome this problem, Aubry et al. create the wave kernel signature as a shape descriptor [3]. The Schrödinger equation is used to express the temporal evolution of quantum mechanical particles.

In 2014, Furqan et al. developed the Gaussian wave packet to provide richer structural information, using the eigenfunctions of the edge based Laplacian matrix derived from the data [4]. The drawback is that the computational cost for the Laplacian matrix is much higher than that using vertex based methods.

2.5.2 Dissimilarity measurement

In computer vision, dissimilarity measures the difference of two shapes. Given a descriptor is formulated, the distance between two shapes can be computed as the distance between the associated descriptors.

Normalised weighted spectral distance

Konukoglu et al. proposed the normalized weighted spectral distance

(nWSD)[41]. For two closed bounded domains with smooth boundaries, $\Omega_\lambda, \Omega_\xi \subset \mathbb{R}^d$, their spectra are given as the sequences $\{\lambda_n\}_{n=1}^\infty$ and $\{\xi_n\}_{n=1}^\infty$ respectively.

Denote $\rho(\Omega_\lambda, \Omega_\xi) \doteq \left[\sum \left| \frac{1}{\lambda_n} - \frac{1}{\xi_n} \right|^p \right]^{\frac{1}{p}}$, where $p > d/2$,

The nWSD is defined as $\bar{\rho}(\Omega_\lambda, \Omega_\xi) \doteq \frac{\rho(\Omega_\lambda, \Omega_\xi)}{W(\Omega_\lambda, \Omega_\xi)} \in [0, 1]$

where $W(\Omega_\lambda, \Omega_\xi) \doteq \left\{ C + K \left[\zeta\left(\frac{2p}{d}\right) - 1 \left(-\frac{1}{2}\right)^{\frac{2p}{d}} \right] \right\}^{\frac{1}{p}}$

$\zeta(\cdot)$ represents the Riemannian zeta function, and C and K are the shape based coefficients. Noticeably, the nWSD contains the zeta function in W , using the shape information encoded in the Laplace spectra, and also the entire eigenvalue sequence. Thus, the geometrical information is better used than that of some other discrepancy measurements, e.g. the root-mean-square error (RMS).

2.5.3 Graph theory in medical image analysis

In medical image analysis, some graph based approaches have been proposed for classification and detection in MRI. Cocosco reports that the *minimum spanning tree* is used for brain tissue classification [20]. Crum describes a spectral clustering method for tissue classification in brain MRI [25], where a label fusion technique is proposed to reduce the errors of random labeling and image registration (alignment). Criminisi et al. propose the *random regression forests* for the automatic detection of anatomical structures in 3D CT scans. An information theoretic metric is used for the *regression tree learning* [23], but the computational cost can be very high, and the detection errors could be propagated from one level to the next.

2.6 Shape analysis in non-Euclidean space

Non-Euclidean space can be a manifold, or a curved surface. It is a topological space that is regarded as Euclidean space locally. Riemannian geometry is applicable to such a manifold; it plays an important role in many computer vision tasks, including shape analysis. Statistical characterisation of medical data is best modeled as elements of a Riemannian manifold [34].

Diffusion tensor images are suitable to be studied in non-Euclidean space, namely the Riemannian manifold. This is because the tensor resides on a curved manifold naturally, where its magnitude and the principal angle can be expressed conveniently. However, some standard statistical formula for shape analysis are no longer applicable, such as the mean, distance and variance. Therefore, “curved statistics” is needed.

In 2006, Pennec et al. proposed a Riemannian framework for tensor computing [55]. The initial intention was to deal with the negative eigenvalues in tensor computing and interpretation.

Here the tensor refers to a 3×3 symmetric positive definite matrix. The Riemannian manifold for the tensors is a convex half-cone space, where the conventional additive operation is not suitable.

For tensor computing, Pennec et al. define an affine invariant Riemannian metric. It is a continuous collection of scalar products (or norms) on each tangent space, where at least one minimising geodesic between any two points on the manifold exists [55]. The geodesic distance between two tensors D_1 and D_2 on the Riemannian manifold is denoted as

$$d_{D_1, D_2} = \|\log(D_1^{-\frac{1}{2}} D_2 D_1^{-\frac{1}{2}})\|_F,$$

where $\|\cdot\|_F$ refers to the Frobenius norm of a matrix.

In Riemannian geometry, the transformation between the manifold and the tangent space must be invertible, to ensure the tensor computing on both a manifold and the tangent plane is equivalent.

Let the vector $\overline{(pq)}$ be a vector of the tangent space at point p , such a vector may be identified to a point on the manifold using the exponential map $q = Exp_p(\overline{pq})$. Conversely, the logarithmic map is used to map almost any bi-point (p, q) into a vector $\overline{pq} = Log_p(q)$ of T_pM [30]. This suggests that the distance of two tensors can be computed on a manifold, as well as on the tangent plane.

The basic operation in Riemannian manifolds is the scalar product. The exponential map, or *Exp* operator, is for geodesic shooting parameterised by the initial tangent; while the logarithm map, or *Log* operator, is for unfolding the manifold in the tangent space along geodesics. They work in the local domain but can depict a shape in the global domain, although it is limited by the cut locus. Nevertheless, it covers the entire manifold if geodesically complete, meaning the geodesic shooting is within the boundary [55].

The following examples demonstrate image analysis in non-Euclidean space.

Zhang describes the smoothing of structural and diffusion MR images in the non-Euclidean space [80]. The heat kernel signature is applied. The Riemannian weighted mean is computed iteratively using the gradient descent algorithm.

Lenglet et al. develop a Riemannian framework for the white matter

connectivity mapping, using diffusion tensor MRI [45]. The MRI images are treated as a Riemannian manifold M , and the Laplace-Beltrami operator is applied on M . Then the diffusion properties are used to derive its geometry.

By using the facial surface normal data, Smith presents his work on face modeling using shape from shading techniques [63]; while Wu reports hers on gender classification applying feature selection [78].

2.7 Summary

In this chapter, firstly, we introduce medical imaging techniques and the concepts of shape analysis and Riemannian geometry; secondly, we review the literature on shape analysis, focusing on statistical pattern recognition using graph based approaches. As an example, a Riemannian framework for tensor computing is described. Finally, some examples are presented.

There are few studies using graph based methods for MR image analysis, especially for the characterisation of white matter fibres in diffusion MR images. There are also few studies of the sulci detection in structural MR images. The related work with graph based methods commonly use 2D images of general 3D objects, rather than medical data. Therefore, there is a research gap to be filled.

This dissertation describes how the graph based methods are extended to three dimensional structural and diffusion MR images, and new shape descriptors for statistical pattern recognition are produced. Most importantly, a novel framework for inferencing white matter fibres in diffusion tensor images is presented, in which spectral graph approaches, feature selection and

machine learning are combined. First of all, a study on sulci classification is presented in the next chapter.

Chapter 3

Characterising the Sulci in Structural MR Images

This chapter presents a preliminary study, focusing on structural MR image analysis using spectral graph approaches. The objective is to test the graph-based methods using a system simpler than full diffusion tensor MRI: we apply this approach to characterise sulci in conventional structural MRI of the brain, and explore the potential of the methodology for diffusion MRI.

Structural MRI data are three dimensional scalar data, while the DT-MRI data is five dimensional data. The latter not only has magnitude but also has tensor direction, hence it is more complicated to compute.

The heat kernel and the zeta function, derived from a graph representing the MR images, are both used to generate features. Machine learning methods are then applied to the feature for the classification tasks, to classify the sulci from the background in brain MR images.

This chapter presents the work on, and the results of, the semi-automatic

sulci detection using graph based methods.

3.1 The sulci of the human brain

The sulci are important anatomical structures of the human brain. A sulcus (*pl.* sulci)(Fig.3.1) is a depression in the cerebral cortex, the outer layer of the brain, which surrounds a gyrus (*pl.* gyri). This creates the distinctive folded appearance of the brain in humans and other mammals. The sulci and fissures are both the depressions in the cortex, but fissures are deeper and larger, which divide the two hemispheres of the brain [10].

Many of the sulci divide functional areas, providing a basis for anatomical labeling of the cortical surface, and for analysing structural and functional changes in disease [57]. However, automatic detection of the sulci is difficult, due to the complex sulcal configurations.

3.2 Methodology of the sulci classification in MR images

This section describes the methodology of the sulci classification in structural MRI. This includes image pre-processing, graph representation of the MRI data, feature extraction, graph characterisation using the heat kernel signature and the zeta function trace. Statistical pattern recognition methods, namely supervised machine learning, are used for the classification of the sulci structures and the background in the MR images.



Figure 3.1: The sulci of the human brain, visible as the dark areas. The T1-weighted MRI image is visualised using Matlab; and the MRI data used are provided by the York NeuroImaging Centre.

3.2.1 MRI data and preprocessing

The T1-weighted structural MR image dataset of the single brain used in this study has the size of $256 \times 256 \times 176$ image voxels, with the voxel size of 1mm^3 , provided by the York Neuroimaging Centre. The MR images are captured at the magnetic strength of 3 Tesla.

To make the MR images of the brain useful for analysis, image preprocessing is carried out. This includes

- (a) stripping the skull from the MR images and applying eddy current correction, using FSL software; and
- (b) re-scaling the MR image intensities to the range of 0 to 255, and shifted to satisfy the Matlab indexing convention, so the MRI data can be displayed and processed by using Matlab.

3.2.2 Graph representation and sampling

A graph is represented as $G = (V, E)$, where $V = \{v_1, v_2, \dots, v_n\}$ denotes the nodes of the graph, and $E = \{e_1, e_2, \dots, e_m\}$ denotes the edges of the graph (Figure 3.2). If the objects in an image are related, they are connected by an edge in the graph.

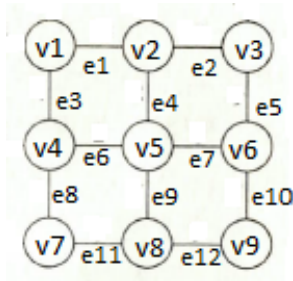


Figure 3.2: A regular graph representing an image of 3×3 pixels. The graph nodes are represented by circles, while the graph edges are depicted by lines. The nodes have no particular orders.

Graph characterisation is performed on feature vectors, which contain feature values. To extract the features, 100 samples are manually selected from different regions of the brain in the MR images, in which 50 samples are from the sulci areas, while the other 50 samples are from their background area.

A sample is a small subset of the MR images, $3 \times 3 \times 3$ image voxels in size. It is expressed as a regular graph, similar to Figure 3.3. Each voxel is regarded as a node in the graph. The central point of the sample is manually localised by using the 3-view software.

Figure 3.4 shows the three medical orthogonal planes: the sagittal, coronal and transverse planes respectively. The coordinates of the central point are chosen at the intersection of the cross hair. Together with the neighbor-

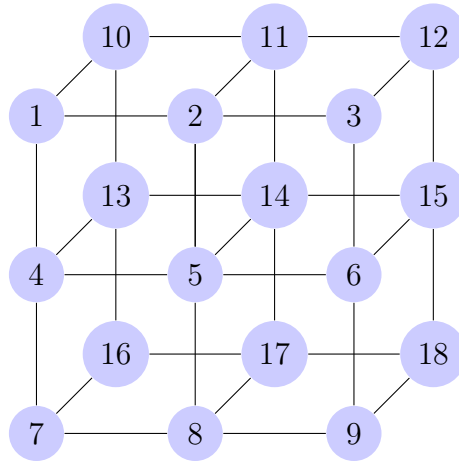


Figure 3.3: A regular graph representing $3 \times 3 \times 2$ MR images (2 slices). The nodes are connected based on the adjacent image voxel. For a structural MR image, each node can be assigned with an intensity value of the image voxel. The nodes have no particular order.

ing points (voxels) surrounding the central point, a sample of $3 \times 3 \times 3$ MR images is selected. It is used to construct a graph of 27 nodes. Similarly, 100 graphs are produced from the 100 samples.

3.2.3 Spectral graph theory and Laplacian matrix

Graph theory is a branch of mathematics. The spectral graph theory computes the eigenvalues and eigenvectors, known as the *spectrum* or *eigensystem*, of the Laplacian matrix of a graph. They are used to determine the properties of the shape under study, and can be used to create a shape descriptor.

The Laplacian matrix can be used to represent a graph. How to produce the Laplacian matrix from a graph? Consider a graph $G = (V, E)$, where V is the set of nodes and $E \subseteq V \times V$ is the set of graph edges. According to the



Figure 3.4: The coordinates of a point in 3D MR images are chosen at the cross hair position. There are 3 views: the coronal (top-left), sagittal (top-right) and transverse (bottom-left) planes. This is visualised from the structural MRI images under study.

graph theory, there is an adjacency matrix, A , describing the connectivity of the nodes as below:

$$A(u, v) = \begin{cases} 1 & \text{if } (u, v) \in E \\ 0 & \text{otherwise} \end{cases} \quad (3.1)$$

The diagonal degree matrix D has its elements obtained by

$$D(u, u) = \sum_{v \in V} A(u, v) \quad (3.2)$$

The graph Laplacian matrix, L , is defined by $L = D - A$. The normalised graph Laplacian matrix is given by

$$\hat{L} = D^{-\frac{1}{2}} L D^{-\frac{1}{2}}, \quad (3.3)$$

and the eigendecomposition of the normalised Laplacian matrix is

$$\hat{L} = \Phi \Lambda \Phi^T, \quad (3.4)$$

where $\Lambda = \text{diag}(\lambda_1, \lambda_2, \dots, \lambda_{|V|})$ is the diagonal matrix with the elements of eigenvalues in an ascending order, and $\Phi = (\phi_1 | \phi_2 | \dots | \phi_{|V|})$ is the matrix with the corresponding eigenvectors as its columns. Φ^T is the transpose of Φ .

The Laplacian matrix is symmetric and positive semi-definite, so all the eigenvalues of the Laplacian matrix are positive. After sorting the eigenvalues in an ascending order, the eigenvector associated with the second smallest eigenvalue is called the *Fiedler* vector, which is useful in graph characterisation [79][62].

However, a simple unweighted graph is insufficient to reflect the changes of information flow in the graph based diffusion method used. A weighted graph encodes richer information, in which a weight is computed for every edge of the graph. When the weight is large, the information flow (also called the heat flow) can pass through easily, or vice versa.

The Gaussian weight function, denoted by $w(i, j)$, is used for characterising the relationship between different voxels. It is computed by

$$w(i, j) = \exp\left(-\frac{\sum d^2}{k^2}\right); \quad (3.5)$$

where d is a similarity distance measure. Here $\sum d^2$ refers to the sum of the squared intensity differences of the 26 paired adjacent voxels with respect to the central voxel of the sample. The total 27 intensity values of a given $3 \times 3 \times 3$ sample are stored in a vector, and the intensity values of two adjacent points are stored in two vectors. k is the parameter of the Gaussian width.

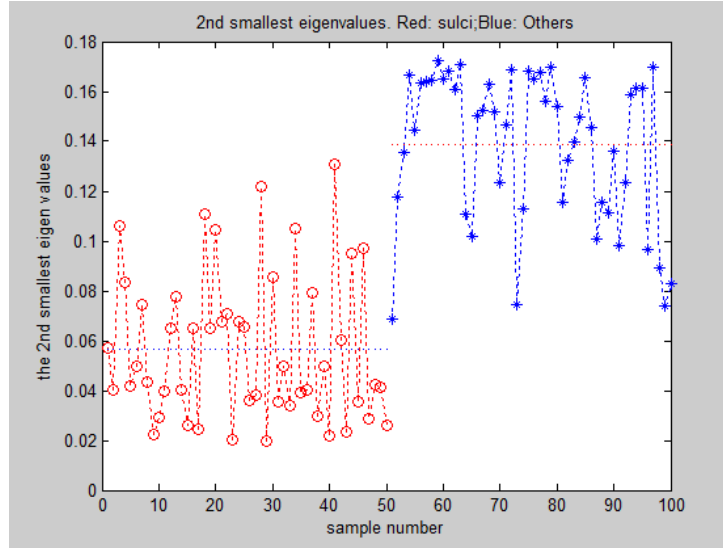


Figure 3.5: The second smallest eigenvalues of 100 graphs derived from the 100 samples. Each point represents a second smallest eigenvalue. The two horizontal lines indicate the means of 0.06 for sulci and 0.14 for the others; the standard deviation is 0.03 for both the sulci and its background.

Based on an image sample, a weighted Laplacian matrix is computed from a data graph for shape analysis. For each weighted Laplacian matrix, a set of

eigenvalues and eigenvectors are obtained by eigendecomposition. Figure 3.5 shows all the second eigenvalues, or the smallest non-zero eigenvalues, calculated from 100 normalised weighted Laplacian matrices, which are associated with the 100 samples. The red circles denote the second smallest eigenvalues derived from the Laplacian matrices that represent the sulci samples, while the blue stars denote the second smallest eigenvalues from the ones that represent the background tissues. Figure 3.5 also shows that the two means are significantly different, suggesting that the sulci and the background may be separable.

3.2.4 Graph characterisation using heat kernel signature

The sulci characterisation is equivalent to the characterisation of the graph, which represents the structural MR images of the brain. In this section, the heat kernel signature (HKS) from a weighted graph is described.

100 samples are selected from the structural MRI dataset, half from the sulci areas and the other half from the background regions. They are given a label: either “sulci” or “the others”. 100 graphs from these samples are produced. Next, the heat kernel values are computed for a graph of each sample, based on the formula below.

$$h_t = \sum_{i=1}^{|\mathcal{V}|} e^{-\lambda_i t} \phi_i \phi_i^T \quad (3.6)$$

where λ_i ($i = 2, 3, \dots, n$) are the non-zero and not repeated eigenvalues and $\phi_i(x)$ are the respective eigenvectors. They are decomposed from the

normalized weighted Laplacian matrix. The heat kernel, h_t , is a $|V| \times |V|$ matrix. t refers to the time intervals of the heat diffuse, and ϕ_i^T is the transpose of ϕ_i .

The heat kernel is a function of time. The chosen time scale and the time intervals depend on the data and the purpose. When the t is large, the HKS is better at describing the global shape, while when t interval is small, the HKS values can capture local structural information [65].

In particular, when the first few time steps are small enough, the heat kernel signature values could be distinguishable. For example, we choose 30 exponentially increasing time intervals (Fig. 3.6), based on the minimum and the maximum of the eigenvalues, setting the upper bound and the lower bound of the t range. This yields a 27×27 matrix containing all the heat kernel signature values.

For all 100 graphs derived from the 100 samples, a feature vector containing average HKS values at each time interval is computed, giving a 100×30 matrix of average HKS values. Each column is a feature vector.

There is a need to condense the matrix of the average HKS values, as visualisation is more easily performed in two or three dimensions.

Principal component analysis (PCA) is used for data condensation. Afterwards, the HKS values are projected onto lower dimension. The first two or three columns of the condensed heat kernel signature values have the largest variances of the data. They are used for visualisation.

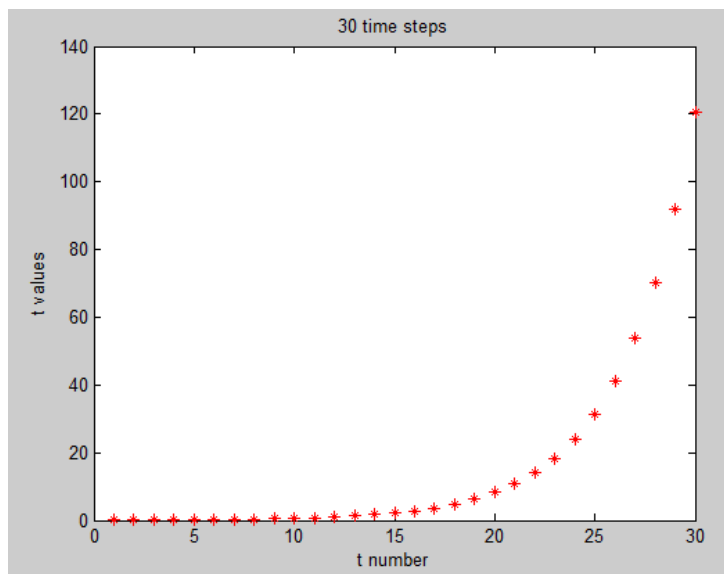


Figure 3.6: The t interval value used during the heat kernel signature value production.

3.2.5 Graph characterisation using zeta function trace

Inspired by the work of Xiao et al.[79], we use the zeta function trace values to characterise the graph derived from the 3D MR images of the brain, rather than from 2D images of 3D general objects that the authors do.

The purpose of the study is to identify the sulci and other surrounding brain tissues. However, the brain images have complex structures, and different brain structures may have similar intensity values in MR images. This makes the shape analysis challenging.

The zeta function is the moment generating function, from which the heat kernel trace is calculated. Then the trace of the zeta function for each graph is computed as a feature vector. For this, 100 samples are selected from the MRI images in the same way as using the HKS. 50 samples are manually

selected from the sulci regions, and another 50 samples are selected from the background areas. They are represented by 100 weighted indirect regular graphs.

For each graph, a normalised Laplacian matrix is produced. The eigenvalues and eigenvectors are computed, the eigenvalues are sorted in ascending order, and the corresponding eigenvectors are re-arranged. The heat kernel trace is calculated by

$$Z(t) = Tr [h_t] = \sum_{i=1}^{|\mathcal{V}|} e^{-\lambda_i t} \quad (3.7)$$

where λ_i refers to the i th eigenvalue and t is the time. Tr denotes the trace of the heat kernel, h_t . Equivalently, the trace of the zeta function is defined as

$$\zeta(s) = \sum_{\lambda_i \neq 0} (-\lambda_i)^{-s} \quad (3.8)$$

where s represents the s th moment of the zeta function. The graph characterisation can be achieved by using the moments of the zeta function trace over time.

In this example, the zeta function traces of 5 moments are computed. As we have 100 samples, each moment generates 100 zeta function trace values. Although more moments can be used to compute the zeta function trace, 5 moments are sufficient for classification here.

Statistical pattern recognition techniques are applied to the generated zeta function values, to classify the sulci and the non-sulci tissues in the MR images.

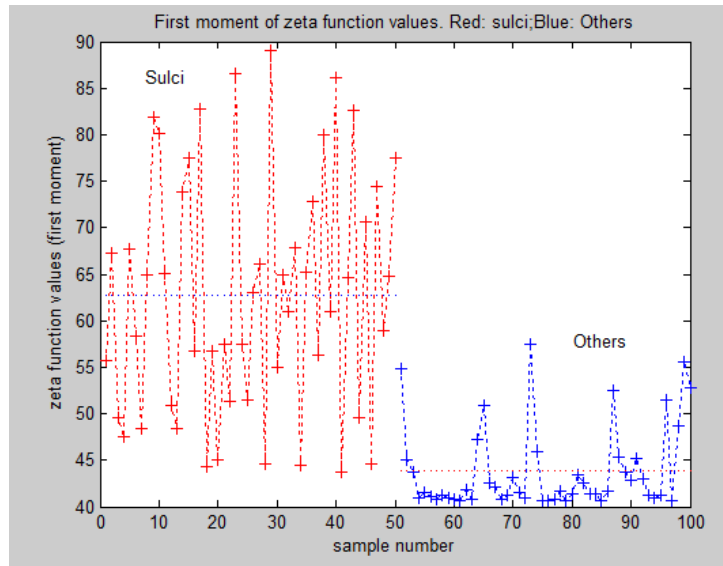


Figure 3.7: The zeta function trace values of the first moment. For the samples of manually labeled the sulci and their background, the means of zeta function trace values are 62.73 and 43.81 respectively; and their standard deviations are 12.98 and 4.47.

The Laplacian spectrum derived from a graph, namely the eigenvalues and eigenvectors, has a close relationship with the heat kernel trace. It is permutation invariant, which is important for the characterisation of a graph representing a shape.

Figure 3.7 shows that the means (horizontal lines) of the zeta function trace values of the labelled sulci samples and that of the labelled background are very different. This suggests that the sulci samples could be separated from the background samples.

3.2.6 Graph characterisation using zeta function derivative at the origin

The derivative of the zeta function at the origin is also computed (Fig.3.8). It is another permutation invariant calculated from the product of the eigenvalues. It has a potential for graph characterisation, because the difference between the derivative of sulci and that of the background is obvious.

The statistical measurements are summarised in Table 3.1. The mean values of the zeta function traces of the first moment for the sulci and the background are significantly different, implying that the zeta function trace has a strong discriminative power, as does the zeta function derivative at the origin.

	Second eigenvalue		Zeta function trace		Zeta function derivative	
Type	sulci	others	sulci	others	sulci	others
Mean	0.06	0.14	62.73	43.81	6.00	4.32
SD	0.03	0.03	12.98	4.47	0.94	0.65

Table 3.1: Mean and standard deviation of three types of features: the second eigenvalues, the first moment of zeta function trace values, and the derivatives of the zeta function.

3.3 Principal component analysis

Principal component analysis (PCA) is a conventional data reduction method (see Appendix). Both the HKS and the zeta function trace values are high dimensional data, so the principal component analysis is applied to reduce

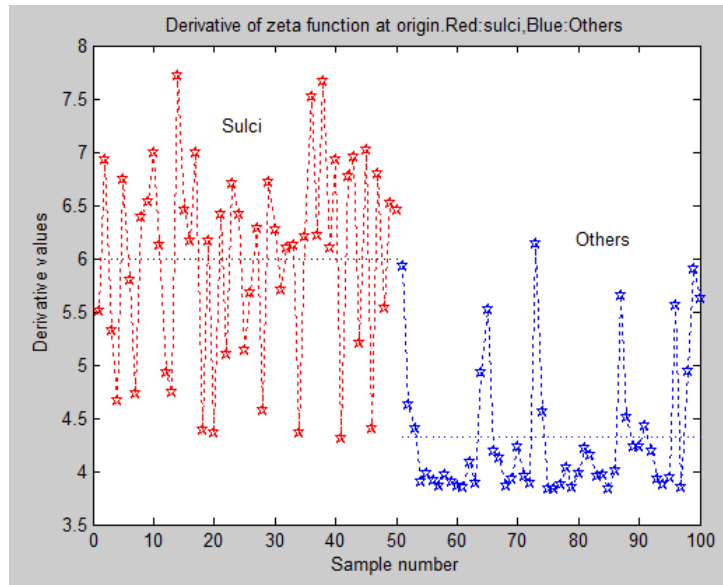


Figure 3.8: The zeta function derivative values at origin. The means is 6.00 for the sulci and 4.32 for the background. The standard deviations are 0.94 for the sulci and 0.65 for the background.

the dimension of the feature data, then the 3 leading features (components) are used for visualisation.

Figures 3.9 and 3.10 show that the two classes (the sulci and the other tissues) may be separable after the data projection. By visual assessment, the PCA performance on the trace zeta function values seems better than that of the heat kernel signature values. However, only when the feature data are large, is the application of PCA necessary.

3.4 Linear discriminant analysis

Linear discriminant analysis (LDA), also known as Fisher's linear discriminant analysis, aims to project the original data matrix onto a lower dimen-

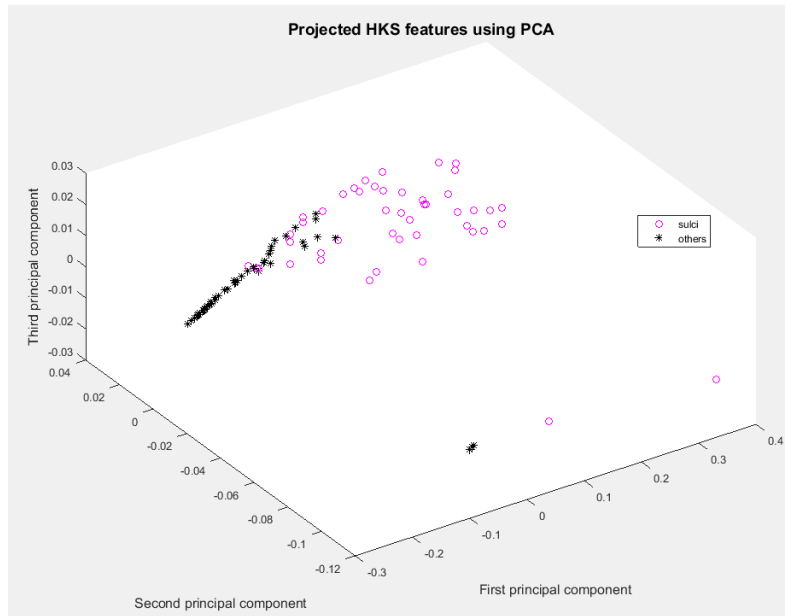


Figure 3.9: Projected heat kernel signature values using PCA.

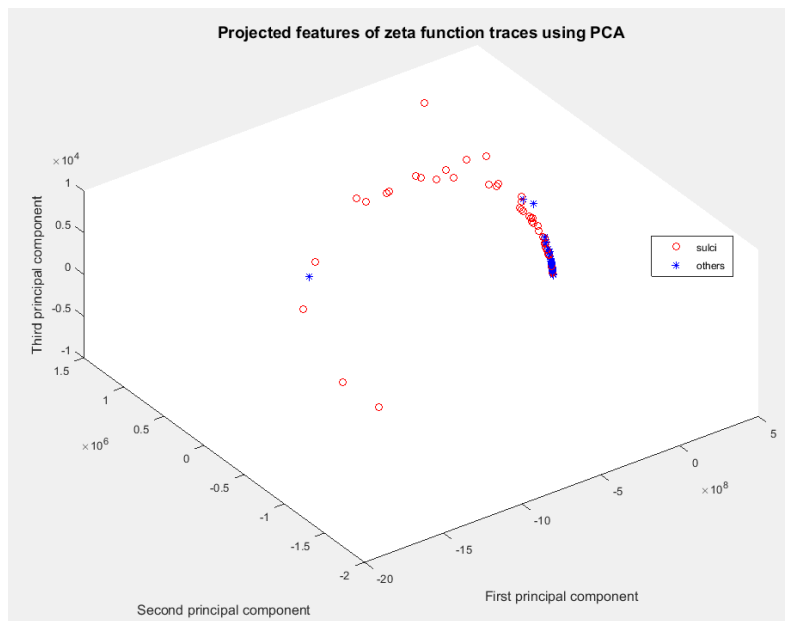


Figure 3.10: Projected zeta function trace values using PCA.

sional space. The algorithm of LDA [67] is:

- (1) calculating the separability between different classes, e.g. the distance of the means of classes, called the between- class variance (matrix);
- (2) calculating the distance between the mean and the samples of each class, known as the within-class variance (matrix);
- (3) constructing the lower dimensional space that maximises the between-class variance and minimises the within-class variance.

LDA assumes the conditional density functions $p(x|y = 0)$ and $p(x|y = 1)$ are both normally distributed. The transformation matrix, W_{Tran} , is obtained by maximising the ratio of the between-class matrix and the within-class matrix:

$$W_{Tran} = argmax_W \frac{Trace(W^T S_b W)}{Trace(W^T S_w W)} \quad (3.9)$$

where S_b is the between class scatter matrix, and S_w is the within class scatter matrix. The solution is

$W_{Tran} = [w_1|w_2|\dots|w_n]$, where $w_i (i = 1 \dots n)$ are the eigenvectors satisfying

$$S_b w_i = \lambda_i S_w w_i, (i = 1, 2, \dots n) \quad (3.10)$$

which can be resolved by eigendecomposition of the matrix $S_w^{-1} S_b$. More details are described in [26].

3.5 Sulci classification and evaluation

The sulci classification has two stages: (1) using linear discriminant analysis to project the feature data, so that they can be more easily separated; (2) using the label information in the training set to build a classifier; then the classifier is used to predict new label for the test set.

Three quantities are used for the label prediction on a test set: posterior probability, prior probability and cost. The objective of classification is to minimise the expected classification cost:

$$\hat{y} = \underset{y=1,\dots,K}{\operatorname{argmin}} \sum_{k=1}^K \hat{P}(k|x)C(y|k) \quad (3.11)$$

where \hat{y} is the predicted classification;

K is the number of classes;

$\hat{P}(k|x)$ is the posterior probability of class k for observation x ;

$C(y|k)$ is the cost of classifying an observation as y when its true class is k .

Posterior Probability: Let $P(k)$ denote the prior probability of class k , the posterior probability that an observation x belongs to class k is:

$$\hat{P}(k|x) = \frac{P(x|k)P(k)}{P(x)}, \quad (3.12)$$

where $P(x)$ is a constant of normalisation.

The multivariate normal density function with mean μ_k and covariance

\sum_k at a data point x is

$$P(x|k) = \frac{1}{(2\pi|\sum_k|)^{\frac{1}{2}}} \exp(-\frac{1}{2}(x - \mu_k)^T(\sum_k)^{-1}(x - \mu_k)), \quad (3.13)$$

where $|\sum_k|$ is the determinant of \sum_k , and $(\sum_k)^{-1}$ is the inverse matrix of \sum_k . T is transpose operation.

Prior probability (empirical): The numbers of training samples of class k divided by the total number of the training samples.

Cost: For true misclassification cost per class, it is 0 for correct classification, and 1 otherwise. For expected misclassification cost per observation, $\text{cost}(n,k)$ is

$$\sum_{i=1}^K \hat{P}(i|X_{new}(n))C(k|i) \quad (3.14)$$

where K is the number of classes; n is the number of samples. $\hat{P}(i|X_{new}(n))$ is the posterior probability of class i for observation $X_{new}(n)$; $C(k|i)$ is the cost of classifying an observation as k when its true class is i .

Sulci classification: We denote $k = \{\text{sulci}, \text{non-sulci}\}$ as the classes of the sulci and non-sulci; x is a test sample, satisfying a Gaussian distribution for the class. The definition of the mean and covariance are the same as mentioned. According to the Bayes rule, the probability that a test sample belongs to class k can be computed by using equations 3.12 and 3.13. If the posterior probability $\hat{P}(\text{sulci}|x) > \hat{P}(\text{non-sulci}|x)$, the sample is classified as the sulci; otherwise, it is classified as non-sulci.

The sulci characterisation belongs to discriminant analysis classification. Both heat kernel signature and zeta function trace values are used as features respectively. In each experiment, 30% (or 35%), 40%, 50%, 60%, 70% and 80% of the total feature data are randomly selected as a training set respectively, while the rest of the feature data as a testing set, with an intention of exploring how the size of a training set affects the classification performance. 30 runs are carried out for each case, using a different random selection; and the mean classification accuracy rate, mean false positive rate and mean false negative rate are computed.

3.6 Results of sulci classification

3.6.1 The confusion matrix

The evaluation of the classification models is based on the confusion matrix, which contains information about actual and predicted classifications. It is the outcome of linear discriminant analysis and classification. The confusion matrix is defined as:

	Predicted: non-sulci	Predicted: sulci
Actual: non-sulci	true negative (TN)	false positive (FP)
Actual: sulci	false negative (FN)	true positive (TP)

Table 3.2: A confusion matrix for two-class classification

TN: the number of correct predictions that an instance is negative;
 FP: the number of incorrect predictions that an instance is positive;
 FN: the number of incorrect predictions that an instance is negative; and

TP: the number of correct predictions that an instance is positive.

The classification performance measures, namely accuracy rate (ACR), false positive rate (FPR), false negative rate (FNR), are defined as

$$ACR = \frac{TP+TN}{TP+TN+FP+FN}; FPR = \frac{FP}{FP+TN}; \text{ and } FNR = \frac{FN}{FN+TP}.$$

3.6.2 Classification using heat kernel signature

Table 3.3 shows the results of classification using the heat kernel signature values. 35 %, 40 %, 50 %, 60 %, 70 % and 80 % of the data are randomly selected for training a classifier, while the rest of the data are used for testing the classifier. 30 runs are performed respectively, and the classification accuracy rate is computed. Then the mean is calculated. Among them, the best mean classification accuracy rate achieved is 86.56%, with standard error of 1.09% (70% of the data are used for the training). Hence, the 95% confidence intervals for the true population mean are 86.56 ± 2.14 (%), computed by using the formula: $\text{mean} \pm 1.96 \times \text{SE}$.

Classification using heat kernel signature						
Size of training set	35%	40%	50%	60%	70%	80%
mean accuracy rate	0.7031	0.7656	0.8273	0.8425	0.8656	0.8650
SE of accuracy rate	0.0172	0.0115	0.0082	0.0081	0.0109	0.0136
mean FNR	0.2875	0.2256	0.1707	0.1433	0.0978	0.1067
SE of FNR	0.0182	0.0170	0.0162	0.0135	0.0123	0.0143
mean FPR	0.3063	0.2433	0.1747	0.1717	0.1711	0.1633
SE of FPR	0.0229	0.0181	0.0152	0.0166	0.0183	0.0206

Table 3.3: Results of classification using HKS features. 30 runs in total. Different dataset percentages show different training accuracy. SE: standard error; FNR: false negative rate; FPR: false positive rate.

3.6.3 Classification using zeta function trace

Table 3.4 shows the results of classification using zeta function trace values. 30 %, 40 %, 50 %, 60 %, 70 % and 80 % of the data are randomly selected for training a classifier, while the rest of the data are used for testing the classifier. 30 runs are performed respectively, and the classification accuracy rate is computed. Then the mean is calculated. Among them, the best mean classification accuracy rate achieved is 87.33% (80% of the data are used for the training). Hence, the 95% confidence intervals for the true population mean are 87.33 ± 2.08 (%).

Classification using zeta function traces						
Size of training set	30%	40%	50%	60%	70%	80%
mean accuracy rate	0.8252	0.8361	0.8433	0.8525	0.8400	0.8733
SE of accuracy rate	0.0061	0.0068	0.0076	0.0074	0.0137	0.0106
mean FNR	0.1229	0.0922	0.0867	0.0983	0.1089	0.0800
SE of FNR	0.0132	0.0131	0.0098	0.0116	0.0206	0.0169
mean FPR	0.2267	0.2356	0.2267	0.1967	0.2111	0.1733
SE of FPR	0.0110	0.0181	0.0128	0.0138	0.0189	0.0179

Table 3.4: Results of classification using zeta function trace features. 30 runs in total. Different dataset percentages show different training accuracy. SE: standard error; FNR: false negative rate; FPR: false positive rate.

3.7 Summary and discussions

Chapter 3 presents the preliminary work of shape analysis for structural MRI images, which involves the classification of the sulci and the background in the MR images, based on the features derived from heat kernel signature and zeta function trace. They imply that the spectral graph approaches are

useful for the characterisation of the sulci in 3D MRI images. The results of classification and evaluation are promising. The following observations are made:

Firstly, it is workable to represent the 3D MR images using a weighted regular undirected graph, and the method of computing the weight of the graph edge is acceptable. The spectral graph theory approaches can be adopted to compute the graph Laplacian matrix and its eigenvalues (called the graph spectrum).

Secondly, the heat kernel signatures and the zeta function trace can be computed from the graph spectrum, respectively. They are useful as features for classification tasks. Good classification results are obtained: by using the HKS and 70% of the feature data for training, the mean classification accuracy rate are 86.56% and SE is 1.09 %, and the 95% confidence intervals for the population mean classification accuracy rate are 86.56 ± 2.14 (%); while using the zeta function trace and 80% of the feature data for training, the mean classification accuracy rate is 87.33% and SE is 1.06%, and the 95% confidence intervals for the population mean classification accuracy rate are 87.33 ± 2.08 (%). They have strong discriminative power.

Thirdly, the results show that the sulci in structural MR images can be characterised by discriminant analysis classification.

When computing the HKS values, it is important to start with small time intervals (e.g. $t=0.050, 0.053\dots$). When the time interval is small enough, then the local geometric information can be obtained; while larger time intervals enable the global geometric information to be captured. This is an empirical task.

The zeta function trace is also useful. Only 5 moments of the zeta function are used, and the features produced are very good for classification.

Both the HKS and the zeta function trace are computed from the graph spectrum. They are invariant of shape rotation and translation, which are the requirements for quantitative measurements in different coordinate systems. Most importantly, the features can be stored in a vector with indices, making computing and analysis more efficient. This overcomes the limitation of graph representation which has no natural order in the nodes.

There are some factors that can degrade the accuracy of classification. (1) additive noise in MRI data and artifacts incurred by the inhomogeneous magnetite field; (2) the motion of the subject being imaged; and (3) sampling error due to the fact that the 100 samples are manually localised.

The work presented in this chapter has established a solid foundation for the next part of the research. It is our intention to use spectral graph approaches for inferencing brain white matter fibres in diffusion MR images. structural MRI data are scalar, image processing and analysis can be done in Euclidean space; while diffusion MRI data are directional, non-Euclidean space and “curved statistics” are called for. Diffusion MRI analysis are the highlights of chapter 4. Additionally, the classification needs to be validated against unseen data to demonstrate the learning has not over-fitted the data. We have more diffusion MRI data available, allowing for the inclusion of this validation step.

Chapter 4

Shape Analysis for Diffusion MR images

The aim of the research is to infer white matter fibres from diffusion MR images. Diffusion MRI is the non-invasive imaging technique for probing micro-structures in the living brain. Diffusion tensor MR (DT-MR) images, which are transformed from diffusion-weighted MR images, are very useful for machine learning on a manifold (curved surface).

This chapter describes the theory and methodology for the DT-MR image shape analysis, with examples.

First, we explain theoretical aspects focusing on shape analysis for diffusion MR images. They are

- (a) the principles of diffusion MRI;
- (b) the formation of diffusion-weighted MR images and that of diffusion tensor MR images;
- (c) Riemannian geometry, the metrics and the mappings between the mani-

fold and the tangent plane;

The methodology covers

- (1) diffusion MR image processing;
- (2) feature extraction using spectral graph theory;
- (3) feature selection for classification;
- (4) inferring white matter fibres from diffusion tensor MR images;
- (5) supervised machine learning;
- (6) the evaluation methods.

Second, tests are carried out to explore the properties of diffusion MR images. The Riemannian metrics are studied, namely, the affine invariant metric and the Log-Euclidean metric; also the proposed shape-angle measure and heuristic method. The concepts of diffusion MRI are described, and the mappings of Riemannian manifold to the tangent plane are presented.

4.1 Theory and concepts of diffusion MRI

4.1.1 Diffusion MR imaging

Diffusion is a process of random water molecular motion, called *Brownian motion*, caused by a thermal flux between different molecular species. This is characterised by a diffusion coefficient. Diffusion coefficients may be determined by measuring the concentration of molecular species, physically or chemically, at different intervals[27].

Diffusion-weighted magnetic resonance imaging (diffusion MRI) uses the diffusion of water molecules to generate contrast in MR images. It captures

the diffusion process of water molecules in biological tissues in *vivo* and non-invasively. Water molecular diffusion in tissues is not free; it diffuses much quicker in the direction aligned with the internal structures. Therefore, water diffusion pattern can reveal the micro-structure of the brain tissues.

During diffusion MR imaging, gradient pulses in a specific direction are applied for signal encoding. In order to obtain richer water diffusion information, multiple gradient directions can be used. As a result, multiple three dimensional diffusion MRI datasets are generated. They are merged into one dataset mathematically. This technique is known as *high angular resolution diffusion-weighted imaging* (HARDI). The HARDI data are used for this research.

HARDI data can be transformed into diffusion tensor MR images (DTI or DT-MRI) for shape analysis. The DTI associates the covariance matrix of the water diffusivity at each voxel of a 3D MRI volume. It approximates the probability density function modeling the water molecules Brownian motion [44]. The DTI data have both magnitudes and angles, they should be computed in non-Euclidean space, like the Riemannian manifold.

4.1.2 The diffusion tensor

The diffusion tensor is defined as a 3×3 symmetric positive definite matrix, referred to as for the *tensor*, meaning that all its eigenvalues are positive.

The space of symmetric positive definite matrices is endowed by a regular geometrically complete (without boundaries) manifold.

Diffusion-weighted MR images are used to produce diffusion tensor images, from which the geometrical information is very useful for shape analysis.

The definition of the diffusion tensor is a covariance matrix:

$$D = \begin{vmatrix} D_{xx} & D_{xy} & D_{xz} \\ D_{xy} & D_{yy} & D_{yz} \\ D_{xz} & D_{yz} & D_{zz} \end{vmatrix}$$

Diffusion tensor D is symmetric and semi-positive definite defined. x, y and z represent the three orthogonal axes. The covariance matrix fully describes molecular mobility along each direction and the correlation between these directions [13]. It reflects the fact that diffusion is a three dimensional process, and molecular mobility in tissues may not be the same in all directions.

4.1.3 Diffusion tensor estimation

Diffusion tensor estimation is performed by solving the Stejskal and Tanner diffusion equation [64]:

$$S_j = S_0 e^{-b_j \hat{g}_j^T D \hat{g}_j} \quad (4.1)$$

where D represents the diffusion tensor; \hat{g}_j represents the non-colinear and non-coplanar gradient direction, and j denotes different direction along which diffusion weighting is applied. \hat{g}_j^T is the transpose of \hat{g}_j . All the gradient directions, e.g. (1,1,0), (0,1,1) and (1,0,1), are given, together with the diffusion weighted MR images. The b -value, b_j , are the MR imaging parameters. S_0 is the intensity without diffusion gradient being applied.

The effect of diffusion on the MRI signal (a spin-echo signal) is an atten-

uation, denoted as A :

$$A = e^{-bD} \quad (4.2)$$

The attenuation depends on diffusion tensor D and the b -value that characterises the gradient pulses applied to the MRI sequence, such as the timing, amplitude and the shape of the pulses.

Since the MR signal measurements are made in the reference frame of the MRI scanner gradients, which is not identical to the diffusion frame of the tissue, thus the coupling of the non-diagonal elements: b_{ij} of the b -matrix (containing gradient information) and D_{ij} ($i = j$) must be taken into consideration. This gives a new expression [9]:

$$A = \exp(-(b_{xx}D_{xx} + b_{yy}D_{yy} + b_{zz}D_{zz} + 2b_{xy}D_{xy} + 2b_{xz}D_{xz} + b_{yz}D_{yz})) \quad (4.3)$$

The estimation of diffusion tensor is done by solving the above equation using multiple linear regression. Since the diffusion tensor is symmetric, so only 6 variables need solving, and at least 6 simultaneous equations are required to estimate a tensor. Therefore, at least 6 diffusion weighted images are required to produce one tensor image.

4.1.4 Parameters derived from the diffusion tensor

The diffusion tensor can be visualised as an ellipsoid geometrically, which was introduced by Basser et al. in 1994 [7]. It uses the scalar parameters derived from the diffusion tensor.

Given the diffusion tensor D , a 3×3 matrix, its real eigenvalues $\lambda_1 \geq \lambda_2 \geq \lambda_3$, and the corresponding eigenvectors v_i ($i = 1, 2, 3$) can be obtained

by eigendecomposition. The shape of the tensor can be depicted by the eigenvalues; and the eigenvectors describe principal diffusion direction and the apparent diffusivity along these directions [43].

In diffusion tensor images, for simplicity, only 3 types of shapes are discussed. If $\lambda_1 = \lambda_2 = \lambda_3$, then the tensor shape is spherical; if $\lambda_1 \gg \lambda_2 = \lambda_3$, it is anisotropic and is depicted as a prolate ellipsoid (linear, like a pencil); if $\lambda_1 \ll \lambda_2 = \lambda_3$, it is oblate (planar, like a pancake) shaped (Fig.4.1).

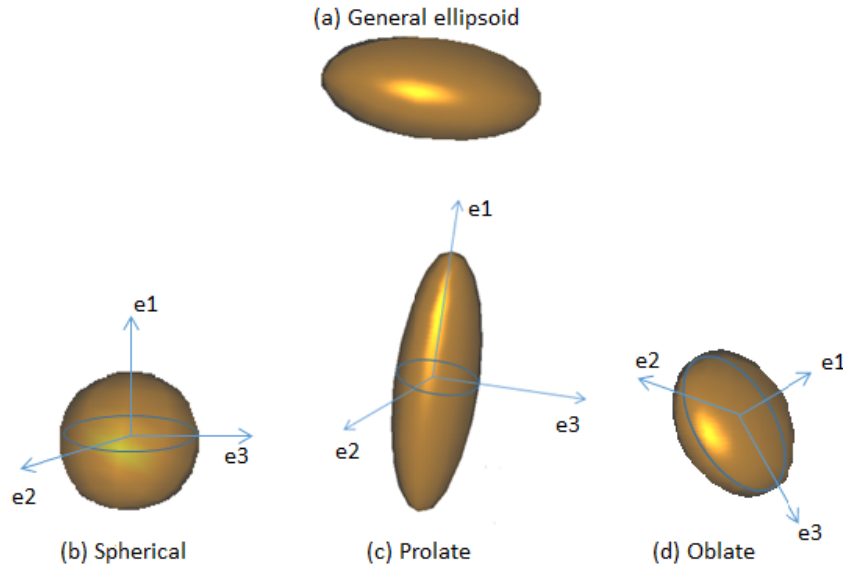


Figure 4.1: Diffusion tensor shapes. (a) A general ellipsoid; (b) In isotropic media, diffusion ellipsoid is spherical; in anisotropic media, it is prolate (c) or oblate (d). e_1 , e_2 and e_3 denote the eigenvectors decomposed from the tensor.

A quantitative method of measuring the shape of a tensor is proposed by Westin[74]:

$$C_L = \frac{\lambda_1 - \lambda_2}{\lambda_1}, \quad (4.4)$$

$$C_p = \frac{\lambda_2 - \lambda_3}{\lambda_1}, \quad (4.5)$$

$$C_s = \frac{\lambda_3}{\lambda_1} \quad (4.6)$$

C_L , C_p , and C_s are called the *Westin indices*, representing the linear, planar and spherical shaped of the ellipsoid, respectively. The value is between 0 to 1, and $C_l + C_p + C_s = 1$.

4.1.5 Riemannian geometry

Shape analysis for diffusion MRI is based on differential geometry; particularly, one of its branches known as Riemannian geometry is applied to this study. Developed by Bernhard Riemann in the 19th century, Riemannian geometry studies smooth manifolds linked to a Riemannian metric.

A Riemannian manifold is a real, smooth topological space, M . It is equipped with an inner product on the tangent space T_pM at each point p . A Riemannian metric measures local information on angles, length of curves and volumes. Riemannian geometry is particularly suitable for studying curves and surfaces [44].

Anatomical objects are usually considered in non-Euclidean spaces, or on a manifold, where conventional statistical tools may not be valid for shape analysis [55]. In contrast, a Riemannian manifold consists of symmetric positive definite matrices that constitute a convex half-cone in the vector space of matrices, where statistical operations, such as the mean and variance, are stable.

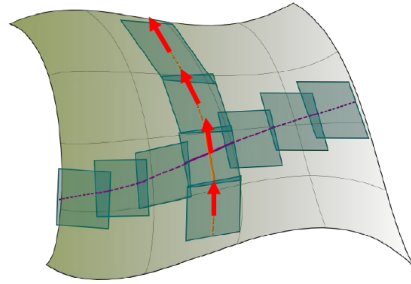


Figure 4.2: The connection structure for a manifold. From Lê N. Hoang, science4all.org

Diffusion tensor MR images have both magnitude and orientation, which can be naturally expressed on a Riemannian manifold. DT-MR image analysis can be performed on Riemannian manifolds. To understand Riemannian geometry and DT-MR images, we explain the core concepts of differential geometry as, including the connection structure, geodesic distance, metrics and the mappings of a point on a Riemannian manifold to its tangent plane. On the tangent plane, conventional statistics can be applied for data analysis.

4.1.6 The connection structure

The differential properties of the manifold can be separated from the geometry and the metrics. The local structure of a manifold M can be specified by neighboring points and the tangent vectors[55]. This permits simple, consistent, smooth functions on the manifold to be differentiated, and defines continuous paths on the manifold. The paths are constructed by a geometric structure known as a *connection*, enabling the use and a comparison of neighboring tangent spaces.

4.1.7 Exponential and logarithmic maps

Assuming the Riemannian manifold is geodesically complete, a one-to-one mapping between the manifold and the tangent plane is available locally around zero in the tangent space, or around point y on the manifold. Inversely, the logarithmic mapping is a vector of the tangent space at point y . The exponential and logarithmic mappings are different for each manifold and for each metric.

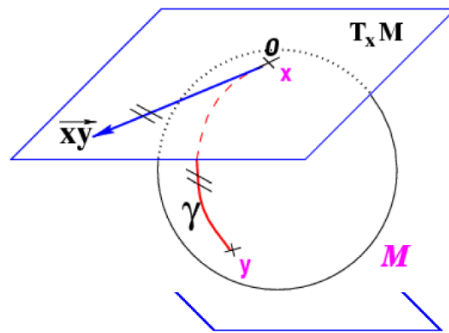


Figure 4.3: Exponential and logarithmic maps. M : a manifold, $T_x M$: the tangent plane to the manifold at the point x . y is another point on the manifold. Point y can be mapped onto the tangent plane using the logarithmic map, while a point of the tangent plane can be mapped onto the manifold by the exponential map[54].

4.1.8 Riemannian metrics and other measures

In Riemannian geometry, the shortest distance on the manifold is called the *geodesic distance*. It is a curve on the surface. A Riemannian metric is defined by a continuous collection of scalar products on each tangent space at point p of the manifold. On any Riemannian manifold there is a unique *connection*

that is compatible with the metric, known as the *Levi-Civita* connection, on which the shortest paths are *geodesics*. A Riemannian metric can be used to compute the statistical mean and the covariance matrix.

Affine invariant metric

Pennec et al. propose an affine invariant Riemannian metric defined as follows [55]. Given two tensors, D_1 and D_2 , their geodesic distance on the Riemannian manifold is defined as

$$d_{D_1 D_2} = \sqrt{\text{Tr}(\log^2(D_M))} = \sqrt{\sum_{i=1}^3 \log^2 \lambda_i} \quad (4.7)$$

where λ_i are the eigenvalues of the matrix $D_M = D_1^{-\frac{1}{2}} D_2 D_1^{-\frac{1}{2}}$.

Let S^+ denote the manifold, the geodesic distance has the following properties:

1. Positivity: $d_{D_1 D_2} > 0$
2. Symmetry: $d_{D_1 D_2} = d_{D_2 D_1}$
3. Triangle inequality: $d_{D_1 D_3} \leq d_{D_1 D_2} + d_{D_2 D_3}$
4. Invariance under congruence transformations: $\forall p \in S^+$
5. Invariance under inversion: $d_{D_1 D_2} = d_{D_1^{-1} D_2^{-1}}$

Log-Euclidean metric

To reduce the computational cost for the Riemannian geodesic distance measurement, while preserving many of their properties, Arsigny et al. define the Log-Euclidean metric for the tensor distance measure [2]. It enables vector space structures to be carried from the tangent space to the manifold.

Compared with the affine invariant metric, the Log-Euclidean metric also has some invariant properties: namely inversion, scaling, transformation in the log space, and orthogonal transformations.

The Log-Euclidean metric for Riemannian geodesic distance measure is:

$$d_{D_1 D_2} = \|\log D_1 - \log D_2\| \quad (4.8)$$

where D_1 and D_2 denote two diffusion tensors. $\log D_1$ means the matrix-logarithm of the tensor D_1 . The computation of geodesic distance is simpler than that using the affine invariant metric [2].

Shape-Angle measure

The proposed *shape-angle* measure is influenced by information theory. It is used to measure the similarities between the distance of tensors. The shape-angle measure consists two parts, representing the tensor shape and the angle of two tensors. This measure is to compute: (1) the difference of the eigenvalues of the two tensors; and (2) the angle between the principal eigenvectors of the two tensors.

The descriptor takes the physical meaning of the tensor, both the shape and orientation, into account.

The differences of the eigenvalues derived from two tensors represent the difference of their shapes; while the angle of two tensors is the angle of their principal eigenvectors. Hence, the distance of the two tensors, D_1 and D_2 , is denoted as

$$d_{D_1 D_2} = E_{shape} + E_{angle} \quad (4.9)$$

where

$$E_{shape} = \sum_{i=1}^3 \frac{4(\lambda_{iD_1} - \lambda_{iD_2})^2}{(\lambda_{iD_1} + \lambda_{iD_2})^2} \quad (4.10)$$

and

$$E_{angle} = \cos^{-1} \phi_{D_1}^1 \phi_{D_2}^1 \quad (4.11)$$

where λ_{iD_1} ($i=1,2,3$) are the eigenvalues of the tensor D_1 , while λ_{iD_2} ($i=1,2,3$) are the eigenvalues of the tensor D_2 . E_{angle} represents the angle of the principal directions of the two tensors, $\phi_{D_1}^1$ and $\phi_{D_2}^1$ are the principal eigenvectors of D_1 and D_2 respectively.

Heuristic method

One of the contributions of this study is that we propose a heuristic method, which is a similarity measure for the tensors. It measures the geodesic distance of two tensors in this way:

- (1) computing the angle of the principal eigenvectors of two tensors; if the angle is less than a threshold (e.g. 10 or 12 degrees), then the angle is computed as the distance; otherwise
- (2) using the Riemannian affine invariant metric to compute the geodesic distance.

The reason is that angle can be a similarity measure, and the principal eigenvectors of two tensors have an angle. When the angle is small, the two tensors tend to be parallel to each other, or vice versa.

4.1.9 Spectral graph theory

Algebraic graph theory is a branch of mathematics, studying graphs by using algebraic properties of associate matrices.

Spectral graph theory studies the relation between graph properties, the spectrum of the adjacency matrix and that of the Laplacian matrix. The *spectrum* refers to the set of eigenvalues and their corresponding eigenvectors, known as the *eigensystem*, produced through eigendecomposition of the matrix.

Geometrical information can be derived from the spectrum of the associated matrix, for example, the adjacency spectrum provides rich structural information [77]. Spectral graph theory can be used for graph characterisation. For example, using the heat kernel trace derived from the graph Laplacian matrix [79], or the graph edge based wave kernel [3][4]. Spectral graph theory can also be applied to image segmentation. Shi proposed a graph cut approach using the second smallest eigenvector, called the Fiedler vector, for image segmentation [62]. The idea is that a graph can be partitioned into two separate node sets by removing edges connecting them.

Spectral graph theory is useful in shape analysis. A disadvantage is that the computation may be intensive, when computing between pairwise voxels. This prevents spectral graph theory from being applied widely to 3D medical image analysis[25].

The existing applications of spectral graph theory are usually non-medical; we wish to explore its use for medical MR images.

4.1.10 Support vector machine

In machine learning, support vector machines (SVMs) are supervised learning models; SVMs use associated learning algorithms for data analysis and pattern recognition. Given training examples that are labelled with one of two categories, an SVM training algorithm builds a model that assigns new examples to one category or the other.

support vector refers to the training examples nearest to the decision boundary, and the *margin* is defined as $\frac{m}{\|w\|}$, where w is a weight vector and m represents the distance between the decision boundary and the nearest training instances.

A supervised learning algorithm analyses the training data and produces an inferred function, which can be used for mapping new instances. Ideally, the algorithm could correctly determine the class labels for unseen instances, which requires the learning algorithm to generalise from the training data to unseen situations [33].

The SVMs can be used for linear and non-linear data classification. As diffusion MRI data are non-linear by nature, they are assumed as Gaussian distribution, hence SVMs with the Gaussian kernel are used for the white matter fibre classification:

$$K(x_i, x_j) = e^{\frac{-\|x_i - x_j\|^2}{2\sigma^2}}, \quad (4.12)$$

where X_i, X_j are the training samples, and σ is the kernel width.

For non-separable data, the SVMs are considered as the dual optimisation

problem formulated as the Lagrange multipliers below, and this function is maximised under positivity constraints and one equality constraint [33]:

$$\alpha_1^*, \dots, \alpha_n^* = \underset{\alpha_i \geq 0}{\operatorname{argmax}} \sum_{i=1}^n \sum_{j=1}^n \alpha_i \alpha_j y_i y_j x_i \cdot x_j + \sum_{i=1}^n \alpha_i, \quad (4.13)$$

subject to $0 \leq \alpha_i \leq C$ and $\sum_{i=1}^n \alpha_i y_i = 0$,

Here C is a user defined parameter, trading off margin maximisation against the margin errors. The higher the C value, the higher the penalty, while the lower the C value, the more margin errors are allowed in order to achieve a large margin. In this study, the optimisation problems are solved by the sequential minimal optimisation (SMO).

Equation 4.13 implies that searching for the maximum-margin decision boundary is the same as searching for the support vectors, which are the training examples with non-zero Lagrange multipliers; and the decision boundary is determined by $w = \sum_{j=1}^n \alpha_j y_j x_j$. The optimisation problem is defined by pairwise dot products between training instances [33].

With a kernel SVM, the kernel implicitly maps the inputs into high-dimensional feature spaces, and an optimal separating hyperplane is constructed. However, when the dimensionality of the feature space is large, a hyperplane that separates the training data does not necessarily generalise well [71].

4.2 Methodology for diffusion MRI analysis

4.2.1 The HARDI data

High angular resolution diffusion MRI (HARDI) data are diffusion-weighted MR images (DWI). Five HARDI datasets, each comprising data from a whole human brain, are used for this study. Among them, four datasets are provided by the York Neuroimaging Centre, and one dataset is from the Human Connectome Project (<https://db.humanconnectome.org/>).

The HARDI datasets are acquired using multiple imaging gradient directions, so multiple volumes of data are produced. The echo planar imaging (EPI) pulse sequence is applied, the b -value is $1000 \text{ s}/(\text{mm})^2$, and the magnetic field strength is 3.0 Tesla.

For example, dataset1 is acquired under 62 gradient directions, along which the diffusion weightings are isotropically distributed. Sixty-two datasets are produced and merged into one dataset across all the corresponding voxels. Each DWI volume, $128 \times 128 \times 44$, is acquired using a different gradient direction. A full data description of all datasets is presented in Table 6.1.

An important step of image preprocessing is image registration (alignment). In the above example, each voxel of the 62 datasets is aligned spatially. Then the eddy current correction is conducted, and the brain in the MR images is extracted completely and the skull is removed from the MR images. These are achieved by using the FMRIB software library (FSL)[38].

4.2.2 Data transformation from HARDI to DTI images

The FSL software is also used to achieve the transformation of DWI to DTI. The process is illustrated as Fig.4.4.

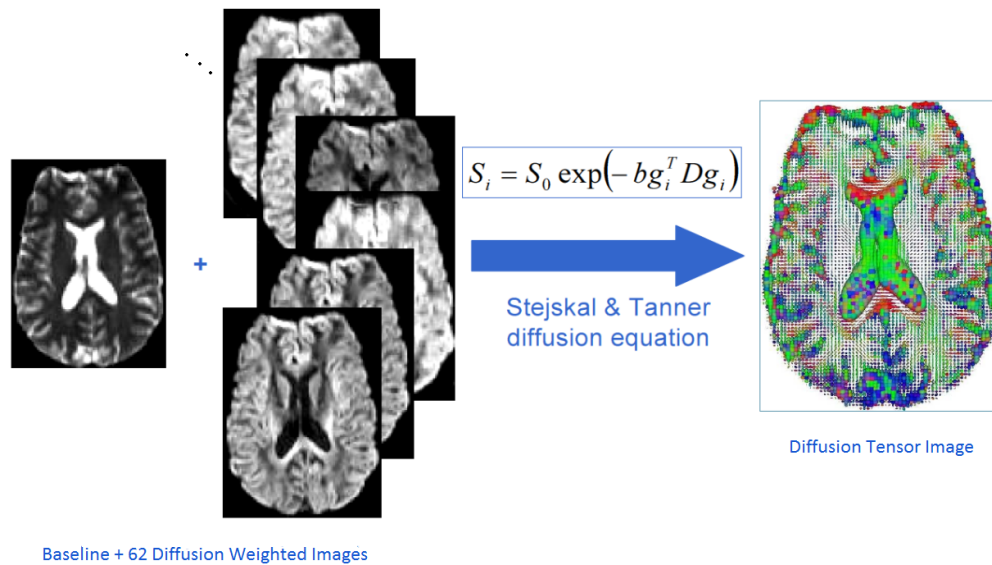


Figure 4.4: Image transformation: from diffusion-weighted MR images to diffusion tensor image (Dataset1). The Stejskal and Tanner diffusion equation is used [74].

Based on the HARDI images, the Gaussian diffusion profiles can be constructed. Generally, the more gradient directions are used, the more precisely the variation of diffusion along different directions can be detected, but more image noise can be introduced. The purpose of statistical estimation is to define the magnitude and predominant orientation of the tensor, also for other diffusion directions. Thus a 3×3 tensor (matrix) is created for that voxel position. In such a manner, all voxels are estimated. For each gradient

direction, a set of MR images are generated.

In the case of dataset1, 62 gradient directions are applied, and 62 sets of diffusion weighted MR images are created. They are combined to form one set of 3D diffusion tensor MR images.

4.2.3 Diffusion tensor visualisation

Diffusion tensor visualisation is important for computer labelling the subsamples. The diffusion tensor can be visualised geometrically as an ellipsoid, which was introduced by Basser et al. in 1994 [7]. The quantitative parameters derived from the diffusion tensor are used. By eigendecomposition of the tensor matrix, 3 eigenvalues and 3 eigenvectors are obtained. The eigenvalues describe the shape of the tensor, and the eigenvectors indicate the directions of the 3 orthogonal axes.

A visualisation tool originally developed by Barmpoutis et al. [5] is able to visualise a two dimensional tensor image. We have modified it, so it can visualise tensor images in three orthogonal view (see Figures 4.5 and 4.6).

In these tensor images, the spherical tensors represent the grey matter and the cerebrospinal fluid (CSF), while the linear shaped tensors represent the white matter fibre bundles. It is impossible to show a single neural fibre with a tensor, as the fibre diameter is only around 5-10 μm , and a voxel size is usually at least 1mm^3 .

4.2.4 Extracting quantitative parameters from DTI

A number of diffusion parameters derived from DTI can describe the properties of diffusion MRI. They are used to depict the shape of the tensor. They

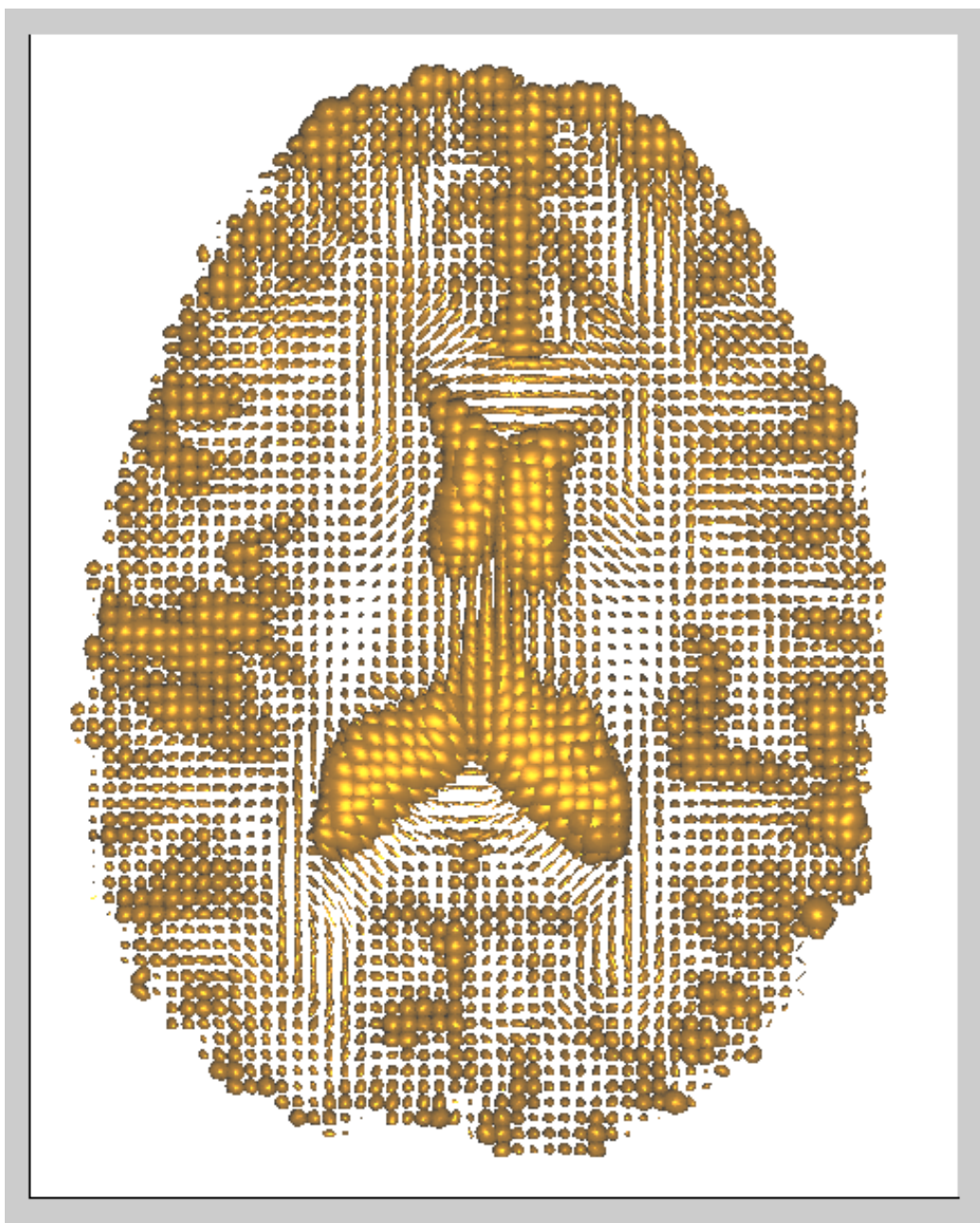
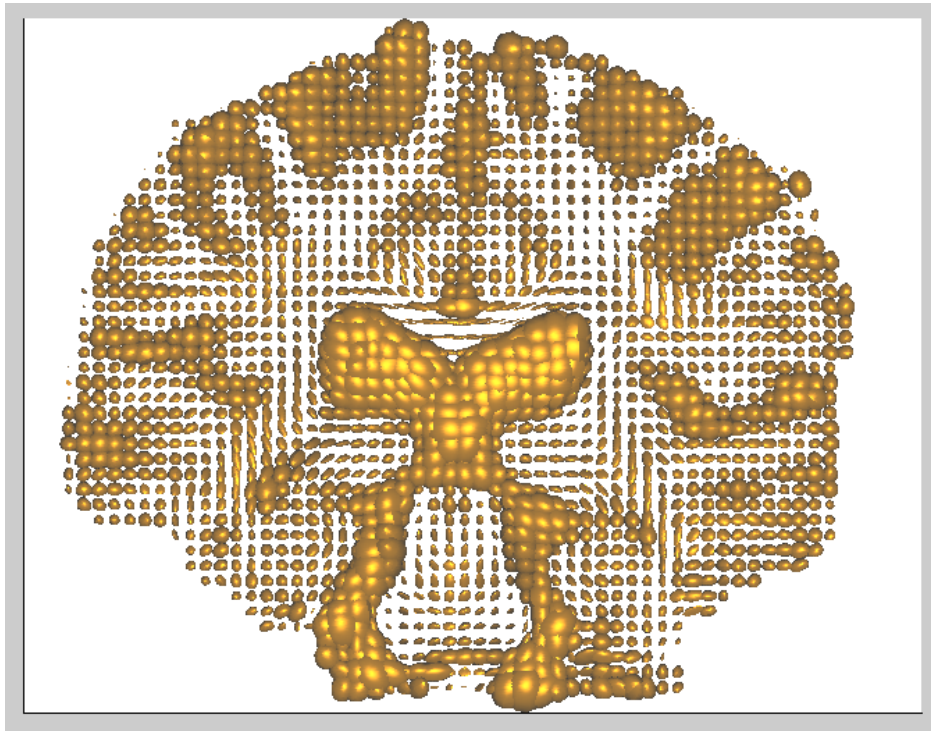
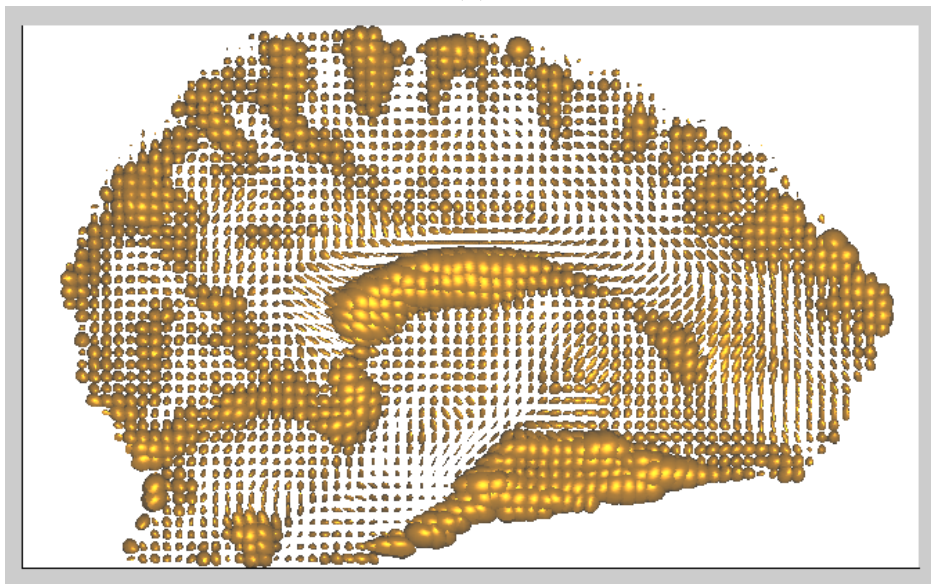


Figure 4.5: A diffusion tensor image of the human brain (axial view); Dataset1 with a voxel size of 2.5 (mm)^3 .



(a)



(b)

Figure 4.6: A diffusion tensor images of the human brain; (a) coronal view and (b) saggital view. Dataset1 with a voxel size of 2.5 mm^3

are also used for assisting clinical studies.

Diffusion tensor images analysis can provide information on tissue microstructure for each voxel. The information can be described as scalar quantitative measurements. Most diffusion parameters are derived from the eigenvalues of the diffusion tensor through eigendecomposition.

The diffusion tensor may be used to characterise the magnitude and the degree of anisotropy, and the orientation of directional diffusion. There are two important measurements of diffusion MRI:

(1) *Mean diffusivity* (MD):

$$\bar{\lambda} = \frac{1}{3} \text{Trace}(D), \quad (4.14)$$

where $\text{Trace}(D) = \lambda_1 + \lambda_2 + \lambda_3$, and

(2) *Fractional anisotropy* (FA):

$$FA(D) = \sqrt{\frac{3}{2} \frac{\sqrt{(\lambda_1 - \bar{\lambda})^2 + (\lambda_2 - \bar{\lambda})^2 + (\lambda_3 - \bar{\lambda})^2}}{\sqrt{\lambda_1^2 + \lambda_2^2 + \lambda_3^2}}} \quad (4.15)$$

where λ_i (i=1,2,3) are the eigenvalues of the diffusion tensor. FA takes on values between 0 (isotropic diffusion) and 1 (infinite anisotropy). MD and FA are invariant scalar measures. They are the popular scalar measures in clinical studies (see Figure 4.7). FA characterises the degree of out-of-roundness of the diffusion ellipsoid [9]. However, FA value sometimes lacks of specificity. It is lower in some brain regions where there is fibre crossing, such as near the lateral cerebra-ventricles.

FA is also used to determine irrelevant brain tissues, such as the grey

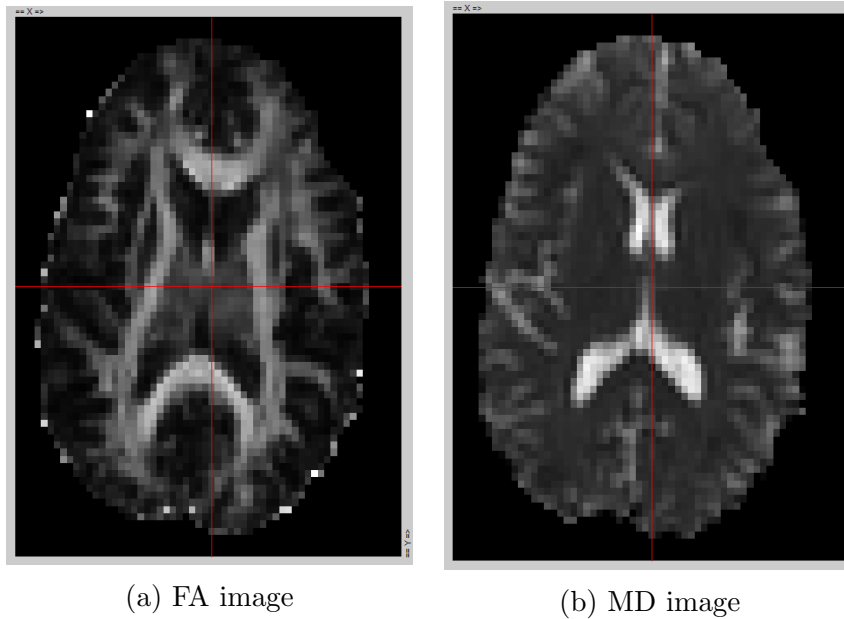


Figure 4.7: (a) A fractional anisotropy (FA) image; (b) A mean diffusion (MD) image. Dataset1.

matter or the cerebrospinal fluid (CSF). We use FA and other measures to assist sample labelling (Chapter 5).

The diffusion is highly anisotropic in fibrous tissues such as white matter. The direction of greatest diffusivity is generally assumed to be parallel to the local direction of white matter fibre [9]. With diffusion tensor images, the directional information of white matter fibre can be derived. Hence, the white matter fibre bundle underlying can be inferred.

Figures 4.8 and 4.9 illustrates the principal eigenvectors (lines or points) in the diffusion tensor images. The red, green and blue colors indicate the different directions of the principal eigenvectors. With the principal eigenvector values of the tensors, white matter tracts can be estimated to form a neural connectivity map.

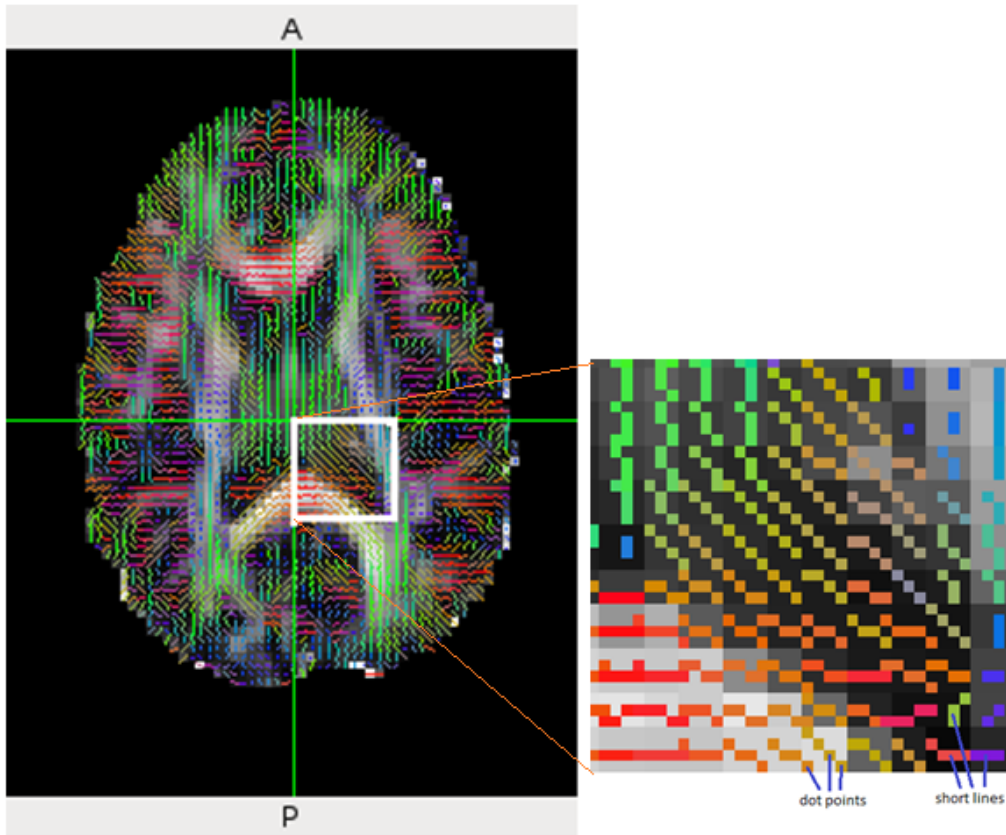
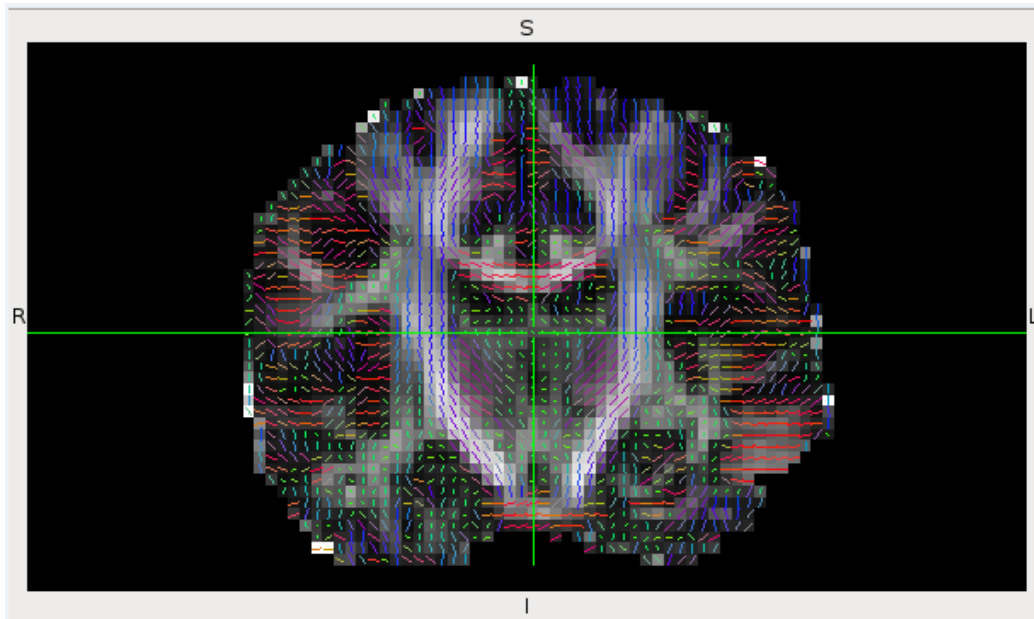


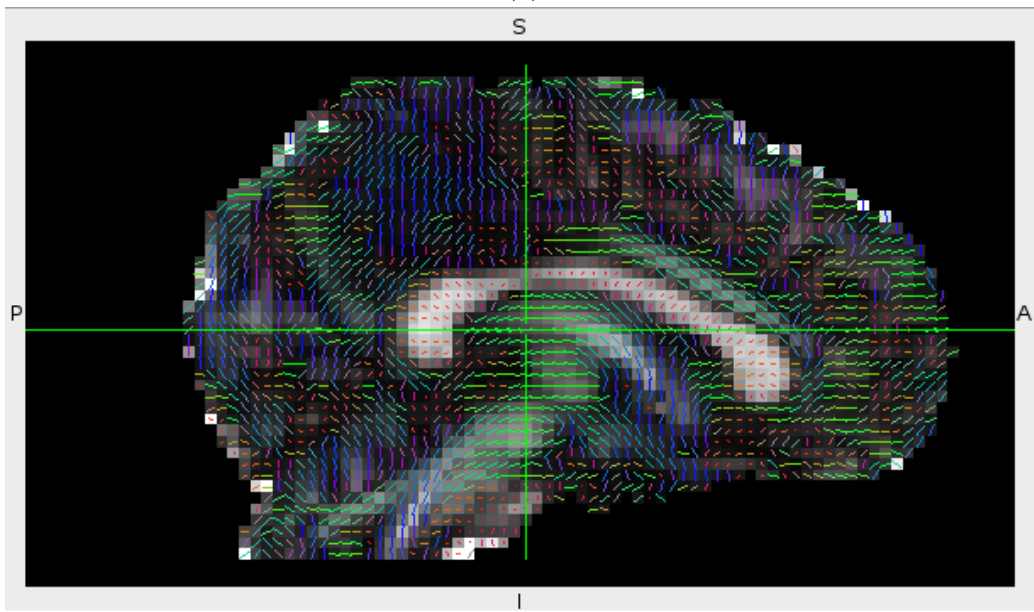
Figure 4.8: A brain MR image overlaid by the principal eigenvectors of the tensor and the FA values. The line colors indicate the directions of the principal eigenvectors; red: left-right; green: anterior-posterior; blue: foot-head. A short line represents a principal eigenvector of the tensor within a voxel, and a dot point depicts the principal eigenvector of the tensor perpendicular to the paper. (axial view, voxel size: 2.5 mm^3 , Dataset1.)

4.3 Tests: the brain structure detection

Some tests are carried out to explore the use of the spectral graph method to characterise the brain strictures in DTI, to deepen our understanding of the methodology of inferring the white matter fibres. This is a simplified version of using spectral graph theory for brain structure detection, using DT-MR



(a)



(b)

Figure 4.9: A brain MR image overlaid by the principal eigenvectors of the tensor and FA values. The line colors indicate the directions of the principal eigenvectors; red: left-right; green: anterior-posterior; blue: foot-head. (a) coronal view; and (b) sagittal views. Dataset1.

images and eigenvector images.

The steps of the algorithm are:

(1) Creating a regular graph representation of diffusion tensor images, where nodes represent the tensors and the edges are assigned weights. For two non-zero tensors, the edge weight of the Laplacian graph is determined by

$$weight = e^{-\frac{d(D_1, D_2)^2}{K^2}},$$

where d denotes the geodesic distance between tensors D_1 and D_2 ; K is the width of the Gaussian kernel. Here the Riemannian affine invariant metric [55] is used to compute the geodesic distance.

(2) Generating the Laplacian matrix (degree matrix minus adjacent matrix) of the graph and normalising it. The Laplacian matrix represents a graph derived from diffusion tensor images.

(3) Computing the eigenvalues and eigenvectors of the normalised Laplacian matrix, using eigendecomposition. The eigenvalues are arranged in an ascending order, and their corresponding eigenvectors are re-arranged.

(4) Producing the eigenvector images for the brain structure detection, using the first few eigenvectors. For visualisation, each eigenvector is reshaped to form a grey image in the same size of the associated diffusion MR image.

Figures 4.10 and 4.11 display a sequence of diffusion tensor images of the corpus callusom (CC) on the sagittal plane. The DTI images of the white matter fibre bundle are on the left, while the corresponding second eigenvector (EV) images are on the right.

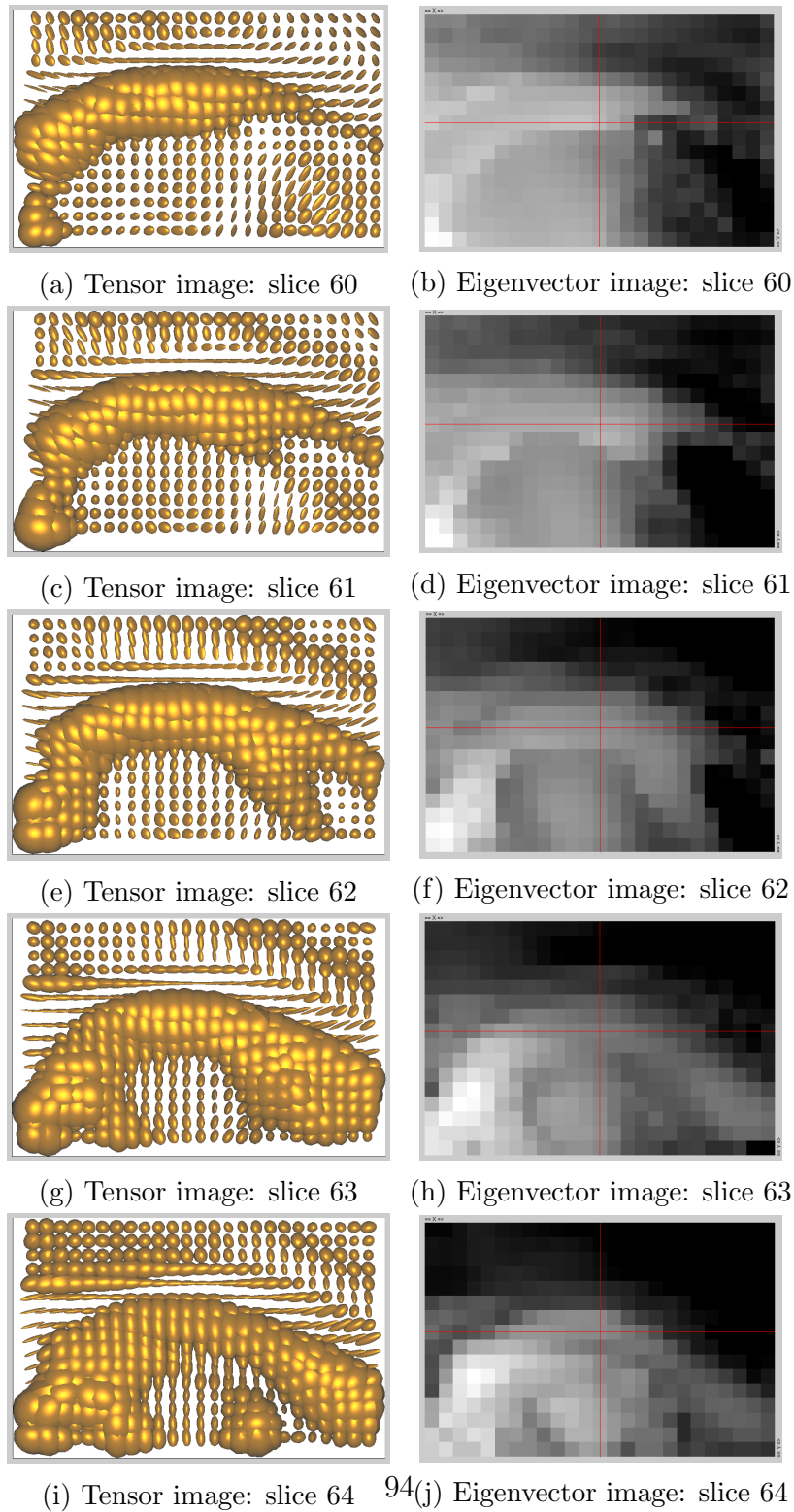


Figure 4.10: Left: A sequence of diffusion tensor images of corpus callosum (slices 60-64, sagittal); Right: their second eigenvector images. The eigenvector images reproduce the structures contained in the tensor images. (Dataset1)

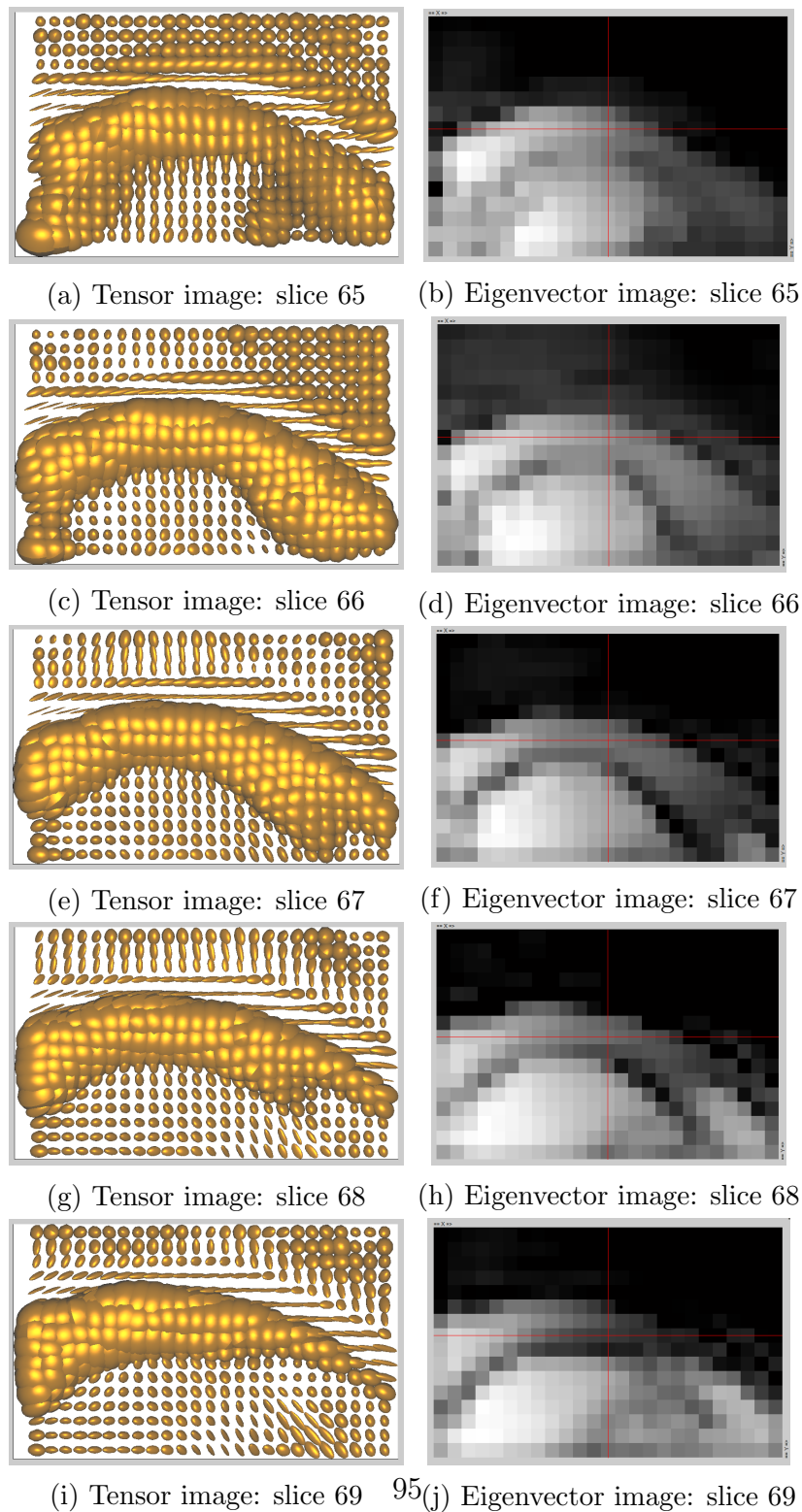


Figure 4.11: Left: A sequence of diffusion tensor images of corpus callosum (slices 65-69, sagittal); Right: their second eigenvector images. The eigenvector images reproduce the structures contained in the tensor images. (Dataset1)

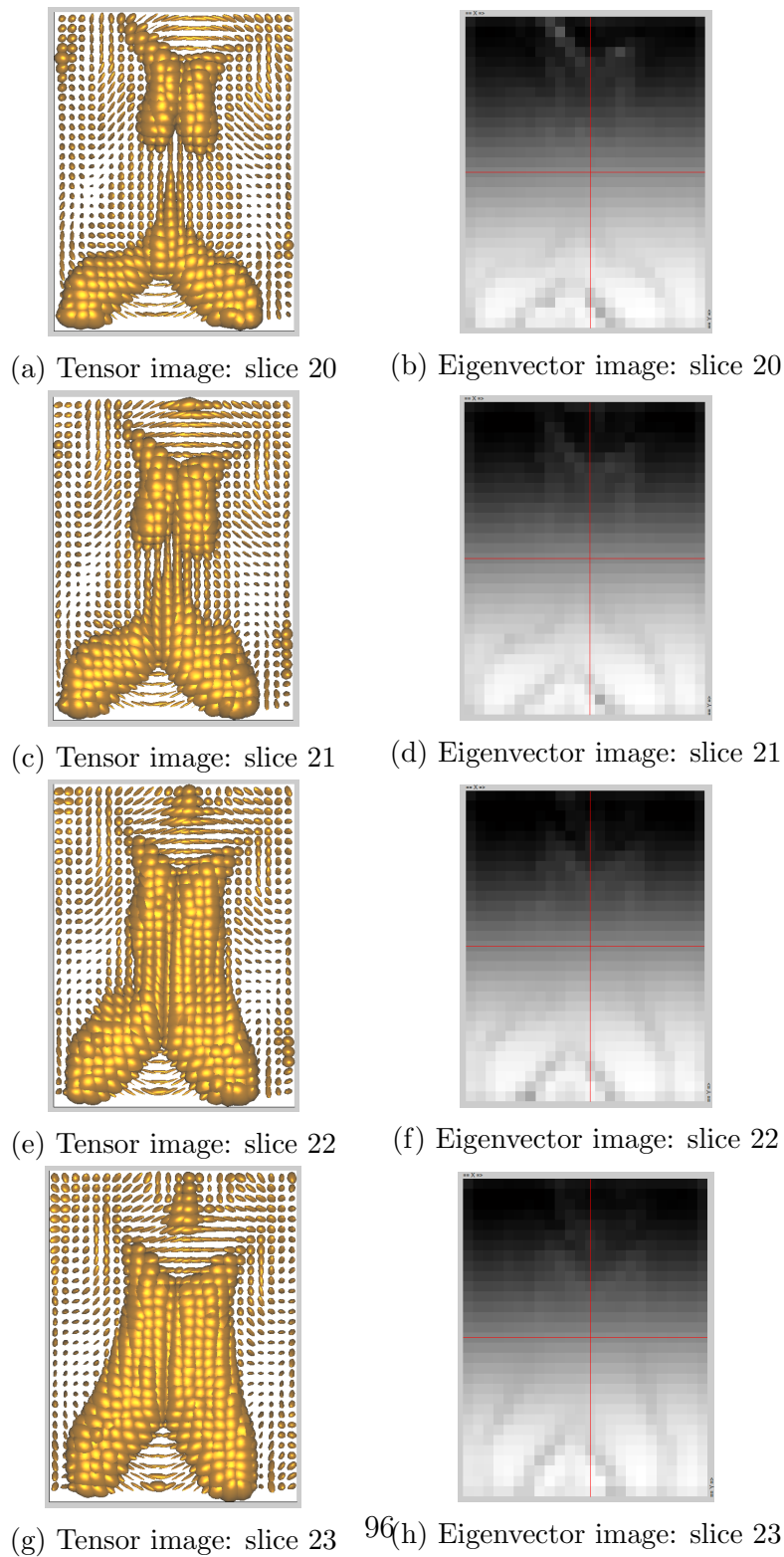


Figure 4.12: Left: A sequence of diffusion tensor images of corpus callosum (slices 20-23, axial); Right: their second eigenvector images. The eigenvector images reproduce the structures contained in the tensor images. (Dataset1)

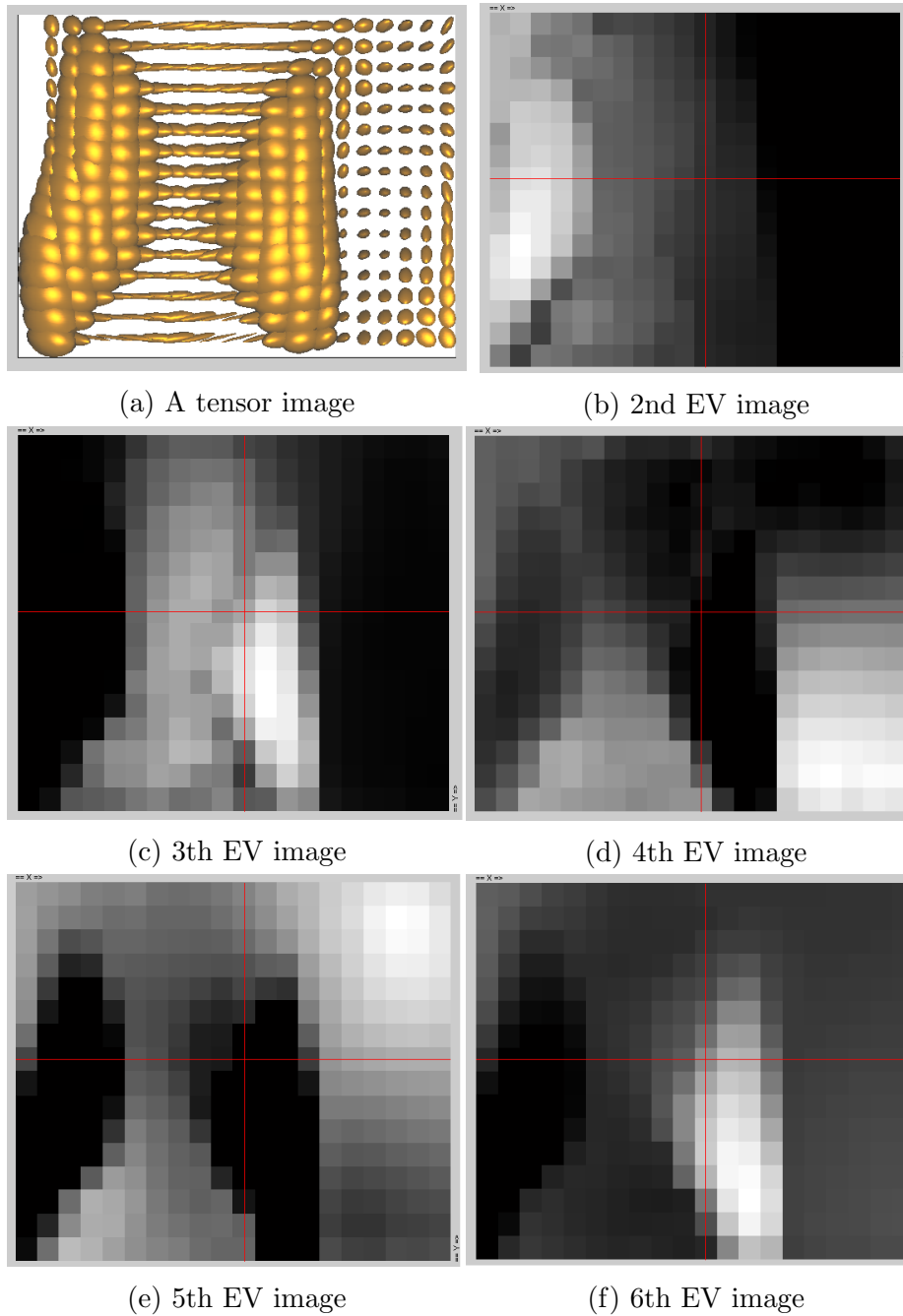
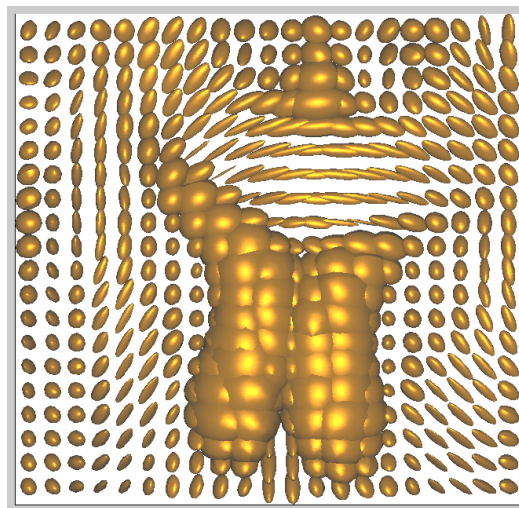
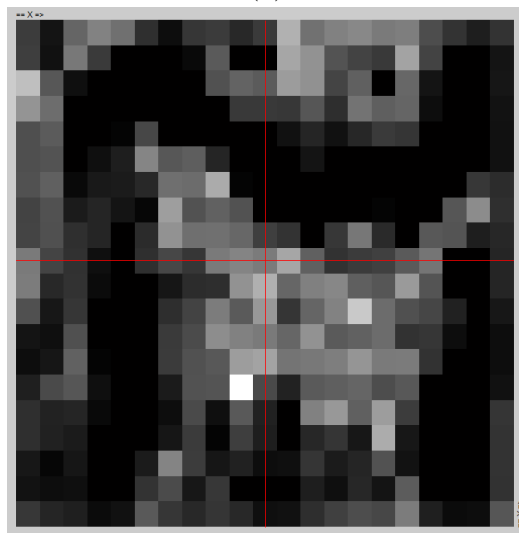


Figure 4.13: A diffusion tensor image of the ventricle (a), and its first five eigenvectors' (EV) images (b - f). The eigenvector images reproduce the structures contained in the tensor images, with different levels of clarity of the structures (axial view).



(a)



(b)

Figure 4.14: The shape-angle measure is used for computing the pairwise distances between the tensors (Dataset1). (a) A tensor image of the corpus callosum (CC) and the ventricle; (b) the second eigenvector image of (a) (axial view).

On the sagittal plane, the EV images show the corpus callosum consistently. To compute the graph edge weights for the weighted Laplacian matrix, the Riemannian affine invariant metric is used to calculate the pairwise geodesic distance.

Similarly, Fig.4.12 displays a sequence of tensor images of the CC and the corresponding second eigenvector images on the axial plane.

Fig.4.13 compares the EV images using the first 5 non-zero eigenvectors. The shape of the ventricle is visible. The geometrical information in the EV images are different, so the choice of the eigenvector used is important.

Fig.4.14 shows a tensor image of part of CC and the ventricle, when calculating the weights, the shape-angle measure is used for computing the pairwise geodesic distances.

4.3.1 The effects of graph size

Spectral graph theory is based on the eigensystem (eigenvalues and eigenvectors), computed from the graph Laplacian matrix.

Given a graph representing a 3D DT-MR image with N nodes, the size of the Laplacian matrix is $N \times N$. By definition, the eigenvectors of the graph Laplacian matrix ought to be orthogonal to each other. If N is large enough, the eigenvectors of the Laplacian matrix may become unstable. To observe this potential problem, tests are conducted at different scales, to examine the effects of the graph size.

All the regions of interest are selected from the same set of DT-MR images.

Their sizes of the chosen graphs are:

Sample 1: $20 \times 26 \times 4$ (4 axial slices), 2080 graph nodes.

Sample 2: $24 \times 31 \times 7$ (7 axial slices), 5208 graph nodes.

Sample 3: $25 \times 16 \times 19$ (19 sagittal slices), 7600 graph nodes.

Sample 4: $24 \times 31 \times 13$ (13 axial slices), 9672 graph nodes.

For each of these samples, a Laplacian matrix of $N \times N$ derived from a graph of N nodes is computed. By eigendecomposition, the eigenvalues and eigenvectors are obtained. Each eigenvector is used to construct an eigenvector image.

Figures 4.10 - 4.12 show a sequence of diffusion tensor images, alongside their second eigenvector images. The brain structures, such as the main ventricle and the corpus callusom, are identifiable.

Figure 4.13 displays the first 5 eigenvector images derived from a tensor image. The eigenvector images show the geometric information at different levels of clarity.

Figure 4.14 shows (a) a diffusion tensor image and (b) the second eigenvector image of (a). The shape-angle measure is used to compute the pairwise tensor distance. A pattern of the ventricle can be seen in (b).

Although the graph sizes are different, they can produce eigenvector images showing visible anatomical structures. The size of the eigenvector images can be $24 \times 31 \times 13$, with 9672 nodes, for instance.

4.3.2 Distribution of voxelwise geodesic distances in DT-MR images

To explore the relationship between the voxelwise geodesic distances of the tensors and the structures in a diffusion tensor MR image, the geodesic distance maps, both horizontal and vertical pairwise connections, are produced. In the distance map, the light color suggests a relatively large distance, and the dark color indicates a small distance. The two histograms display the distance distributions in the horizontal and vertical connections, respectively.

Fig.4.15 (a) shows a tensor image of CSF in part; (b) displays a light strip in column 3, indicating a gap in the tensor image, and the horizontal distance are bigger; (c) shows the vertical pairwise geodesic distance are heterogeneous; in the histogram (d) based on (b), the smallest geodesic distance values have a narrow range of high frequency, which are related to wider horizontal connections, and suggest that anisotropic tensors are aligned along the gap. The distribution is more skew in (d) than that in (e). This suggests that there is a sharp contrast in the geodesic distance distribution, hinting that a coherence structure may exist in the DT-MR image.

Fig.4.16 (a) shows the background area in a tensor image; similarly, (b) and (c) are the vertical and horizontal geodesic distance maps respectively. In both cases the trends of frequency are spreading out, suggesting there are no obvious anatomical structures.

Fig.4.17 (a) shows a tensor image of the corpus callusom and its background; in the column 7 of (b), there is a dark strip,, indicating horizontal voxelwise distances are small there. In (c), a few bright pixels are aligned obliquely, suggesting there is an edge along that direction; (d) shows that

most of the horizontal distances are not very small; (e) shows that some small vertical distances are in high frequency, implying that some tensors may align in the vertical direction.

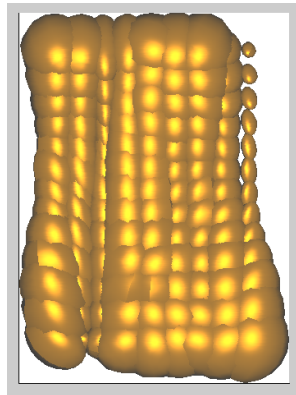
We can conclude that a distance map and a histogram are able to reveal structural information in DT-MR images. To produce an eigenvector image as seen, edge weights are computed for the weighted graph representing the diffusion tensor image, and the pairwise geodesic distances of the tensors are measured using the Riemannian affine invariant metric[55].

4.4 Conclusion

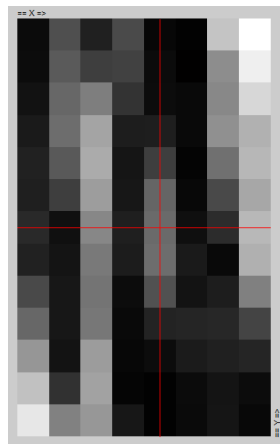
In Chapter 4, we describe the theory and core concepts of diffusion (tensor) MRI. Tests are conducted to explore the properties of the DTI. They show that the spectral graph methods are applicable to real diffusion MR images. The eigenvector images of the Laplacian matrix, derived from a graph representing DT-MR images, show the brain structures, they match those in diffusion tensor images. This provides evidence that the EV images encode geometrical information. Therefore, the spectral graph approach could be useful for the inference of the white matter fibres.

The quality of some of the eigenvector images is not satisfactory. This may be because there is noise in the nuclear MR signals, which are used for the re-construction of the diffusion-weighted MR images. The quality of the similarity measure can also affect the results. In these tests, the Riemannian affine invariant metric[55] is applied to compute geodesic distance.

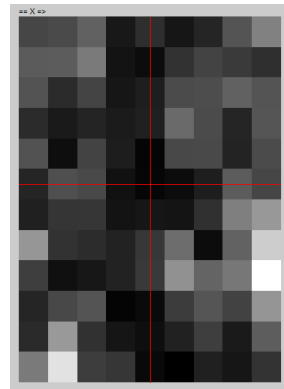
The next chapter describes how spectral graph method is used to infer



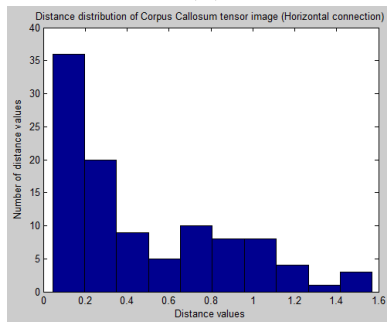
(a)



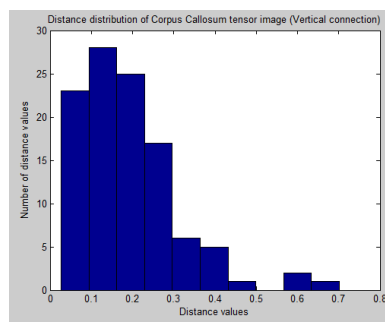
(b)



(c)

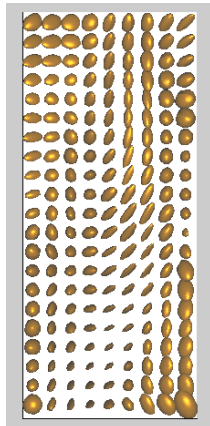


(d)

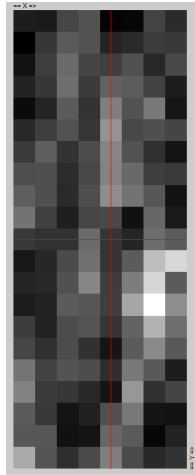


(e)

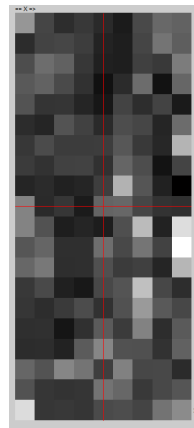
Figure 4.15: Tensor distance maps and histograms. (a) A tensor image of the CSF; (b), (c) are horizontal and vertical geodesic distance maps respectively; (d), (e) are the histograms of (b) and (c). The affine invariant metric is used to compute the pairwise tensor distance. (Dataset1)



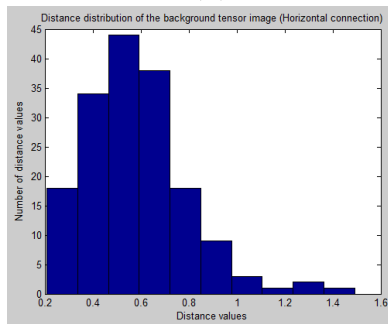
(a)



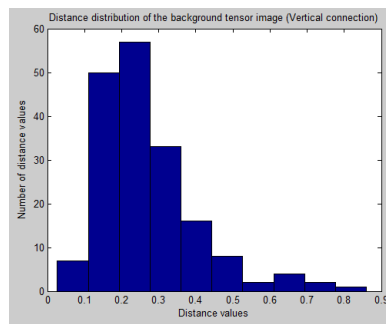
(b)



(c)

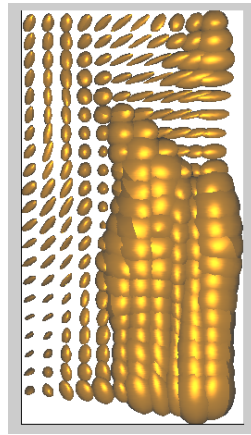


(d)

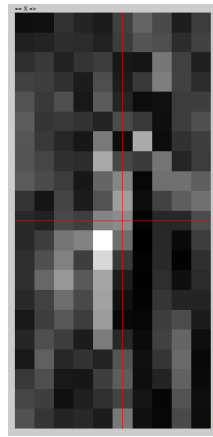


(e)

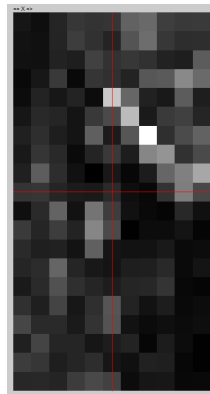
Figure 4.16: Tensor distance maps and histograms. (a) A tensor image of the background; (b),(c) are horizontal and vertical geodesic distance maps respectively; (d),(e) are the histograms of (b) and (c). The affine invariant metric is used to compute the pairwise tensor distance. (Dataset1)



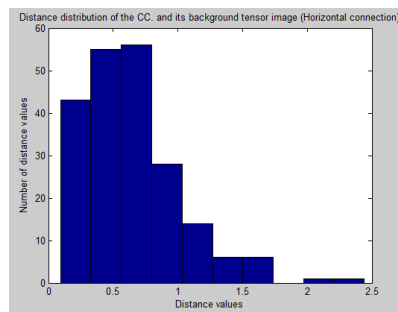
(a)



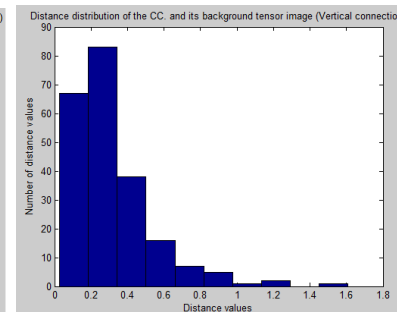
(b)



(c)



(d)



(e)

Figure 4.17: Tensor distance maps and histograms. (a) A tensor image of the CSF in part and its background; (b),(c) are horizontal and vertical geodesic distance maps respectively; (d),(e) are the histograms of (b) and (c).The affine invariant metric is used to compute the pairwise tensor distance.(Dataset1)

the white matter fibres from diffusion tensor MR images. Further similarity measures are adopted.

Chapter 5

Feature Selection for Inferring White Matter Fibres from DTI

In this chapter, we propose a framework for the inference of white matter fibres from diffusion tensor MR images of the human brain. In Chapter 6, we evaluate the proposed methodology on datasets from several brains.

The framework has the following characteristics:

- The HARDI data are used and represented by a 3D regular indirect graph
- The DTI data are computed on non-Euclidean space, namely Riemannian manifold
- Spectral graph theory is applied to generate features
- Feature selection is adopted to select the best features
- Machine learning techniques are used for the white matter fibre classification

5.1 Contributions

The contributions are: we design and implement a successful framework for inferring the white matter fibres from diffusion tensor MR images, which are transformed from diffusion MR images. Spectral graph theory is used to extract useful features from diffusion tensor data. Feature selection is applied to select the most relevant features; and machine learning is applied for inferring the cerebral white matter fibres. The proposed heuristic method, as a similarity measure, is able to achieve very good classification results. A novel methodological contribution is made.

5.2 An outline for inferring the white matter fibres from DTI

There are three stages: (a) image processing and data representation; (b) feature selection using spectral graph theory; and (c) feature selection and machine learning for neural fibre classification.

Stage1: Image processing and data representation

1. *Data preprocessing*: High angular resolution diffusion-weighted imaging (HARDI) data are processed, including image registration and the eddy current correction.

2. *Data transformation*: The HARDI images are transformed into diffusion tensor images (DTI). It is possible to extract quantitative geometric information from the DTI.

3. *Data representation*: The DTI data are represented by a weighted regular graph. The Laplacian matrix is computed, and decomposed into the eigenvalues and eigenvectors.

Stage2: Feature extraction using spectral graph theory

4. *Sample selection and labelling*: Based on each of the DTI datasets, 80 - 228 samples of $3 \times 3 \times 3$ voxels (tensors) are selected and semi-automatically labelled for machine learning.

5. *Similarity measure*: The similarity measure is a geodesic distance measure. It is required when computing the graph edge weight, or labelling a sample. Two Riemannian metrics and two proposed measures are applied.

6. *Feature extraction*: a weighted Laplacian matrix and its the graph spectrum are computed, and features are extracted from the elementary symmetric polynomial coefficients.

Stage3: Feature selection and machine learning

7. *Feature selection*: the best features are chosen by using the sequential forward selection algorithm.

8. *Infering white matter fibres from DTI*: The support vector machine (SVM) is used for two-class classification, which is a supervised learning process.

9. *Cross validation of the SVM*: ten-fold cross validation is used to train the SVM and select the best classification parameters; the resulting trained system is applied to unseen data to evaluate the performance of the classification.

The following sections describe the framework in detail.

5.3 The detailed framework of inferring white matter fibres from DTI

This section describes in detail the process of inferring white matter fibres from diffusion MR images.

The algorithm seeks to train the support vector machine for the white matter fibre classification, using the best features from feature selection. This is a process of supervised learning. The trained SVM is then applied to the unseen data, to predict new labels or classes. The algorithm is detailed as below.

5.3.1 The HARDI data and samples

Five diffusion-weighted MR image datasets are used for the study; they are denoted as dataset1, dataset2,... dataset5. The datasets 1-4 are provided by the York Neuroimaging Centre, and dataset5 is from the Human Connectome Project website (<http://www.humanconnectomeproject.org/data/>). They are diffusion-weighted MR images of healthy human brains. A description of the datasets is presented in Table 6.1.

All the HARDI datasets are transformed into diffusion tensor images (DTI) datasets, which are still called as dataset1, dataset2,...dataset5 for convenience. Each dataset covers a whole brain.

Samples are selected semi-automatically from each DTI dataset, for fibre

classification through machine learning. A sample refers to $3 \times 3 \times 3$ image voxels, 27 tensors in total. The higher the image resolution, the more samples can be selected. For the 5 datasets, 80, 160, 160, 148, 228 samples are selected respectively. They are labelled afterwards.

5.3.2 Semi-automatic sample labelling

Labelling a tensor sample, as fibre or non-fibre, is crucial for supervised learning in this study. The labelling is for training a classifier, it also provides the baseline for computing the accuracy of classification. To label a sample semi-automatically, a few selection criteria are applied, both the shape and the orientation of the tensor are considered. The tensor is described as a physical object[7], which can be spherical, prolate (linear) and oblate (planar) shaped. Only the linear shaped tensors are relevant to the inference of the white matter fibres.

The semi-automatic labelling algorithm is described as follows:

1. With the diffusion tensor images, a label map is produced for every 3 images, from which a $3 \times 3 \times 3$ sample of 27 tensors is labelled, one sample after another, as if a three dimensional window is sliding from one sample to the next. For every sample, a graph is produced to represent the data. By eigendecomposition, 27 eigenvalues and eigenvectors are produced. The eigenvalues are sorted by ascending order and their corresponding eigenvectors are found.
2. To depict the tensor orientations in a sample (27 tensors), the variance of the tensor angles about the mean is calculated.

For each sample, based on the principal eigenvectors of the tensors, the mean principal eigenvector P is computed. Afterwards, the angle between each tensor's principal eigenvector M about the mean principal eigenvector P is computed respectively, and an average taken.

The sign of the principal eigenvector has uncertainty, and so an extra step is needed to check the sign. If the inner product of M and P is negative, then the sign is flipped. Thus, the variance of angles of the sample is computed.

3. To extract the shape information, the *Fractional Anisotropy* (FA) and the Westin shape indices [74] are integrated (see section 4.2.3).

The shape and the orientation of the tensor are depicted by its eigenvalues and eigenvectors respectively. The eigenvectors describe the principal diffusion directions and apparent diffusivity along these directions [43], while the eigenvalues describe the shape of the tensor.

Westin indices can be used to approximately indicate the tensor shapes. As mentioned, we consider the tensor having one of the 3 types of shapes: spherical, ellipsoidal (prolate) or oblate. If $\lambda_1 = \lambda_2 = \lambda_3$, then the shape of the tensor is spherical; if $\lambda_1 \gg \lambda_2 = \lambda_3$, it is a prolate ellipsoid; if $\lambda_1 \ll \lambda_2 = \lambda_3$, it is oblate, or planer. Their values are between 0 and 1.

4. The threshold used for identifying the shape of the tensor is chosen as below: If the C_s value is greater than 0.40 the tensor is considered as a spherical in shape and excluded; otherwise if both the Westin index[74], C_l value, is greater than 0.35 and FA values are greater than 0.45, the tensor is considered as prolate in shape, so the number of prolate shaped tensor is increased by one. For every sample of 27 tensors, a *prolate score* is computed, which is the ratio of the number of the prolate shaped tensors to the 27

tensors.

5. Labelling a sample with the shape and orientation information. For each sample, if the variance of all the tensor angles about the mean angle is less than or equal to a threshold (e.g. 10 or 12 degrees) and if the prolate score is greater than 0.5, then this sample is labelled as *fiber*, otherwise as *non-fiber*.

6. Repeat the above. Finally, a label map is created (Figure 5.1 (a)), based on the three tensor images (Figure 5.1 (b))

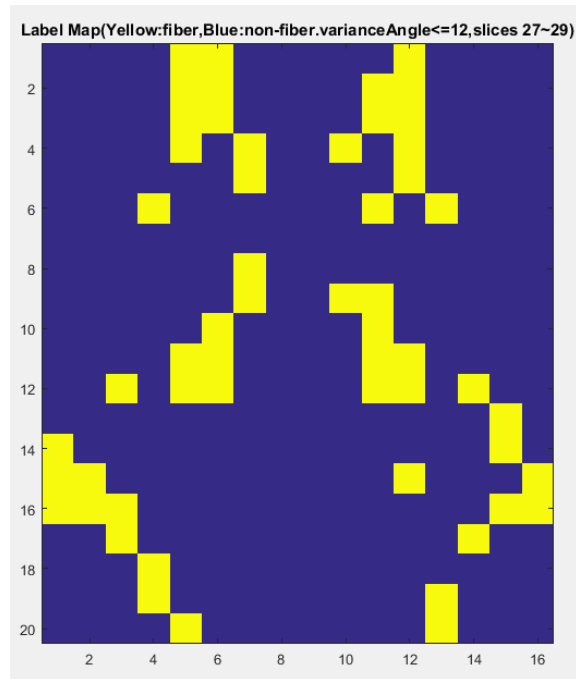
The label map is consistent with visual observation of the tensor image. Although only one tensor image is displayed, 3 tensor images are used to produce a label map.

5.3.3 Feature extraction from the elementary symmetrical polynomials

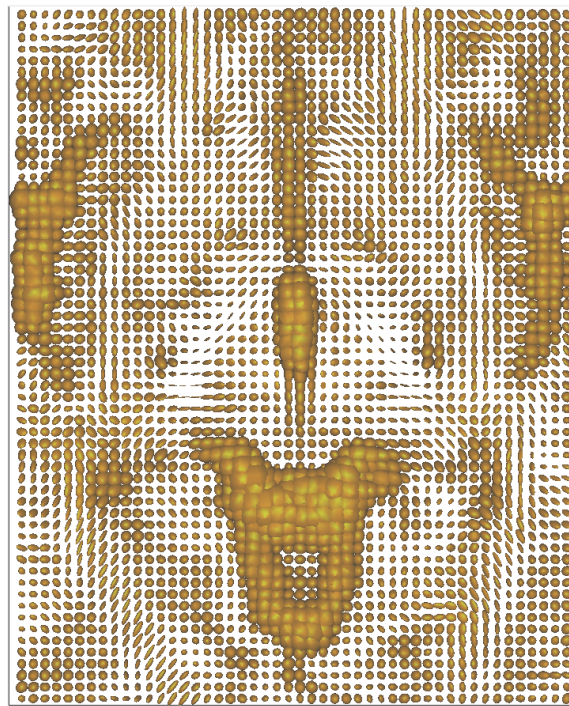
Features are the essential elements for machine learning. In this study, the elementary symmetric polynomials (ESPs) are used to generate the features, which are used to infer the white matter fibres.

The overall procedure consists

- (a) computing the weight Laplacian matrix, and constructing the feature matrix.
- (b) computing the ESP values, based on the feature matrix.
- (c) constructing the ESP feature matrix.



(a) A lable map



(b) One of the three tensor images used for creating the label map.

Figure 5.1: A label map and an associated tensor image (Dataset2). Three diffusion tensor images are used to create the label map.

Computing the weighted Laplacian matrix

Each of the samples is represented by a regular graph, where a node represents an image element, namely a diffusion tensor. The weight of a graph edge is associated with the geodesic distance between the two adjacent nodes (tensors).

First, the weighted adjacency matrix representing a sample is computed, and the weight is calculated by

$$weight = e^{-\frac{(d_{D_1 D_2})^2}{K^2}} \quad (5.1)$$

where D_1 and D_2 represent two 3×3 tensors, K is a parameter for the Gaussian distribution (the width of the Gaussian kernel), and $d_{D_1 D_2}$ is a geodesic distance between D_1 and D_2 .

Second, the Laplacian matrix, L , is produced:

$$L = D - W \quad (5.2)$$

where D is the degree matrix and W is the weighted graph adjacency matrix.

The steps of the computation of W are:

1. Based on the adjacency matrix of the graph, the indices are assigned to the nodes. For the pairwise nodes, their indices are stored in a $N \times 2$ matrix, N denotes the number of the pairs of direct connected nodes, and 6-connection is applied.
2. The graph edge weight is computed for each pair of nodes and stored in a vector.

3. By using the edge weights and the node indices, a weighted graph, W , is constructed.

Computing the spectral matrix

The Laplacian matrix can be decomposed into eigenvalues and eigenvectors, known as the graph spectrum, which are combined to form a spectral matrix [77]:

$$\Phi = (\sqrt{\lambda_1}e_1, \sqrt{\lambda_2}e_2, \dots, \sqrt{\lambda_n}e_n) \quad (5.3)$$

where λ_i and e_i ($i = 1, 2, 3, \dots, n$) are the eigenvalues and eigenvectors of the Laplacian matrix L , given by

$$L = \sum_{i=1}^n \lambda_i e_i e_i^T \quad (5.4)$$

T means the transpose operation.

Computing the values of the elementary symmetric polynomials

The elementary symmetric polynomials are created by using the spectral graph theory; they can be used to produce pattern vectors. This is described by Wilson et al.[77] as follows.

The spectral matrix consists n scaled eigenvectors as columns (see Equation 5.3), which is used for feature extraction. As shown in Figures 4.10 - 4.12, the eigenvalues and eigenvectors contain geometric information of shape and orientation. We need the features containing structural information of the DT-MR images, in particular, those of the white matter fibres.

For a set of variables v_1, v_2, \dots, v_n , The ESPs are defined as below

$$\begin{aligned}
S_1(v_1, v_2, \dots, v_n) &= \sum_{i=1}^n v_i, \\
S_2(v_1, v_2, \dots, v_n) &= \sum_{i=1}^n \sum_{j=i+1}^n v_i v_j, \\
&\vdots \\
S_r(v_1, v_2, \dots, v_n) &= \sum_{i_1 < i_2 < \dots < i_r} v_{i_1} v_{i_2} \dots v_{i_r}, \\
&\vdots \\
S_n(v_1, v_2, \dots, v_n) &= \prod_{i=1}^n v_i.
\end{aligned}$$

The power symmetric polynomial functions are

$$\begin{aligned}
P_1(v_1, v_2, \dots, v_n) &= \sum_{i=1}^n v_i, \\
P_2(v_1, v_2, \dots, v_n) &= \sum_{i=1}^n v_i^2, \\
&\vdots \\
P_r(v_1, v_2, \dots, v_n) &= \sum_{i=1}^n v_i^r, \\
&\vdots \\
P_n(v_1, v_2, \dots, v_n) &= \sum_{i=1}^n v_i^n,
\end{aligned}$$

Here $v_i = \sqrt{\lambda_2} e_i$ and v_i^r means that for vector v_i the pointwise raise to power. The arguments of the polynomials above are the elements of the spectral matrix. The values of the symmetric polynomials are used to construct the feature matrix. The two sets of polynomials are associated by the Newton-Girard formula:

$$S_r = \frac{(-1)^{r+1}}{r} \sum_{i=1}^r (-1)^{k+r} P_k S_{r-k} \quad (5.5)$$

For each sample, a graph Laplacian matrix is created. The spectral matrix and the ESP feature matrix are computed.

Constructing the ESP feature matrix

For each sample of a DTI dataset, the values of the first 6 polynomials, S_1, S_2, \dots, S_6 , are computed and stacked to form a long feature vector. All the samples' long feature vectors are computed and form an ESP value matrix, which can be used for feature selection. Any number of the polynomials can be used to construct a feature vector, but the feature dimension should be less than the number of samples.

The first value of the $S_i (i = 1, 2, \dots, 6)$ is always zero, so it is discarded. Then these feature vectors are merged column by column into a two dimensional matrix, known as the feature data matrix or feature matrix. In practice, the feature matrix is truncated to preserve the useful values, and those polynomial values corresponding to the very small eigenvalues are removed. This ensures that the eigenvalues of the covariance matrix of the feature matrix are real numbers.

A feature matrix is useful, since every element of it has an index, which overcomes the difficulty of indexing in an unordered graph structure. The feature matrix is used for classification. The feature matrix can be very large. For example, Dataset1 has 80 samples; half of them are chosen as the training set, and the other half are the testing set. The feature matrix of polynomial values hence has the size of 156×40 , as the ESP values are from

the first 6 items, S_1, S_2, \dots, S_6 , each of the $S_i (i = 1, 2, \dots, 6)$ has 26 values, corresponding to 26 non-zero eigenvalues.

Figure 5.2 shows that the eigenvalues of the covariance matrix of the feature data matrix are well separated into two parts. Here we use 80 samples of dataset1, in which 40 samples are for training and the other 40 samples are for testing.

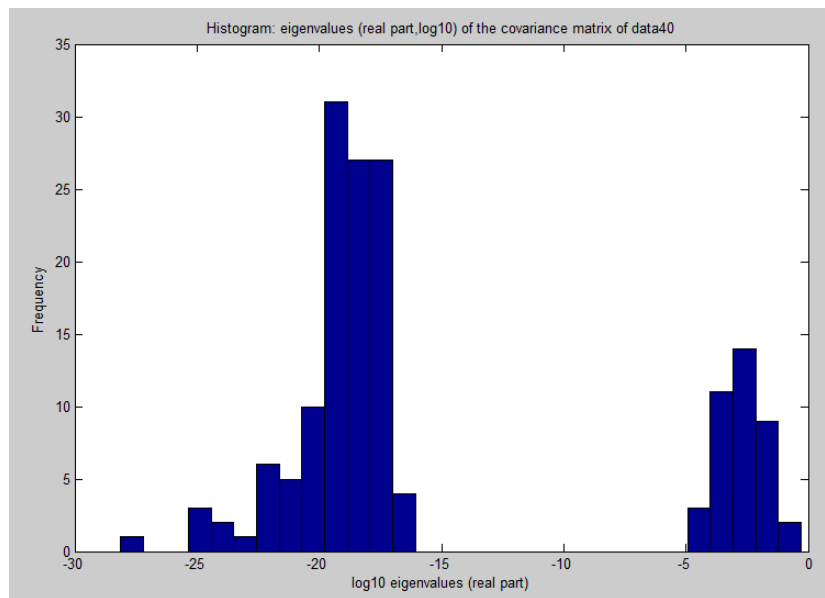


Figure 5.2: A histogram of the log10 eigenvalues of the covariance matrix of the feature data matrix. The figure shows that the log10 eigenvalues are clearly separated into two parts, this suggests that the left part with very small eigenvalues can be discarded.

Given the feature matrix has the size of 156×40 , the covariance matrix of the feature matrix has the size of 156×156 . By eigendecomposition, 156 eigenvalues and eigenvectors are obtained. However, only a small portion of them are real numbers. We produce a histogram of these log10 eigenvalues (Figure 5.2) to see if it is possible to split them into useful and non-useful

parts. The log10 eigenvalues are naturally divided by two distinctive parts: the small part represents 39 real eigenvalues, while the rest are complex eigenvalues although only the real parts are displayed. Thus, we choose 39 rows of the feature data matrix, which are the polynomial values.

In general, if the number of samples is N , then the chosen number of features, or feature dimension, would be $N - 1$. The size of an ESP feature matrix is $(N - 1) \times N$. This feature matrix can be the input for the feature selection algorithm.

5.3.4 Feature selection

When humans perform object classification and pattern recognition problems, only a few attributes, called *features*, are needed. For example, the nose, the eyes and the mouth can be the features for face recognition.

Feature selection can make machine learning more effective. Although the number of features being used is unlimited, keeping this number to a minimum is necessary to avoid the *curse of dimensionality* [71]. Feature selection removes redundant and irrelevant information that may have an adverse effect on the classifier performance. The purpose of feature selection is to select the best subset X of d features.

The sequential forward selection algorithm is used to achieve feature selection; and the criterion used for that is the Fisher discriminant ratio.

Sequential forward selection algorithm

The *Sequential Forward Selection* (SFS) algorithm [26] is a simple bottom-up search procedure.

Mathematically, the SFS algorithm is initialised by setting a vector X_0 as an empty set, k features are then selected to form a feature set X_k . Ranking the elements, ζ_j , of the set of available measurements, $Y - X_k$, so that

$$J(X_k + \zeta_1) \geq J(X_k + \zeta_2) \geq \dots \geq J(X_k + \zeta_{D-K}).$$

The feature set X_{k+1} is given as $X_{k+1} = X_k + \zeta_1$. J represents the selection criterion, namely the Fisher discriminant ratio (equation 5.8).

The SFS algorithm selects successive features with reference to the current set of features, and the new enlarged feature set generates a maximum value of the criterion function used. The statistical dependence between measurements is considered, so the features set selected is good. The best subset is produced by the combination of d features that optimises a criterion function. Using different criteria can result in selecting different features. However, the SFS has the nesting phenomenon: the feature sets X_k , $k = 1, 2, \dots, d$ are nested[26].

Search strategy for feature selection

A search strategy is applied to determine the best combinations of d features out of D measurements, by evaluating each individual feature set. The number of evaluations, q , is given by the combination formula:

$$q = \binom{D}{d} = \frac{D!}{d!(D-d)!}$$

where D is the number of features, d is the number of features to be selected. Since q can be a large value of combinations, direct exhaustive search is not a practical solution, thus a computationally feasible algorithm is sought.

Fisher discriminant ratio

The *Fisher discriminant ratio* is a well known criterion for class separability, which is used here. It maximises the ratio of the between-class data separation to the within-class data separation. It is described as the following by Devijver and Kittler [26].

The mixture population covariance matrix is denoted by

$$\Sigma = E\{(\bar{x} - \bar{\mu})(\bar{x} - \bar{\mu})^T\}, \quad (5.6)$$

where E is the expected value. \bar{x} is the d -dimensional feature vector, and $\bar{\mu}$ is the class population mean. T means *transpose*. Then the total covariance matrix, also known as the total scatter matrix, S_T , is denoted as

$$S_T = |\Sigma| = |S_w + S_b|, \quad (5.7)$$

where $|\Sigma|$ is the determinant of Σ , S_w represents the within-class scatter matrix, and S_b represents the between-class scatter matrix. The greater the ratio of the between- and within-class scatter, or of the total- and within-class scatter, the greater the spatial separation of classes. The ratio is depicted as

$$J(\zeta) = \frac{|\Sigma|}{|S_w|}, \quad (5.8)$$

Alternatively,

$$J(\zeta) = \prod_{j=1}^d (1 + \tilde{\lambda}), \quad (5.9)$$

where $\tilde{\lambda}$ is an eigenvalue of the product $S_w^{-1}\Sigma = I + S_w^{-1}S_b$. The Σ is the covariance matrix of the data matrix and I is the identity matrix. S_w^{-1} is the

pseudo-inverse of S_w .

5.3.5 Machine learning and SVM classification

There are two strands of categorising data in machine learning: (a) supervised learning and (b) unsupervised learning. The former uses labelled data to train a classifier, which is applied to the unseen data to predict the new labels, or the classes, this process is known as *classification*; while the latter does not require the data to be labelled, certain rules are applied to the group data, called *clustering*. In this study, supervised learning is adopted for fibre classification.

The support vector machine (SVM) is used for supervised learning [33]. The trained SVM is applied to the unseen testing data to predict new labels for them. The prediction accuracy rate, or classification accuracy rate, is the ratio of the number of correctly predicted new labels against the number of assigned labels. The classification accuracy indicates how well the SVM classifier would perform on the new data.

5.3.6 Cross validation of the SVM

The purpose of cross validation is to examine the accuracy and the robustness of a SVM, and to select the best parameters for the SVM.

Ten-fold cross validation is carried out. The samples of a training set are divided into 10 equal portions, from which 9 portions are used to train a SVM classifier, while the rest is for testing. For each fold, a different portion is chosen as a testing set, and the rest are the training set.

The SVM is trained through ten-fold validation; the best parameters are applied to the training set to build a SVM that can then be used for classifying the unseen data. The ten-fold validation results in 10 classification rates; a set of the best parameters are identified if they achieve the best classification accuracy rate.

So far, we have explained the framework of inferring the white matter fibres in length. This is a pipeline, from HARDI data process, feature extraction, feature selection, to machine learning and classification. This framework is evaluated by applying it to real world data in chapter 6. But first, we explore certain properties of stages in the pipeline.

5.4 Exploring geometric relationship of the tensors

The inference of the white matter fibre is associated with the pairwise tensor distance measured on the Riemannian manifold; statistic measurements are on the curved surface. Hence, it is necessary to examine what impact would be on the similarity measure for shape analysis.

In this section, several tests are carried out, to study the spatial relationship between the tensor angle, geodesic distance, the metrics and the ratio of eigenvalues. These properties are useful for similarity measurement. Dataset1 is used for all the tests unless stated.

5.4.1 Test 1: Shape-angle distance vs. affine invariant distance

The Riemannian metrics and the proposed measures are introduced in Chapter 4. They are used to compute the geodesic distance of the tensors. This test further explores their spatial relationship. The affine invariant metric[55] and the proposed shape-angle measure are examined.

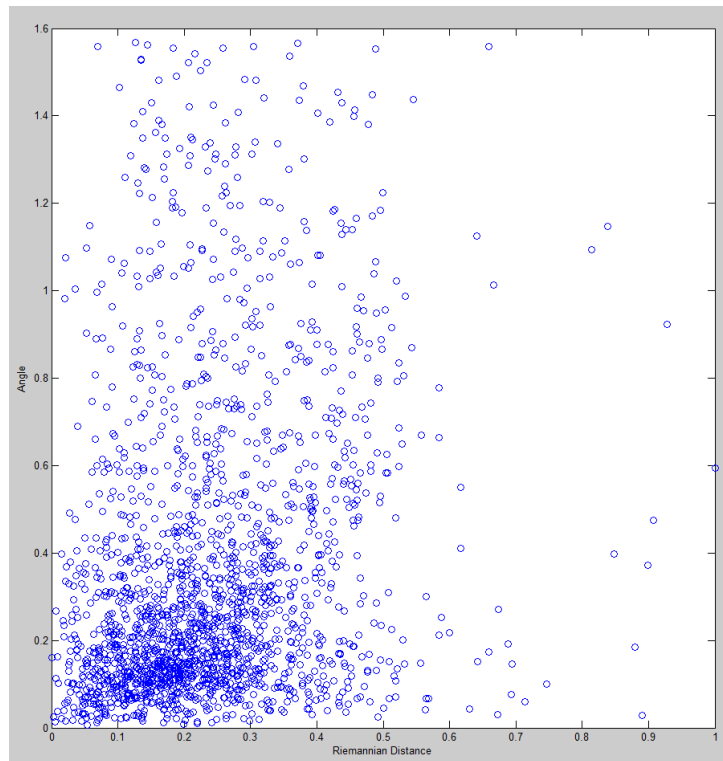


Figure 5.3: The relationship between geodesic distance and the angle of pairwise tensors of a data graph. The affine invariant Riemannian metric is used to compute the tensor distance. The X-axis is the Riemannian geodesic distance, the Y-axis is the angle.

Figures 5.3 and 5.4 show that the geodesic distance computed by the

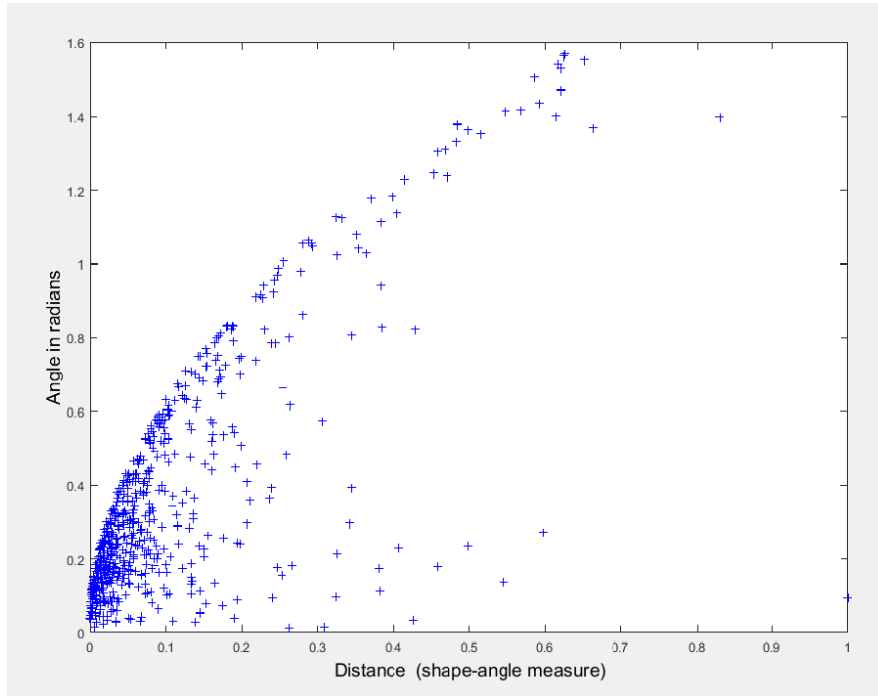


Figure 5.4: The relationship between geodesic distance and the angle of pairwise tensors of a data graph. The shape-angle measure is used to compute the geodesic distance of paired tensors.

affine invariant metric and the shape-angle measure, they are proportional to the angle of tensors. This reveals that the angle measure is compatible with the distance measure of the tensors, or vice versa. So the angle of tensors can be used for similarity measure for shape analysis. When two tensors are parallel or near parallel to each other, the distance and the angle tend to be small. They can be indicators of the white matter fibres lying underneath the tensor images.

Figure 5.5 shows the relationship between the tensor distance using affine invariant metric and the tensor distance using the shape-angle measure. They are largely positively related.

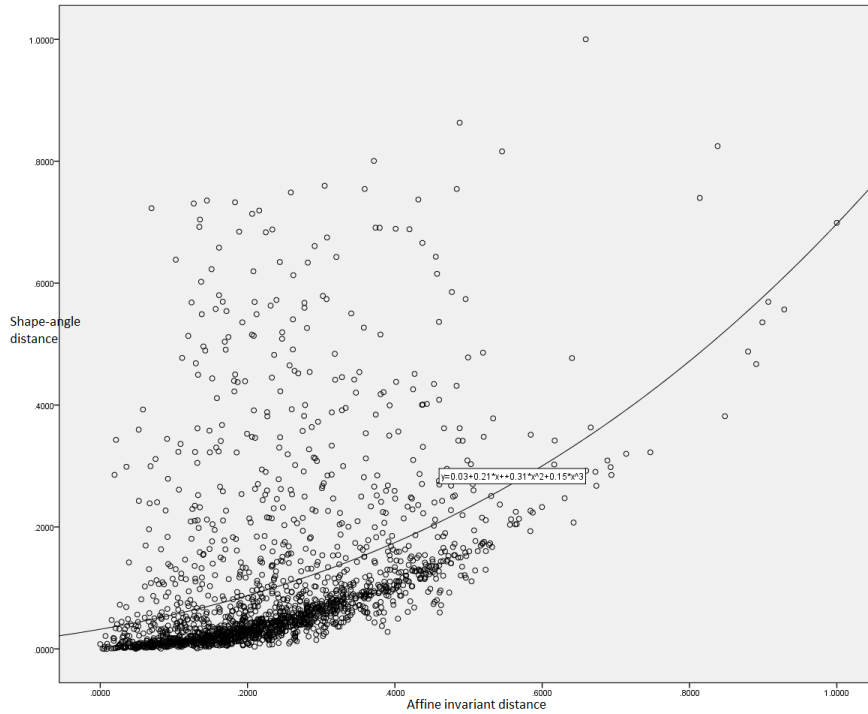


Figure 5.5: The relationship between the affine invariant distance and the shape-angle distance, different measures are used.

5.4.2 Test 2: The effects of changing the angle of the tensor

This test is to explore the relationship between angle of the tensor and curvature of the circular tensor field.

Figure 5.6 shows that when the radius of the circle becomes larger, the principal directions of the two adjacent tensors on the same radial line tend to be parallel; while when the radius is small and near the center of the circle, the principal directions of the tensors change rapidly. This simulates the situation when a fibre bundle gradually changes its direction with different

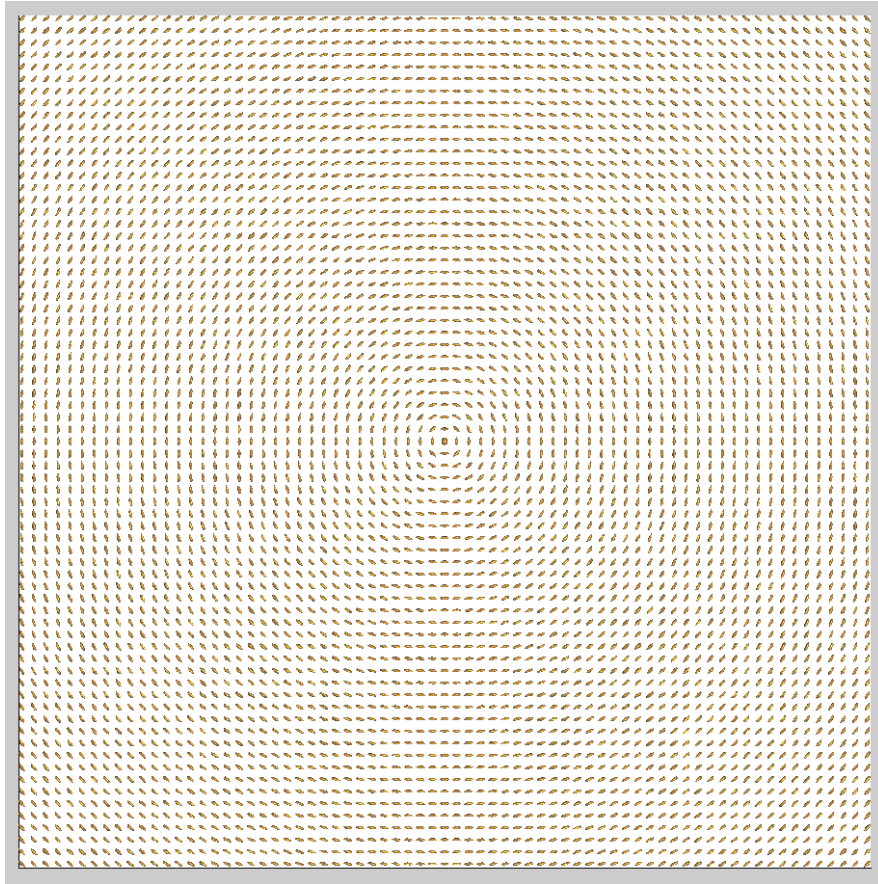
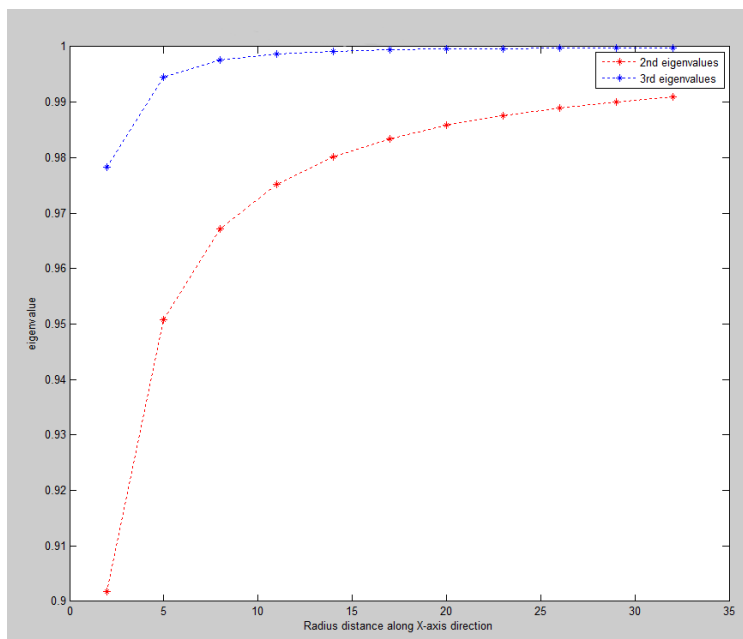


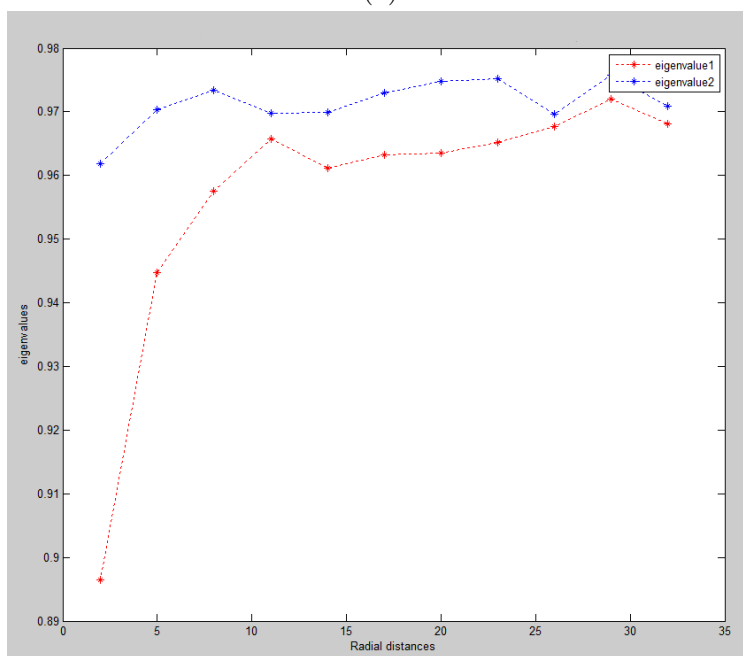
Figure 5.6: Tensors in the circular field. The tensors sit along the tangents of the circle at different points, with different radii. The tangent direction is parallel to the principal eigenvector direction of the tensor.

curvatures. The test suggests that the principal eigenvector of the tensor can be used to depict the curvature of the white matter fibre tracts.

Eigenvalues of the tensor can be useful for structure detection in DTI image analysis. Figure 5.7 describes the changes of the second and third eigenvalues along the X-axis in the tensor field. The former has no noise added, while the latter has Gaussian noise added with a standard deviation of 0.005.



(a)



(b)

Figure 5.7: The second and the third eigenvalues vs. radial distance along the X-axis. (a) without adding noise; (b) Gaussian noise is added to the eigenvalues (sd.0.005).

In the test, a set of 3×3 samples are selected along the X-axis, the eigenvalues and eigenvectors of the tensor are computed via eigendecomposition. When the radial distance increases, the eigenvalues of the tensor changes smoothly, and the curvature of the tensor's trajectory changes smoothly, too. After the Gaussian noise is added, this trend largely remains the same.

In the circular tensor field, the second eigenvalue increases when the radii distance getting bigger along the X-axis (or Y-axis). The curve of the third eigenvalue is quite flat. The two curves are distinguishable, even when Gaussian noise is added. Figure 5.7(b) shows that by adding the Gaussian noise, the trend of the curves remain similar. It reveals that the second eigenvalues change smoothly along the radial distance, and are useful for distinguishing the tensors as different in position and orientation.

5.4.3 Test 3: The effects of the ratio of eigenvalues

This test is to examine if the ratio of the eigenvalues derived from the tensor can characterise the white matter fibres. Figures 5.8 and 5.9 are the images of the ratio of eigenvalue1 to eigenvalue2, and that of eigenvalue1 to eigenvalue3. The major white matter bundles (e.g. genu/splenium of the corpus callosum) in the two images appear in the bright light blue.

A few negative eigenvalues (the dark spots) appear at the edge of the brain images. They may be a result of MRI signal truncation.

Figure 5.10 shows the images of the ratio values of eigenvalue2 to eigenvalue3; the contrast of the white matter fibre tracts to the background in the image is relatively weak. This is because the difference of their values are small, so they are not suitable for inferencing the fibres.

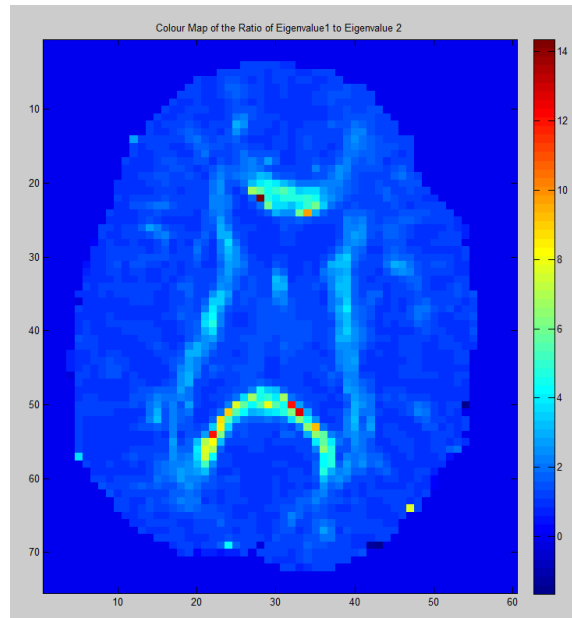


Figure 5.8: A map of the ratio values of eigenvalue1 to eigenvalue2

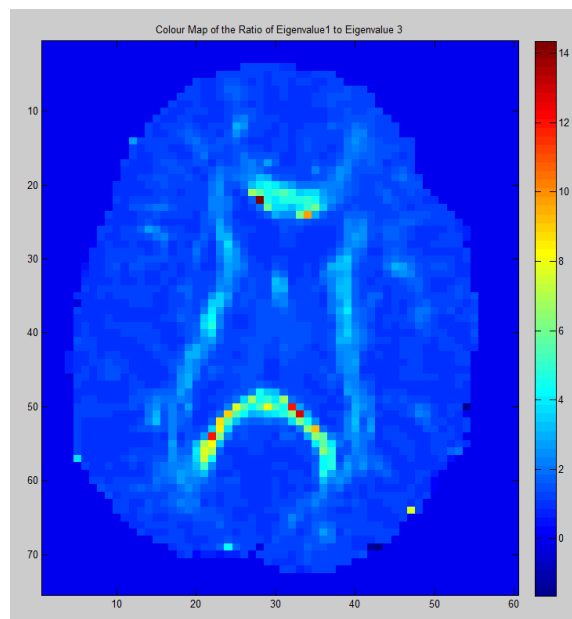


Figure 5.9: A map of the ratio values of eigenvalue1 to eigenvalue3

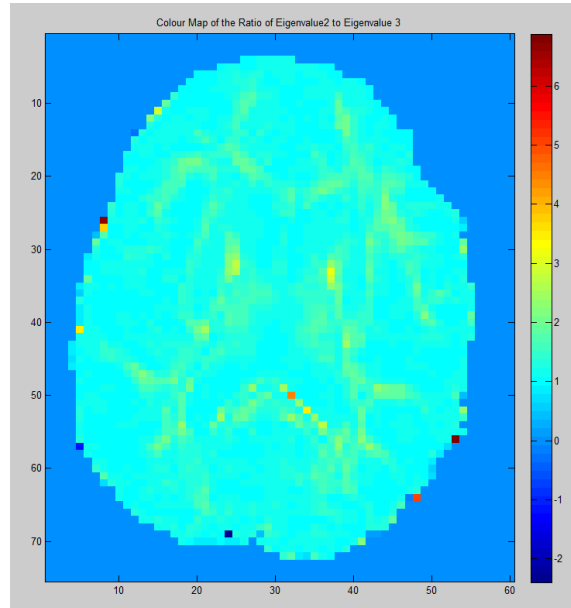


Figure 5.10: A map of the ratios of eigenvalue2 to eigenvalue3

By comparison, the ratio of eigenvalue1 to eigenvalue2 and the ratio of eigenvalue1 to eigenvalue3 can be useful for inferring the white matter fibres.

5.4.4 Test 4: Affine invariant metric vs. shape-angle measure

Pennec et al. propose the affine invariant Riemannian metric [55]; while we develop the shape-angle measure for computing the geodesic distance of tensors. Their compatibility is examined here.

Figure 5.11 shows that all the curves computed by using the affine invariant metric are smooth, stable, continuous and sensitive to small change in distance. The angle of the tensor is changed from 0 to 360 degrees with a 10-degree interval. The tensor's radial axes are changed from 0.1 to 1,

meaning its shape changes from linear to spherical. This is reflected by the different colours of the curves.

In Figure 5.11, the geodesic distance between the two adjacent tensors are computed, using the shape-angle measure. The tensor angle changes from 0 to 180 degrees at a 20-degree interval, and the tensor shape also changes from linear to spherical.

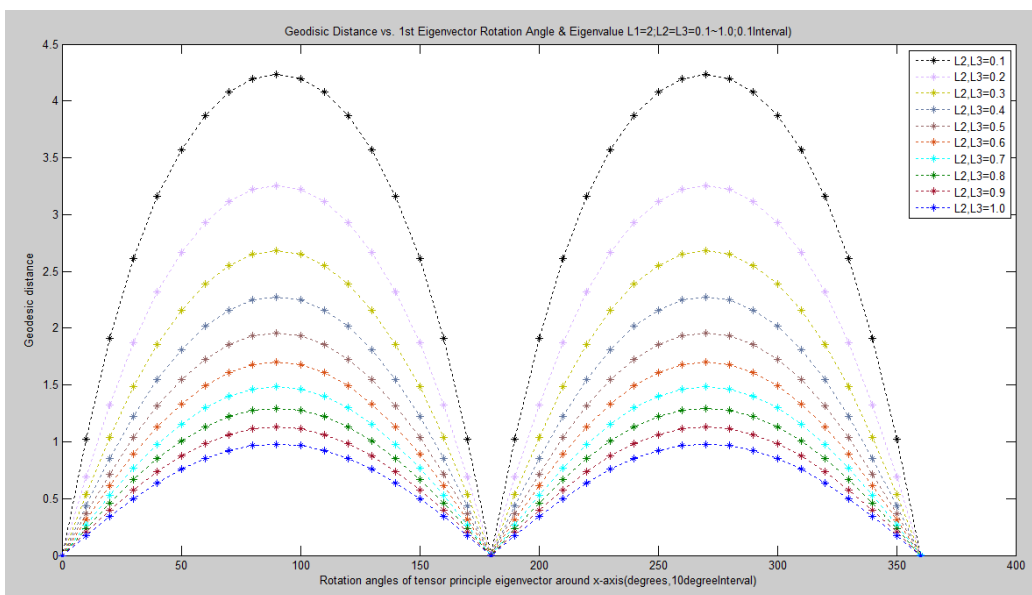


Figure 5.11: The curves show the changing geodesic distance, measured by Penneç’s affine invariant metric. The tensor angle is changed from 0 to 360 degrees, at an interval of 10 degrees. Different curves show the distances while the tensor’s radial axes (L2 and L3) changing from 0.1 to 1.0, or from linear to spherical shaped.

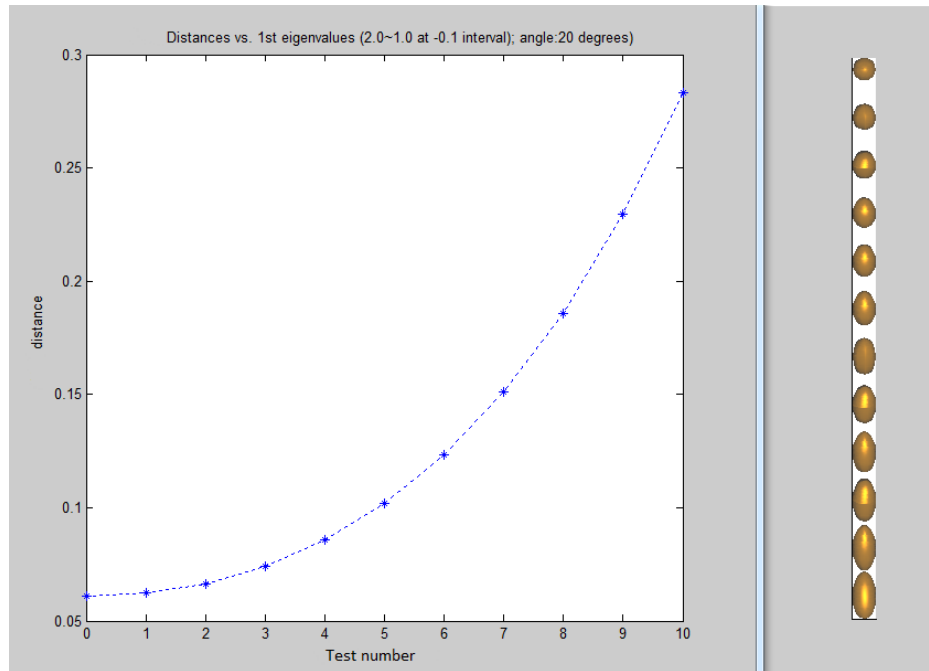


Figure 5.12: The tensor distance computed by the shape-angle measure. The curve shows the distance values changing smoothly, while the tensor angle changes from 0 to 180 degrees at an interval of 20 degrees; the principal eigenvalue of the tensor changes from 2.0 to 1.0, meaning that the tensor shape changes from linear to spherical.

5.5 Summary

Chapter 5 presents a framework for inferring the white matter fibres from diffusion tensor images. The highlights of this framework are:

- The spectral graph theory is used for the characterisation of white matter fibres in 3D diffusion tensor MRI images of the human brain
- Useful features are extracted from the elementary symmetrical polynomial values, derived from the eigensystem of the spectral matrix, which is associated with the Laplacian matrix of the data graph

- Feature selection and machine learning techniques are applied, for the inference of the white matter fibres

Tests are conducted prior to the implementation of the framework. The qualitative results show that the change of the geodesic distance between the tensors are smooth. The ratios of the eigenvalues derived from the tensor are geometrically informative.

Tests are applied to explore the relationship between the geodesic distance and the angle of paired tensors; the changing curvatures of the angles of the tensors in a circular tensor field; and the effects of the ratio of eigenvalues. The results suggest that both eigenvalues and eigenvectors would be useful for shape analysis in diffusion tensor MR images.

Chapter 6

Evaluation of Methodology for Inferring White Matter Fibres

In Chapter 5, we present the methodology of inferring the cerebral white matter fibres from diffusion tensor MR images. The inference is achieved through graph based feature extraction, feature selection, supervised machine learning for classification, to distinguish the white matter fibres from the background.

This chapter describes an evaluation of the methodology. It studies the techniques of feature extraction and feature selection; the use of the support vector machine (SVM) models and their performance; the use of cross validation to select the best parameters; the classification accuracy on DTI samples; and the generalisability of the SVM models - how well the SVM models can be used to predict the white matter fibres in new data.

6.1 Datasets and experiment design

The evaluation of the inference methodology is based on diffusion tensor MR images, derived from diffusion-weighted MR images, namely the HARDI data. Five DTI datasets with different image resolution are used. A description of the datasets used in this study is displayed in Table 6.1.

The HARDI image acquisition used diffusion weightings (isotropic $b = 1000 \text{ s/mm}^2$) in multiple directions (e.g. 62, 69, 288), with a magnetic field of 3 Tesla. Along each diffusion direction, a 3D volume of diffusion weighted MR dataset is produced. For example, Dataset1 (diffusion weighted MR data) has 62 volumes, since 62 gradient directions were applied respectively during data acquisition; all the volume has the same size: $128 \times 128 \times 44$ voxels (44 slices), meaning that there are 44 slices of images with 128×128 resolution. The number of diffusion directions is equal to that of data volumes.

Table 6.1: Data Description

Dataset	Volume size (voxel)	Voxel size (mm^3)	Dataset size (volume)
1	$128 \times 128 \times 44$	$2.5 \times 2.5 \times 2.5$	62
2	$98 \times 103 \times 74$	$2.0 \times 2.0 \times 2.0$	69
3	$98 \times 103 \times 74$	$2.0 \times 2.0 \times 2.0$	69
4	$98 \times 103 \times 74$	$2.0 \times 2.0 \times 2.0$	69
5	$145 \times 174 \times 145$	$1.25 \times 1.25 \times 1.25$	288

The inference of the white matter fibres is based on supervised machine learning. The DTI samples of $3 \times 3 \times 3$ tensors are selected as described in section 5.3.2. The overall strategy of the evaluation is designed as follows:

Firstly, using the DTI samples from one brain: 50% were randomly sampled 30 times for the experiments, which are used for training a SVM

model, while the rest of the samples are used as a testing set, or the unseen data. Datasets 1, 2, ..., 5 are used for these experiments. This evaluates how well a model trained on part of a brain generalises to a different part of the same brain.

Secondly, using the DTI samples from two brains: the samples obtained from one brain form a training set, while that from the other brain are used as a testing set. The datasets 2, 3, 4 have the same image resolution, so they are suitable for a comparison of the performance of the SVM classification. To test the generalisability of the inference methodology, the samples of each brain become in turn the training set, with the samples of the other brain used for testing. This evaluates how well a model trained on one brain generalises to a different brain.

Thirdly, using the DTI samples from three brains: the samples of two brains are used as a training set, while the samples of the other brain are used as a testing set. This evaluates how well a model trained on multiple brains generalises to a further brain.

In cases 2 and 3, different brains are used in a combinational manner, as the training and the testing sets. More details are given in the following sections.

6.2 Selection of samples

A DT-MR dataset of the human brain can be used to collect some samples to study. In this study, a sample is defined as a grid of $3 \times 3 \times 3$, having 27 tensors. The samples are chosen for machine learning and classification.

After a visual inspection of the DT-MR images, slice by slice, the region of interest (ROI) is defined. The ROI is mainly in the deep brain. In brain anatomy, the surface layer of the brain is known as the cortex, where the grey matter and the cerebral fluid appear as spherical tensors in DT-MR images. Some short U-shaped white matter fibres may exist in the cortex. Within the ROI, DT-MR images are used for computer labelling. The labelling method is described in section 5.5.2.

For example, given that the ROI in the 3 DT-MR images has $45 \times 54 \times 3$ voxels, 15×18 samples can be produced. They are semi-automatically labelled as fibre or non-fibre (the background) based on the criteria. “Non-fibre” here means that there are no coherence fibres in the sample.

The criteria of sample labelling are described in Chapter 5. They involve the calculation of the fractional anisotropy (FA) value [9], the Westin index [74], C_l , indicating the degree of a linear tensor shape, and the variance of angles of the principal eigenvectors within the DTI samples.

To calculate the variance of angles in a sample, the average principal eigenvector of the 27 tensors is first computed. The angle of two tensors is considered to be between 0 and 90 degrees. For every tensor, its principal eigenvector, P , about the mean principal eigenvector, M , is also computed. Sometimes, the sign of the principal eigenvector needs flipping if $P \times M < 0$. This is because the eigenvector could point in the opposite direction.

Figure 6.1 shows the characteristics of the samples of dataset5; each point shown in the figure is: (a) the mean FA values of a sample; (b) the mean Westin index, or C_l values; and (c) the mean variance angle values. These figures display a distinctive two-part pattern, indicating they are separable.

Based on the label map (e.g. Figure 5.1(a)), “fibre” samples are selected in a bottom-to-top order; and then the “non-fibre” samples are chosen from the background. In fact, no particular order is required. The sample set is arranged as the first half consisting of the “fibre” samples, while the second half are the “non-fibre” samples, both halves have the same number of samples.

6.3 Training of SVM models

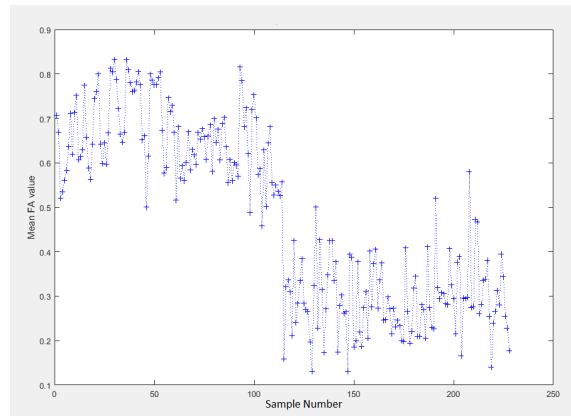
The training of SVM models is used to build a useful classifier for the prediction of classes for new data. The training is based on the DTI training set. Ten-fold cross validation is performed to estimate the parameters for building the best model. The objectives are: (a) to examine the classification accuracy and the robustness of the SVM models, measured by the misclassification rate during ten-fold cross validation; (b) to test to what extent the trained SVM models can be used to predict new instances (classes) in unseen data.

The validation process is divided into two stages: 1. training the SVM model; 2. testing the model on the unseen data.

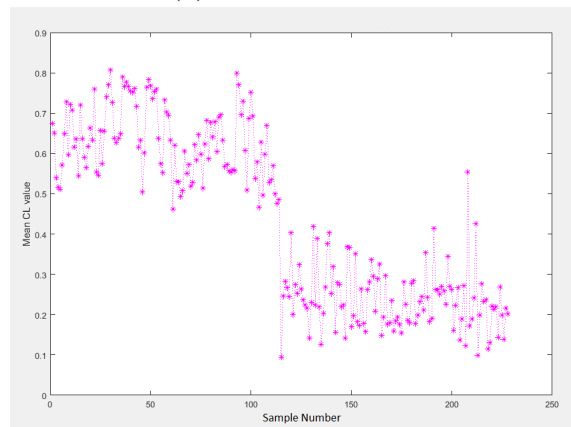
6.3.1 Choosing parameters

Training an SVM model is used to find the optimal parameters from the SVM algorithm which enable new data to be classified. The principles of the SVM are described in section 4.1.10.

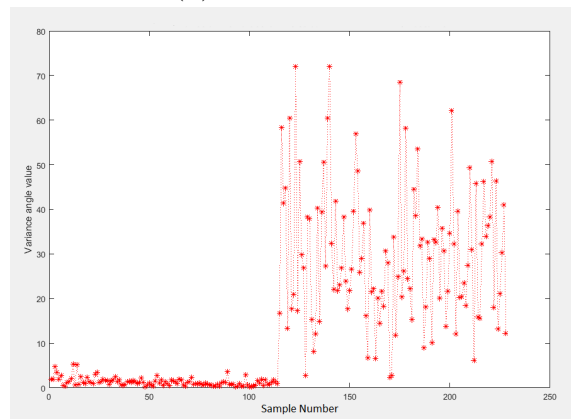
There are 3 parameters to be chosen: (i) the box constraint called C



(a) Mean FA values



(b) Mean C_l values



(c) Mean variance angle values

Figure 6.1: The characteristics of the samples from dataset5. The mean FA, mean C_l , and mean variance angle values of each sample are represented by the points.

value, for computing the margin of the SVM model; (ii) the number of best features, BFs ; and (iii) the K value, for computing the graph edge weight.

When training the SVM model, all the feature data points are first standardised, and then mapped onto the low dimension space using the Gaussian kernel. A set of BFs , K and C parameters is chosen in a combinational manner from the follows: the BFs are 1, 2, 3,... 12; the K values are 0.15, 0.16, 0.17, ... 0.24; and the C values are chosen to be exponential: 0.01, 0.03, 0.05, 0.1, 0.2, 0.5, 1.0, 5.0, 8.0 and 10.0. These numbers are decided experimentally.

During the ten-fold evaluation, 10 misclassification accuracy rates are computed, and the corresponding parameters used are recorded. By finding the minimum misclassification rate, the parameters used are considered as the optimal parameters.

In Figure 6.2, the parameters BF and K are shown with error bars; these parameters are used to produce the ESP feature matrix. Seven features at the top-left and $K=0.22$ at the top-right are on the lowest points of the curves, suggesting that they can produce the lowest misclassification rates. At the bottom, the 7th C value also produces the lowest misclassification. Thus they are considered as the optimal parameters.

Figures 6.2 - 6.5 display the parameter curves and their neighbourhood; different metrics and measures are adopted. Among them the misclassification rates in Figure 6.5 are the lowest (the mean values are less than 0.1), for which the heuristic method is used. Noticeably, the error bars are very short, meaning that the range of the misclassification rates is very small. Figure 6.5 shows the SVM classifier is robust and stable with the heuristic method.

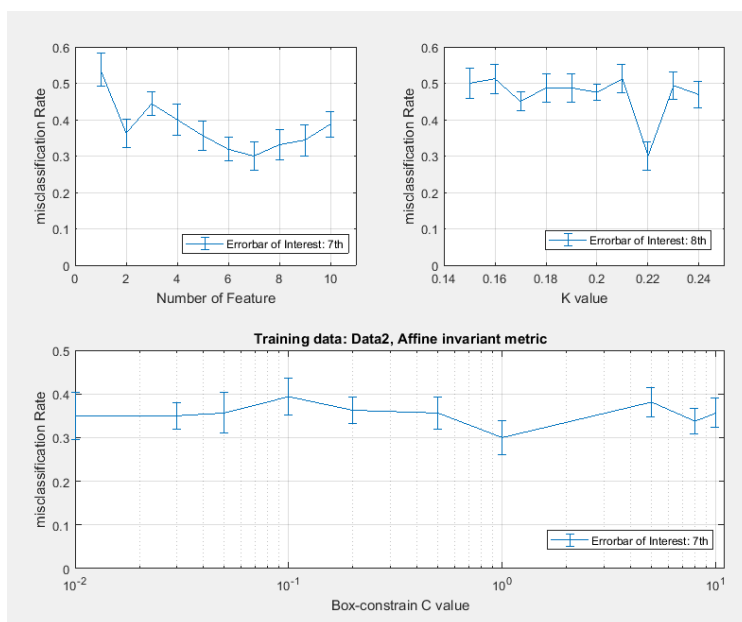


Figure 6.2: Choosing parameters with affine invariant metric. Dataset2.

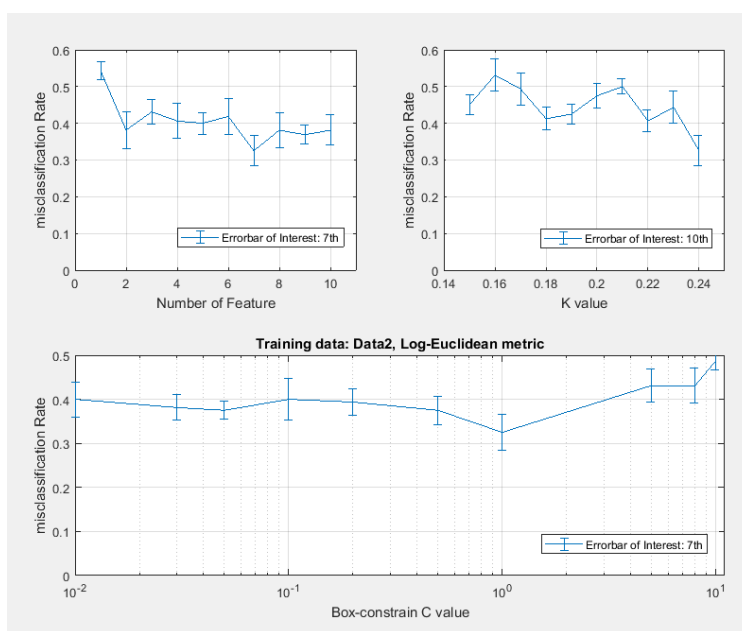


Figure 6.3: Choosing parameters with Log-Euclidean metric. Dataset2.

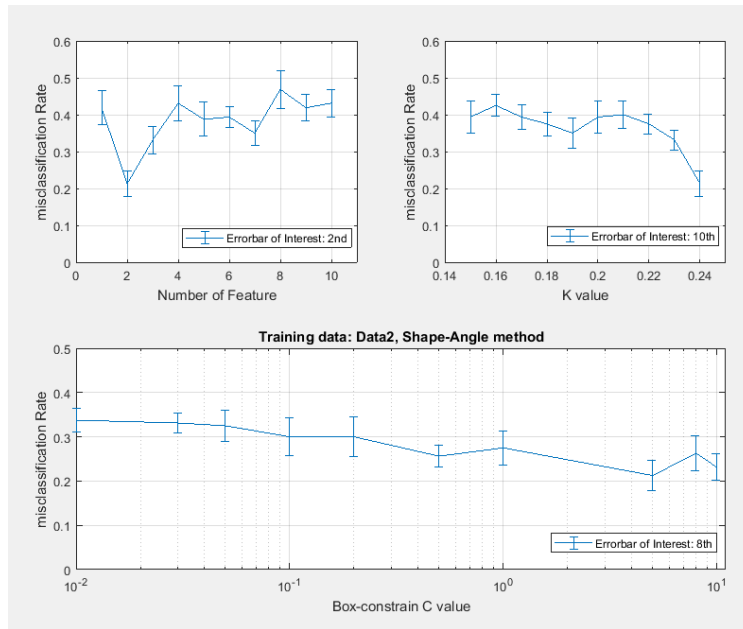


Figure 6.4: Choosing parameters with Shape-Angle measure. Dataset2.

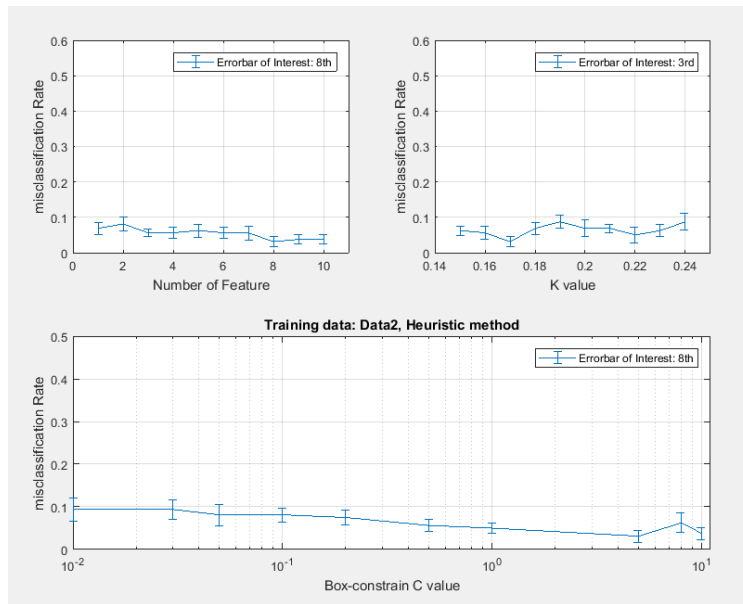


Figure 6.5: Choosing parameters with Heuristic method. Dataset2.

6.3.2 Ten-fold cross validation

At the training phase, ten-fold cross validation is used to examine the robustness of the SVM and to find the best parameters (Figure 6.6). The testing phase is described in section 6.4.

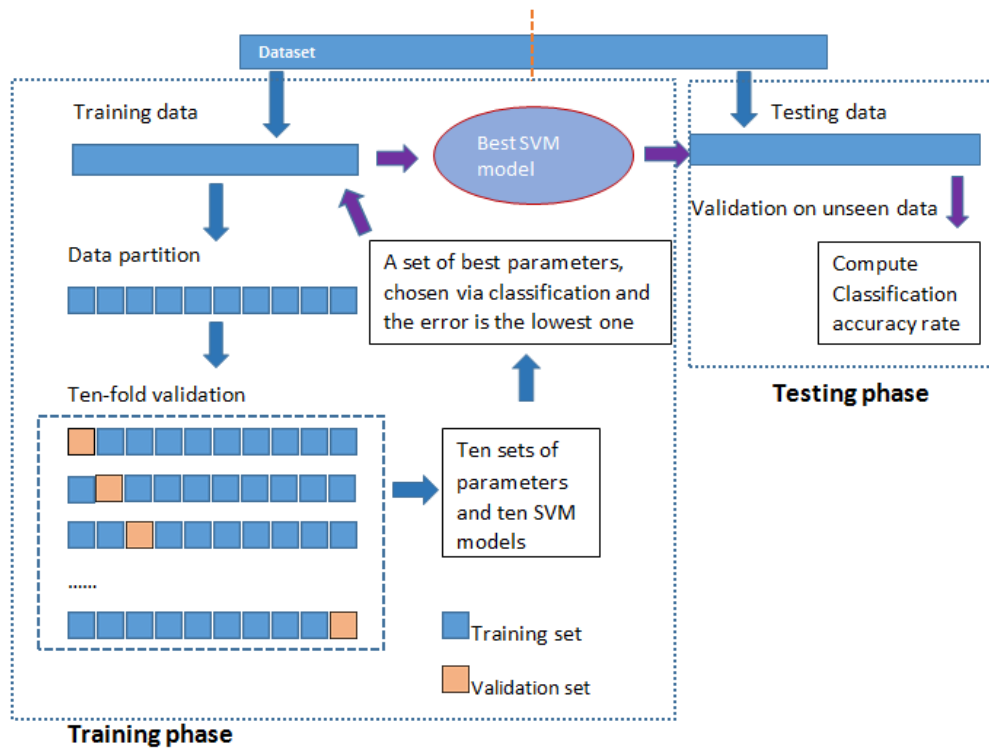


Figure 6.6: A diagram of ten-fold cross validation. It shows two phases: training and testing. The dataset is divided into training data and testing data. Training is to select the best parameter set through ten-fold validation, using the training data only. The best parameter set is then applied to the training data to produce an optimal SVM model, which is applied to the unseen data to compute a classification accuracy rate.

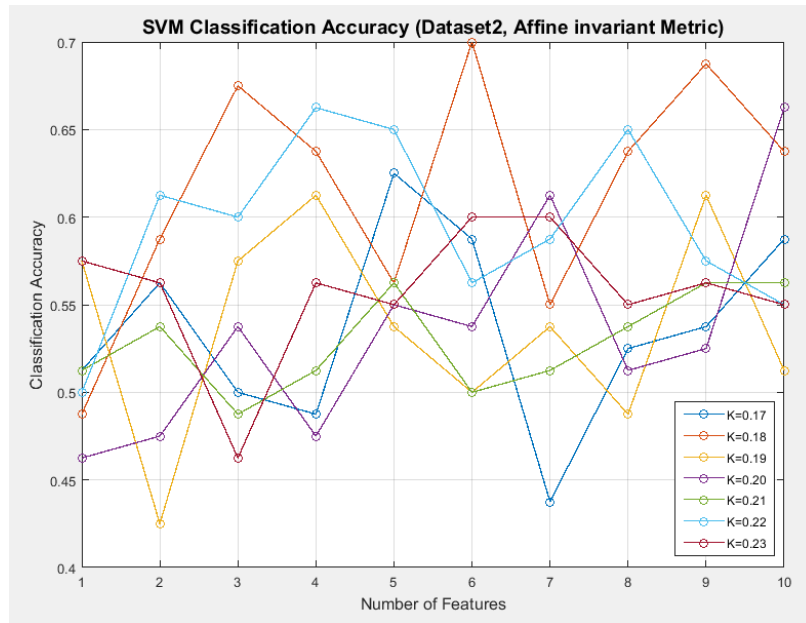
For example, 160 samples of Dataset2 are used in a ten-fold validation. The dataset is equally divided into 10 portions. In each fold, 9 portions

are randomly selected for training a SVM classifier, while the other portion is used for validation. This is performed in a rotation fashion, giving 10 estimates for the model parameter values. The parameters achieving the best classification results are considered to be the best parameters.

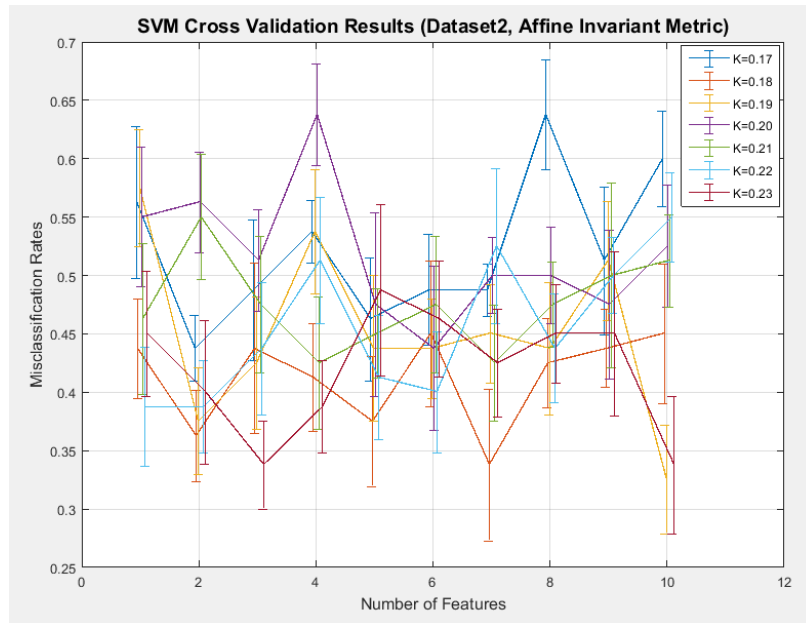
Figures 6.7 - 6.10 show the results of the SVM training. For example, in Figure 6.7(a) different coloured curves represent different K values used for tensor distance measures, which affects the graph edge weight. The classification accuracy rates vary with the different number of features used. The affine invariant metric is used to compute the geodesic distance of the tensors.

Figure 6.7(b) shows vertical lines with colours representing different K values. The two horizontal short bars at the ends of the vertical line indicate the highest and the lowest misclassification rates. This bar is called an error bar. In a ten-fold evaluation, with a given amount of feature(s), 10 misclassification rates are computed and represented as an error bar. The shorter an error bar is, the less spread out the errors, hence the more robust the SVM model. These figures assist with the choice of parameters. We ideally look for a small number of features that can produce the low misclassification rate, and the SVM is robust enough. In this example, 3 best features and $K=0.23$ are good parameters.

To compute the geodesic distance of the tensors, four different similarity measures are adopted: the affine invariant metric, the Log-Euclidean metric, the shape-angle measure and the heuristic method. Comparing Figures 6.7 - 6.10, we can see that the heuristic method achieves the lowest misclassification rates in training, and the highest classification accuracy rate in testing. These are desirable outcomes.

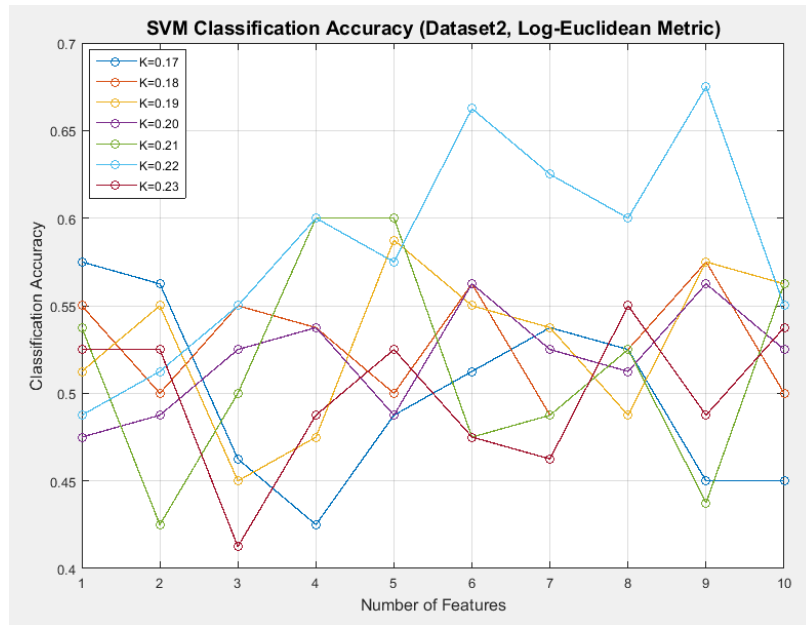


(a) Classification accuracy

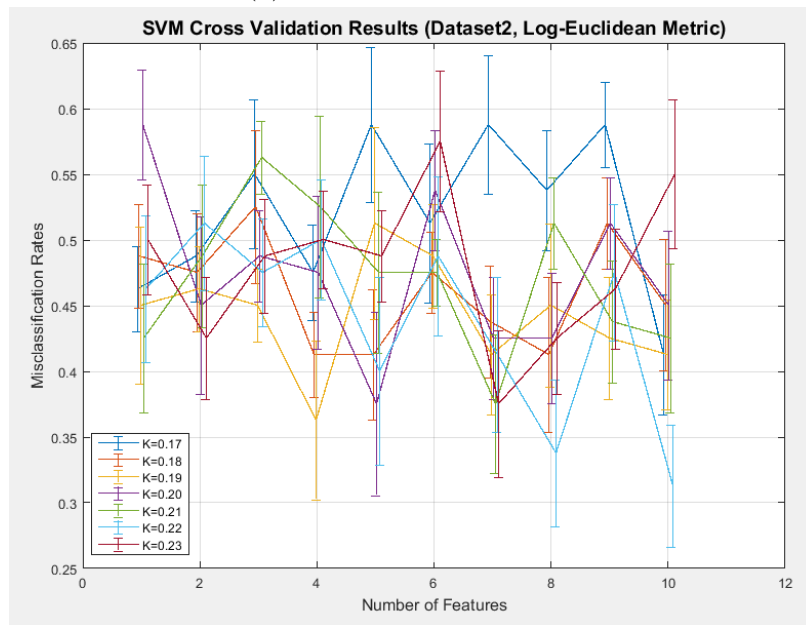


(b) Misclassification rates

Figure 6.7: Ten-fold cross validation in SVM training: the affine invariant metric is used for tensor distance measure. 1 to 10 leading features are used respectively.

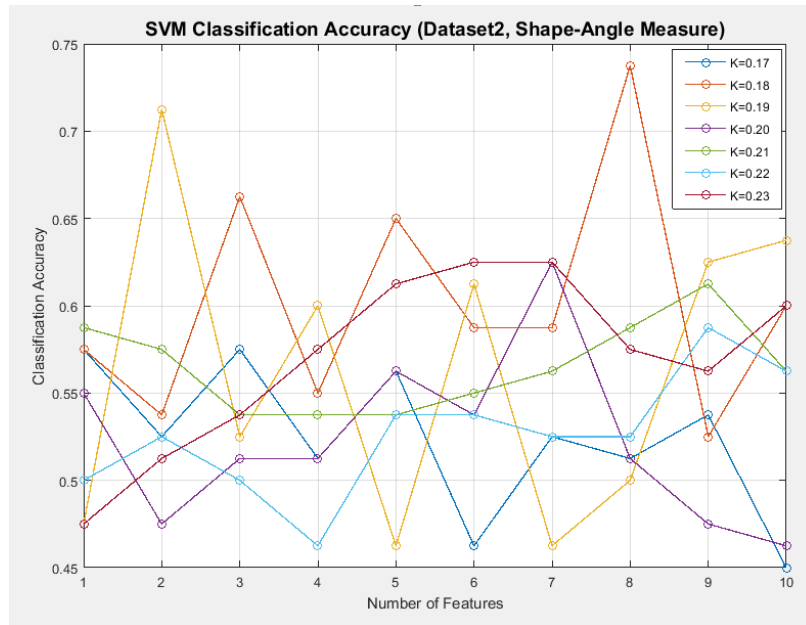


(a) Classification accuracy

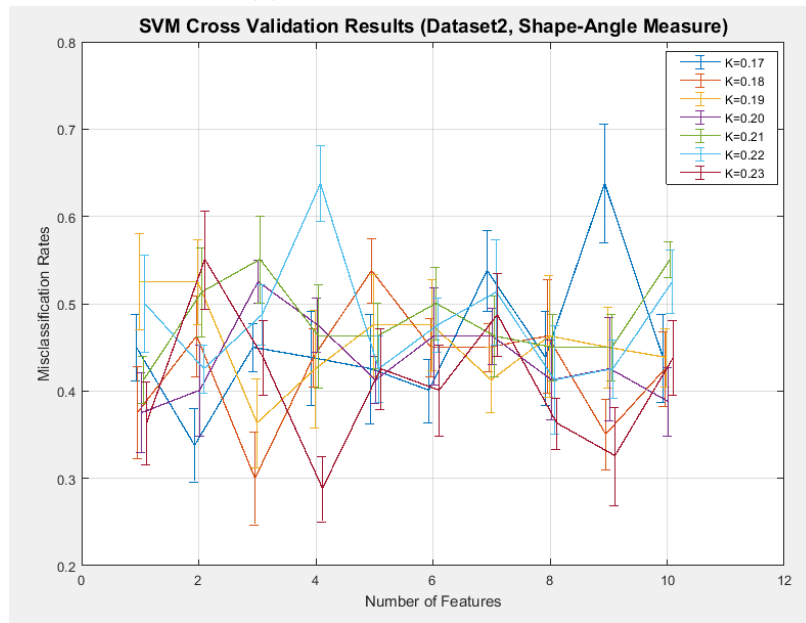


(b) Misclassification rates

Figure 6.8: Ten-fold cross validation in SVM training: the Log-Euclidean metric is used for tensor distance measure. 1 to 10 leading features are used respectively.

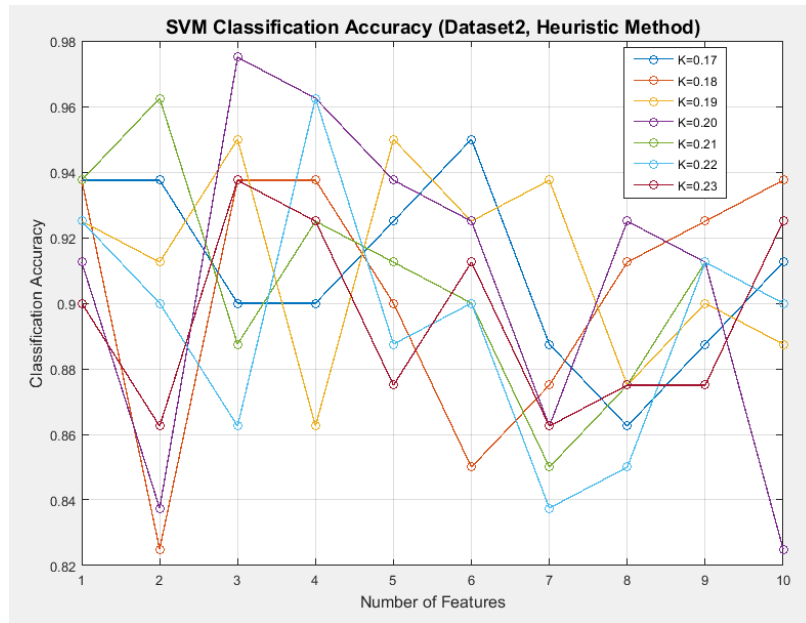


(a) Classification accuracy

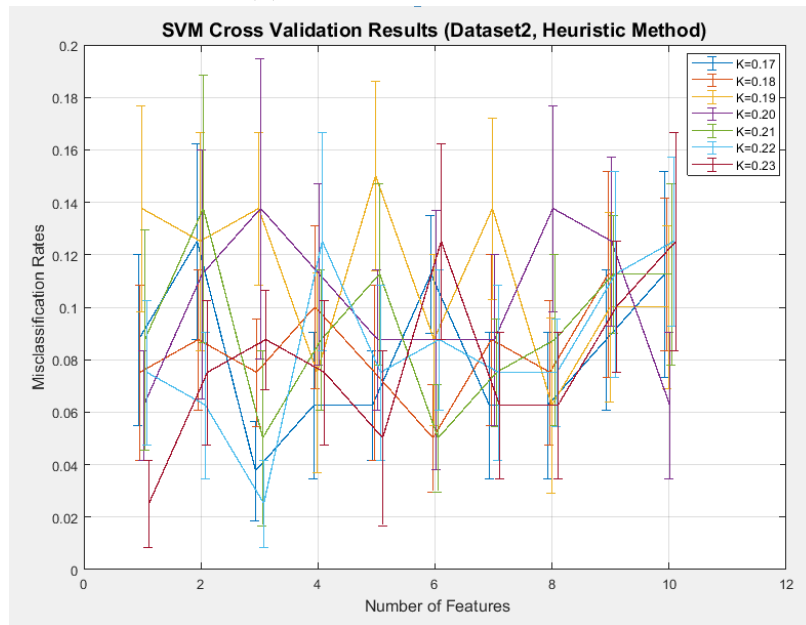


(b) Misclassification rates

Figure 6.9: Ten-fold cross validation in SVM training: the shape-angle measure is used for tensor distance measure. 1 to 10 leading features are used respectively.



(a) Classification accuracy



(b) Misclassification rates

Figure 6.10: Ten-fold cross validation in SVM training: the heuristic method is used for tensor distance measure. 1 to 10 leading features are used respectively.

6.4 Testing of SVMs on the unseen data

As mentioned, DTI samples are divided evenly for training and testing. After training an SVM model, it is tested to examine its performance, e.g. classification accuracy.

Ten-fold cross validation is done on training set only, resulting in a set of optimal parameters; and class posterior probabilities are estimated. Based on the likelihood measures and the Bayes rule, the SVM model uses the best parameters to predict new labels on the unseen data (Figure 6.6).

The classification results are displayed in Table 6.2 to Table 6.15. Classification accuracy rate, false negative rate (FNR) and false positive rate (FPR) are computed, as defined in section 3.6.1. In the one-brain case, random selection for both the training and testing sets is performed, 30 runs are carried out and average classification results are produced.

$$\text{Classification accuracy rate} = \frac{\text{Number-of-correctly-predicted-labels}}{\text{Number-of-known-labels}}$$

To examine the generalisability of the SVM model to the unseen data, a classification error is computed by

$$\text{Misclassification rate} = 1 - \text{Classification accuracy rate.}$$

6.5 Experimental methods

There are 3 cases in the experiments: called one-brain case, two-brain case or three-brain case, meaning that the DTI samples used for fibre classification are selected from one brain, two brains and three brains respectively. In each case, four different similarity measures are used to compute the geodesic distance of pairwise tensors. They are the affine invariant met-

ric, the Log-Euclidean metric, the proposed shape-angle measure and the heuristic method.

The trained SVM model is applied to the testing set and new labels are predicted. A classification accuracy (or misclassification) rate is computed. The evaluation results are presented in the following section.

(1) **One-brain case**

The Datasets 1 - 5 are used for the experiments. They produce 80, 160, 160, 148 and 228 DTI samples respectively. In each experiment, a dataset covering the whole brain is used for both training a SVM model and testing the model. 50% of the sample are randomly selected for training, while the other 50% of the samples are used for testing. 30 runs are completed.

(2) **Two-brain case**

The assessment process is the same as that of the one-brain case. However, the training set and the testing set used are acquired from different brains: the samples from one brain are used for training a model, while the samples from another brain are used for testing the model.

Datasets 2, 3, 4 having the same image resolution of $2.0 \times 2.0 \times 2.0 \text{ mm}^3$ are used for this experiment, with different combinations. There are 6 assessments: dataset2 is for training while dataset3 is for testing, and vice versa; dataset2 is for training while dataset4 is for testing, and vice versa; or dataset3 is for training while dataset4 is for testing, and vice versa.

(3) **Three-brain case**

The samples from DTI datasets of two brains are merged into one training set, while that of the other brain becomes the testing set. For datasets 2, 3, 4, all the combinations are considered when constructing a training set and

a testing set. This means: the datasets 2, 3 are merged for training while dataset4 is for testing; datasets 2, 4 are merged for training while dataset3 is for testing; datasets 3, 4 are merged for training while dataset2 is for testing.

6.6 Results

The SVM classification results are presented in Tables 6.2 - 6.15. The DTI datasets used are derived from real diffusion-weighted MR images of the human brains. Four different similarity measures are applied for computing the tensor distance, which is used to compute the graph edge weight.

For the one-brain case, 30 runs are conducted. The mean classification accuracy rate, mean false negative rate, mean false positive rate, and their standard deviations are computed. The results are displayed in Tables 6.2 - 6.6.

For the two-brain case, the samples from the dataset of one brain are used for training, and the samples from that of the other brain are used for testing. Tables 6.7 - 6.15 consist of two parts: the upper part displays the training results: the mean accuracy rate, the standard error, and the best parameters; while the lower part displays the classification outcomes of the testing phase.

For the three-brain case, the samples from DTI datasets of two brains are merged together for training, while the samples from that of the other brain are used for testing. The results are shown in Tables 6.13 - 6.15.

Classification Results				
Similarity Measure	Affine Invariant	Log-Euclidean	Shape-Angle	Heuristic
Mean accuracy	0.5092	0.4892	0.5475	0.7900
SD of accuracy	0.1047	0.0960	0.0887	0.0684
Mean FN	0.5317	0.61	0.3667	0.2217
SD of FN	0.2291	0.1940	0.2361	0.1448
Mean FP	0.4500	0.4117	0.5383	0.1983
SD of FP	0.2403	0.1879	0.2735	0.1118

Table 6.2: **One-Brain Case 1:** SVM training and testing both using Dataset1 (50% samples for each.); 30 runs in total.

Classification Results				
Similarity Measure	Affine Invariant	Log-Euclidean	Shape-Angle	Heuristic
Mean accuracy	0.5000	0.5054	0.5479	0.7517
SD of accuracy	0.0637	0.0563	0.0732	0.1455
Mean FN	0.4342	0.3292	0.5100	0.2608
SD of FN	0.3255	0.2981	0.3065	0.2928
Mean FP	0.5658	0.6600	0.3942	0.2358
SD of FP	0.3061	0.2964	0.2733	0.2205

Table 6.3: **One-Brain Case 2:** SVM training and testing both using Dataset2 (50% of samples for each.); 30 runs in total.

Classification Results				
Similarity Measure	Affine Invariant	Log-Euclidean	Shape-Angle	Heuristic
Mean accuracy	0.5363	0.5563	0.521	0.7675
SD of accuracy	0.0734	0.0883	0.0603	0.1109
Mean FN	0.4750	0.4258	0.5008	0.1633
SD of FN	0.3232	0.2749	0.4159	0.1508
Mean FP	0.4525	0.4617	0.4950	0.3017
SD of FP	0.2835	0.2586	0.4229	0.2796

Table 6.4: **One-Brain Case 3:** SVM training and testing both using Dataset3 (50% of samples for each.); 30 runs in total.

Classification Results				
Similarity Measure	Affine Invariant	Log-Euclidean	Shape-Angle	Heuristic
Mean accuracy	0.5207	0.5360	0.5419	0.7730
SD of accuracy	0.0444	0.0620	0.0610	0.1203
Mean FN	0.4793	0.2514	0.1505	0.2432
SD of FN	0.4186	0.3427	0.2033	0.2271
Mean FP	0.4793	0.6766	0.7658	0.2108
SD of FP	0.4238	0.3671	0.2715	0.2497

Table 6.5: **One-Brain Case 4:** SVM training and testing both using Dataset4 (50% of samples for each.); 30 runs in total.

Classification Results				
Similarity Measure	Affine Invariant	Log-Euclidean	Shape-Angle	Heuristic
Mean accuracy	0.5067	0.5167	0.5126	0.6468
SD of accuracy	0.0310	0.0442	0.0427	0.0838
Mean FN	0.2099	0.2158	0.5357	0.2474
SD of FN	0.2262	0.2352	0.3345	0.2360
Mean FP	0.7766	0.7509	0.4392	0.4591
SD of FP	0.2431	0.2623	0.3207	0.2825

Table 6.6: **One-Brain Case 5:** SVM training and testing both using Dataset5 (50% of samples for each.); 30 runs in total.

SVM Training Results				
Similarity Measure	Affine Invariant	Log-Euclidean	Shape-Angle	Heuristic
Mean accuracy	0.700	0.6750	0.7875	0.9687
Standard error	0.0382	0.0415	0.0340	0.0140
Best K	0.22	0.24	0.24	0.17
No.of BestFeatures	7	7	2	8
Best C	1	1	5	5
Classification Results				
Similarity Measure	Affine Invariant	Log-Euclidean	Shape-Angle	Heuristic
Accuracy rate	0.4932	0.5068	0.5608	0.8378
False negative	0.4324	0.0135	0.2297	0.1486
False positive	0.5811	0.9730	0.6486	0.1757

Table 6.7: **Two-Brain Case 1:** SVM training using the samples from Dataset2; testing on the samples from Dataset3.

SVM Training Results				
Similarity Measure	Affine Invariant	Log-Euclidean	Shape-Angle	Heuristic
Mean accuracy	0.7062	0.6687	0.6812	0.9687
Standard error	0.0476	0.0373	0.0237	0.0104
Best K	0.22	0.24	0.23	0.17
No.of BestFeatures	6	8	10	9
Best C	1	0.2	1	8
Classification Results				
Similarity Measure	Affine Invariant	Log-Euclidean	Shape-Angle	Heuristic
Accuracy rate	0.6067	0.5067	0.5000	0.8667
False negative	0.24	0	1	0.16
False positive	0.5467	0.9867	0	0.1067

Table 6.8: **Two-Brain Case 2:** SVM training using the samples from Dataset2; testing on the samples from Dataset4.

SVM Training Results				
Similarity Measure	Affine Invariant	Log-Euclidean	Shape-Angle	Heuristic
Mean accuracy	0.7181	0.7090	0.6881	0.9052
Standard error	0.0556	0.048	0.0331	0.0307
Best K	0.19	0.23	0.18	0.16
No.of BestFeatures	4	10	8	2
Best C	5	1	10	1
Classification Results				
Similarity Measure	Affine Invariant	Log-Euclidean	Shape-Angle	Heuristic
Accuracy rate	0.5467	0.5467	0.5	0.8667
False negative	0.44	0.2933	1	0.1867
False positive	0.4667	0.6133	0	0.08

Table 6.9: **Two-Brain Case 3:** SVM training using the samples from Dataset3; testing on the samples from Dataset4.

SVM Training Results				
Similarity Measure	Affine Invariant	Log-Euclidean	Shape-Angle	Heuristic
Mean accuracy	0.6562	0.725	0.6937	0.9187
Standard error	0.0477	0.0312	0.0218	0.0163
Best K	0.18	0.21	0.22	0.22
No.of BestFeatures	4	6	9	5
Best C	0.5	0.5	1	5
Classification Results				
Similarity Measure	Affine Invariant	Log-Euclidean	Shape-Angle	Heuristic
Accuracy rate	0.4875	0.5125	0.5188	0.8000
False negative	0.1875	0.2625	0.0125	0.0125
False positive	0.8375	0.7125	0.95	0.3875

Table 6.10: **Two-Brain Case 4:** SVM training using the samples from Dataset3; testing on the samples from Dataset2.

SVM Training Results				
Similarity Measure	Affine Invariant	Log-Euclidean	Shape-Angle	Heuristic
Mean accuracy	0.7467	0.7467	0.6933	0.9200
Standard error	0.0239	0.0239	0.0374	0.0166
Best K	0.21	0.18	0.23	0.15
No.of BestFeatures	7	10	1	8
Best C	5	10	0.05	1
Classification Results				
Similarity Measure	Affine Invariant	Log-Euclidean	Shape-Angle	Heuristic
Accuracy rate	0.5000	0.4875	0.5375	0.925
False negative	1.000	0.8750	0.8750	0.0625
False positive	0	0.1500	0.0500	0.088

Table 6.11: **Two-Brain Case 5:** SVM training using the samples from Dataset4; testing on the samples from Dataset2.

SVM Training Results				
Similarity Measure	Affine Invariant	Log-Euclidean	Shape-Angle	Heuristic
Mean accuracy	0.7533	0.7533	0.7267	0.9267
Standard error	0.0315	0.0299	0.0336	0.0185
Best K	0.21	0.18	0.18	0.15
No.of BestFeatures	6	7	6	8
Best C	8	1	1	5
Classification Results				
Similarity Measure	Affine Invariant	Log-Euclidean	Shape-Angle	Heuristic
Accuracy rate	0.5000	0.5000	0.5875	0.8375
False negative	0	0.0375	0.2750	0.1875
False positive	1.0000	0.9625	0.5500	0.1375

Table 6.12: **Two-Brain Case 6:** SVM training using the samples from Dataset4; testing on the samples from Dataset3.

SVM Training Results				
Similarity Measure	Affine Invariant	Log-Euclidean	Shape-Angle	Heuristic
Mean accuracy	0.6395	0.6492	0.6820	0.9223
Standard error	0.0284	0.0194	0.0231	0.0174
Best K	0.22	0.23	0.23	0.17
No.of BestFeatures	10	7	10	3
Best C	0.5	5	1	10
Classification Results				
Similarity Measure	Affine Invariant	Log-Euclidean	Shape-Angle	Heuristic
Accuracy rate	0.5733	0.5067	0.5600	0.8600
False negative	0.4	0.0133	0.36	0.0933
False positive	0.4533	0.9733	0.52	0.1867

Table 6.13: **Three-Brain Case 1:** SVM training using the samples from Dataset2 and Dataset3; testing on the sample from Dataset4.

SVM Training Results				
Similarity Metrics	Affine Invariant	Log-Euclidean	Shape-Angle	Heuristic
Mean accuracy	0.6516	0.6484	0.6677	0.9355
Standard error	0.00271	0.0148	0.0373	0.0167
Best K	0.2	0.17	0.23	0.15
No.of BestFeatures	7	11	10	6
Best C	1	0.03	1	10
Classification Results				
Similarity Measure	Affine Invariant	Log-Euclidean	Shape-Angle	Heuristic
Accuracy rate	0.5878	0.5676	0.5405	0.8446
False negative	0.4324	0.3649	0.7027	0.2297
False positive	0.3919	0.5	0.2162	0.0811

Table 6.14: **Three-Brain Case 2:** SVM training using the samples from Dataset2 and Dataset4; testing on the sample from Dataset3.

SVM Training Results				
Similarity Metrics	Affine Invariant	Log-Euclidean	Shape-Angle	Heuristic
Mean accuracy	0.6968	0.7032	0.6516	0.9097
Standard error	0.0211	0.0292	0.0258	0.0151
Best K	0.2	0.19	0.22	0.15
No.of BestFeatures	7	10	6	3
Best C	10	1	1	1

Classification Results				
Similarity Measure	Affine Invariant	Log-Euclidean	Shape-Angle	Heuristic
Accuracy rate	0.4688	0.4250	0.5625	0.9313
False negative	0.3750	0.4375	0.2375	0.0625
False positive	0.6875	0.7125	0.6375	0.0750

Table 6.15: **Three-Brain Case 3:** SVM training using the samples from Dataset3 and Dataset4; testing on the sample from Dataset2

6.7 Summary

Tables 6.2-6.15 show that our proposed heuristic method consistently outperforms the other measures used; a high prediction rate (around 86%) is achieved.

As the similarity measure, two Riemannian metrics and two proposed measures are applied to compute the geodesic distance of the pairwise or paired tensors. They are the affine invariant metrics, the Log-Euclidean metrics, the proposed shape-angle measure and the heuristic method. The heuristic method is the most suitable for the fibre inference.

The proposed heuristic method is associated with the affine-invariant metrics. It uses a selective criterion: if the angle between two tensors is below a threshold (e.g.10 degrees), then the angle itself becomes the geodesic distance of the tensors, otherwise the affine invariant metrics is used to compute the geodesic distance. This enables the graph edge weight to be more dis-

criminative. The weight determines the weighted Laplacian matrix of the data graph representing the DTI images. The weighted Laplacian matrix is used to produce the eigenvalues and eigenvectors, which are used to generate features. The features are the key to machine learning and fibre classification. This is the procedure of inferring the white matter fibres from diffusion MRI, also the procedure of methodological evaluation. If any error occurs, it could degrade the accuracy of the next step. In contrast, the affine invariant metric, the Log-Euclidean metric and the shape-angle measure do not work so well. The affine-invariant Riemannian metric was originally evaluated on synthetic data and it may not be applicable to real MR images.

The Log-Euclidean metric is computationally simpler than the affine invariant metric. However, it does not have all the properties that the affine-invariant Riemannian metric possesses. The Log-Euclidean metrics would show *tensor swelling effects*, because the determinant of the Euclidean mean of the tensors can be larger than that of the original tensors [2]. The affine-invariant and the Log-Euclidean metrics achieve similar classification results. The proposed heuristic method achieves the best classification results among them. The inference of the white matter fibres is non-trivial, particularly when the HARDI data are used, due to image noise, the partial volume effect and the complicated brain structures.

The quality of features plays a crucial part in the success of the neural fibre classification. They are associated with the geodesic distance metric or measure. Figure 6.11 shows that different metrics or measures can generate features of different characteristics. In Figure 6.11 (a),(b),(c) two-class features are inseparable, while in (d) they are separable and generated by the

proposed heuristic method.

The importance of these experiments is the use of real diffusion MR images, which is clinically relevant. Diffusion MR images are noisy and complicated, which can degrade the classification accuracy. Although the inference of the white matter fibers is challenging, this methodological evaluation provides strong supportive evidence for the framework of the inference of the white matter fibers from diffusion tensor MR images of the human brain.

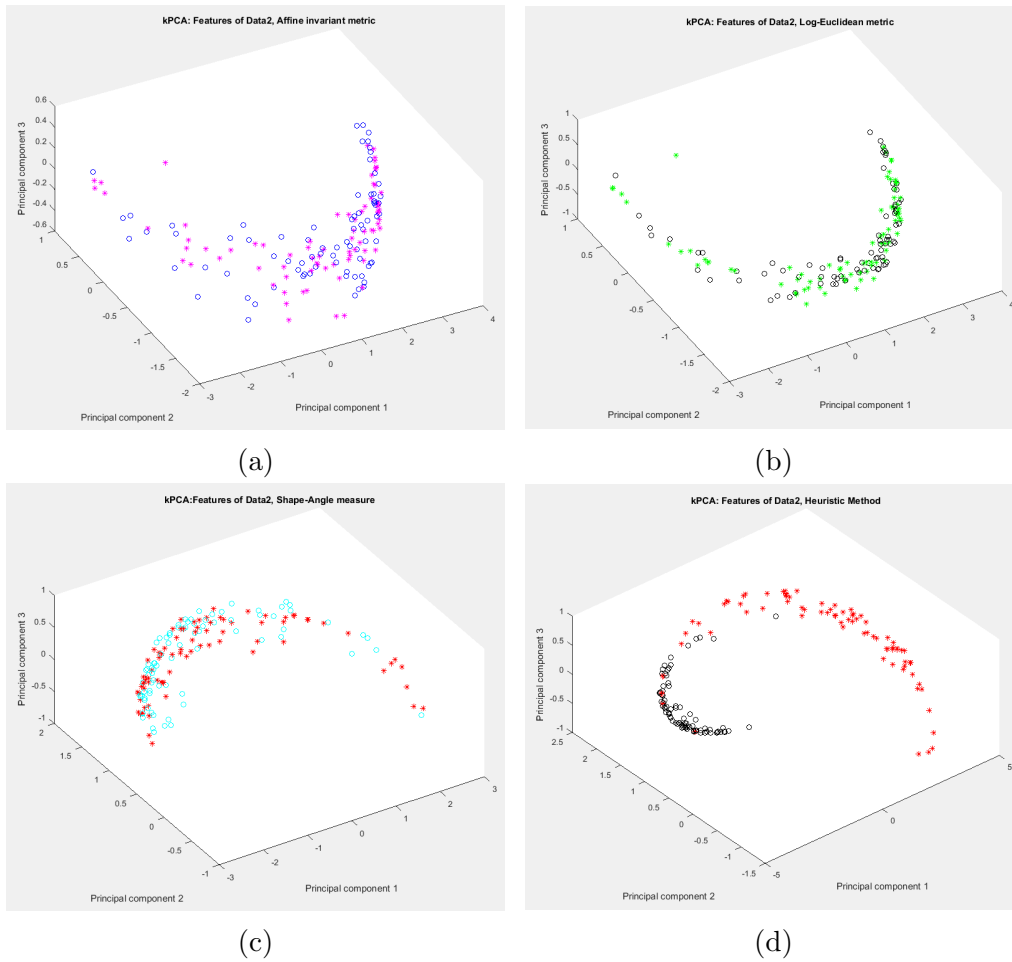


Figure 6.11: Features generated from the elementary symmetric polynomials, derived from spectral graph theory. Different measures are used to compute the graph edge weight. They are (a) affine invariant metric; (b) Log-Euclidean metric; (c) shape-angle measure; and (d) heuristic method. Kernel PCA [73] is used to condense the data and extract features. (d) shows that the feature points generated by using the heuristic method are much easier to be separated into two classes: fibre and non-fibre. (Dataset2)

Chapter 7

Conclusion and future work

Chapter 5 presents a framework for inferring white matter fibres in diffusion tensor images; and Chapter 6 describes the implementation of the framework in detail. Four measures are applied for the similarity measure, namely the affine invariant and Log-Euclidean metrics, and the proposed shape-angle measure and the heuristic method. Among them, the heuristic method significantly outperforms the other methods.

The similarity measure is crucial for labelling tensor samples. It affects the quality of feature extraction and feature selection. The classification results indicate that the features produced with the heuristic method have stronger discriminative power than using other distance measures. This is because the geodesic distance implies parallelism of prolate shaped tensors; alternatively, only when the variance of the principal eigenvectors of the tensors of a sample is small, can the sample be labelled as “fibre”. If the labelling of the samples is incorrect, the classification outcome will degrade. In short, the similarity measure is important to successful inference of the

white matter fibres.

The cerebral white matter fibres cannot be seen in diffusion MR images with the naked eye. Histologists have been using chemical dyes and/or dissection to isolate the white matter fibres from a cadaver’s brain. In this thesis, we identify the fibres in the live human brain through diffusion DT-MR images, statistical pattern recognition techniques and supervised machine learning. This is achieved by implementing the proposed framework and procedures, data transforming DWI to DTI, carrying out feature extraction and feature selection. Useful features are created for the classification of white matter fibres and their background in DTI.

The heuristic method significantly outperforms the other 3 similarity measure methods. It achieves excellent mean classification accuracy rates (with standard deviation) when 2 or 3 brains are used:

0.7458 ± 0.0570 (one-brain case, 5 tests; see Tables 6.2 - 6.6);

0.8556 ± 0.0419 (two-brain case, 6 tests; see Tables 6.7 - 6.12);

0.8786 ± 0.0463 (three-brain case, 3 tests; see Tables 6.13 - 6.15).

The heuristic method is used to compute the geodesic distance of a pair of tensors, which is for computing the graph edge weight later. When the angle is less than a threshold (e.g. 10 degrees), the angle is used as the similarity measure; otherwise the affine invariant metric is adopted. This approach is able to identify linear shaped tensors, which improves the accuracy of DTI sample labelling, leading to high classification accuracy.

The heuristic method successfully captures the fundamental aspect for machine learning: being able to produce discriminative features first. It

focuses on the similarity measure for computing the right graph weights; as a result, an appropriate label is given to a sample. However, it is difficult to find the ground truth. The classification results are largely based on the correctness of the labelling of the DTI samples. For this reason, the brain anatomy atlas is used to understand the labelling, for both confirmation and triangulation and experts in the York Neuroimaging Centre were consulted.

The work covering shape analysis for diffusion MRI images of the human brain is more challenging than that for structural MRI. Structural MRI data are 3 dimensional, while diffusion MRI data have 5 dimensions: each voxel is a 3×3 symmetric positive definite matrix. Structural MRI are scalar data, diffusion MRI data have both magnitudes and orientations. They can be used for inferencing the white matter fibers, which enables further studies of the brain connectivity.

The work presented in chapter 6 also shows the usefulness of graph representation; and the graph spectrum has a potential for the shape analysis of diffusion tensor images.

7.1 Summary of contributions

The contributions described in the thesis are:

- (1) Proposing a spectral graph based framework for inferring white matter fibres. This is successfully applied to diffusion tensor images, derived from real diffusion-weighted MR images, namely the High Angular Resolution Diffusion Imaging (HARDI) data.

- (2) Creating useful features from DT-MR images through the symmetric

elementary polynomial values and the spectral graph theory.

(3) Proposing a semi-automatic labelling system to select DTI samples, which are used for supervised machine learning.

(4) Proposing two methods for similarity measures: the heuristic method and the shape-angle measure. Both are for pairwise tensor distance measures. The former is very good, while the latter does not work well.

(5) With only a small number of diffusion tensor image datasets, an evaluation of the methodology for inferring white matter fibres is conducted successfully, and useful classification results are produced.

(6) Applying spectral graph theory to 5D diffusion tensor MR image analysis. With the heuristic method, feature selection and machine learning on Riemannian manifold, excellent fibre classification accuracy rates are achieved (around 86%).

(7) Feature selection techniques are successfully applied to diffusion MR images, and choosing the best features for the fibre inference, or fibre classification; only a small number of features are chosen (up to 10), so the search space for features is considerably reduced.

(8) Identifying the suitable SVM classifiers for DTI classification, together with the useful heuristic approach for feature similarity measure, excellent classification results for the white matter fibres are achieved.

(9) Obtaining excellent results of the sulci classification based on structural MRI analysis, with the combination of spectral graph theory and statistical machine learning. Useful features are extracted from the heat kernel signature and the zeta function trace.

(10) This study has proven that the Fisher discriminant ratio has a strong

discriminative power. It is useful not only for the sulci characterisation in structural MR images, but also for inferring white matter fibres from diffusion tensor images as the feature selection criterion.

7.2 The factors that could affect the inference of white matter fibres

There are a number of factors that could affect the inference of white matter fibres.

MR imaging bias: noise can be caused by the heterogeneous magnetic field, causing geometrical distortion of (diffusion) MR images, hampered by individual difference.

Image registration error: in this study, up to 288 MR image volumes are aligned to produce a single set of HARDI dataset. Due to physiological movement like breathing, the quality of imaging can be degraded and blurred.

Diffusion tensor measurement errors: usually, the FA value is lower than it should be in fibre crossing; conventional statistics is not naturally applicable to the tensors; and the choice of metric or measure is application dependent. These can cause tensor quantitative measurement errors. As a result, sample labelling might be affected.

Diffusion tensor modelling error: the tensor model is assumed to be a Gaussian model but in reality it is not; the model assumes at most one fibre exists in an image voxel but this may not be true, since the white matter fibre is only 5-10 μm in diameter, and the image voxel sizes of the datasets are 2.5mm^3 , 2.0mm^3 or 1.25mm^3 , which being much bigger than the fibre

diameter, could contain a large number of fibres.

Graph spectrum computing error: a $3 \times 3 \times 3$ sample is used to generate a graph and so the Laplacian matrix of the graph thus has a size of 27×27 . In the process of eigendecomposition, numerical errors could occur when computing the eigenvalues and eigenvectors, such as overflow or underflow, as their values are very small. This also can occur when performing the pseudo-inverse of a large (feature) data matrix.

Small sample size: the number of datasets is small; and the number of samples selected is also small. This could affect the SVM training result, as the variance of the classification accuracy in the ten-fold validation can fluctuate. In general, machine learning tends to use large datasets. However, HARDI acquisition can take a long time (around 1 hour), which can make the subject feel claustrophobic, and cause body motion inside the scanner, resulting in geometric distortion in MR images.

The datasets in the public domain might not always be suitable for fibre inference. For instance, the datasets might use different MR imaging sequences, different diffusion b -value and magnetic field strength.

Image resolution: Dataset5 comes from the website of the Human Connectome Project; the voxel size is 1.25 mm^3 . This is the highest diffusion image resolution used in this study. However, when the samples from DTI dataset5 are used for evaluation, in the one-brain case, the classification accuracy rate is only 64.68% (Table 6.6); while with samples from datasets 1-4, the classification accuracy rates are over 75%. This may be because the signal-to-noise ratio is low when the image resolution is high.

Shape analysis for diffusion MR images is non-trivial, particularly for brain structure detection. The white matter fibres cannot be detected directly, as they are invisible in both structural and diffusion MR images. They can be inferred through measuring water diffusion, but there is a limitation as mentioned above.

Nevertheless, this dissertation provides a novel graph based framework for inferring white matter fibres from DT-MR images. Although this is mathematically and technically challenging, the research outcomes are promising.

7.3 Future work

Based on the analysis in section 7.2, the future work is identified as improving all the aspects mentioned. These include improvements of the metrics of geodesic distance of the tensors, feature generation, feature selection, and finding more samples and more diffusion MR datasets.

To improve the metrics, both the characteristics of diffusion MR and the angular component of the data should be taken into account. For feature generation, different shape descriptors can be applied to diffusion tensor MR images, such as the heat kernel signature and the trace of zeta function. For feature selection, other methods can be used to reduce the feature nesting problem; and different selection criteria can be applied or invented.

We are excited by the new technical advances this thesis presents. Most importantly, the whole image processing and analysis pipeline is workable, and the novel methodology has been tested successfully on real diffusion MR images, particularly on HARDI data. The study proves a proposed heuristic

method works much better than the other existing similarity measures.

Diffusion MRI is a unique non-invasive brain imaging modality. The research outcomes are significant for diffusion MR image analysis. It is an important step forward for the inference of brain white matter fibres, which will certainly be beneficial for white matter pathological studies, such as psychiatric disorders and neurological diseases; and also for computer assisted neurosurgery in the future.

Appendices

Principal component analysis (PCA)

Principal component analysis (PCA) is a data projection method that is used for data reduction. It is an orthogonal transformation to convert a set of observation values of possibly correlated variables into a set of values of linearly uncorrelated variables, called principal components; and the first principal component has the largest possible variance [53].

Given a data matrix D with dimensions of $M \times N$, where M is data dimension and N is the number of observations or of samples, as a standard algorithm, the algorithm of PCA is:

1. Data centering: computing the mean for each column of the data, and subtract that mean from the each column value, resulting in a zero mean new data matrix U ;
2. Computing the covariance matrix of the new data matrix: $\Sigma = U^T U$;
3. Obtaining the eigenvalues and eigenvectors of the covariance matrix by eigendecomposition;
4. Sorting the columns of the covariance matrix, so that they correspond to the eigenvalues in a descending order. This create a projection matrix.

5. Using the projection matrix to project the original data onto a new subspace.

Bibliography

- [1] A.L. Alexander. Diffusion tensor imaging of the brain. *Neurotherapeutics*, 4(3):316–329, 2007.
- [2] V. Arsigny, P. Fillard, X. Pennec, and N. Ayache. Log-Euclidean metrics for fast and simply calculus on diffusion tensors. *Magnetic Resonance in Medicine*, 56:411, 2006.
- [3] M. Aubry, U. Schlickewei, and D. Cremers. The wave kernel signature: A quantum mechanical approach to shape analysis. *Technical report*, pages 1–8, 2011.
- [4] F. Aziz, R.C. Wilson, and E.R. Hancock. Graph characterisation using Gaussian wave packet signature. *SIMBAD 2013, LNCS*, 7953:176–189, 2013.
- [5] A. Barmpoutis, B. C. Vemuri, T.M. Shepherd, and J.R. Forder. Tensor splines for interpolation and approximation of DT – MRI with applications to segmentation of isolated rat hippocampi. *IEEE TMI: Transactions on Medical Imaging*, 26(11):1537–1546, 2007.

- [6] H.G. Barrow and R.J. Popplestone. Relational descriptions in picture processing. *Machine Intelligence*, 6:377–396, 1971.
- [7] P.J. Basser, J. Mattiello, and D.Le Bihan. MR diffusion tensor spectroscopy and imaging. *Biophysical Journal*, 66:259–267, 1994.
- [8] P.J. Basser and E. Ozarslan. Introduction to diffusion MRI. In *Diffusion MRI: From Quantitative Measurement to in vivo Neuroanatomy*, pages 3–9. Academic Press, 2009.
- [9] P.J. Basser and E. Ozarslan. Anisotropic diffusion: From the apparent diffusion coefficient to the apparent diffusion tensor. In *Diffusion MRI: Theory, Methods, and Applications*, pages 79–91. Oxford University Press, 2011.
- [10] M.F. Bear, B.W. Connors, and M.A. Paradiso. *Neuroscience: Exploring the brain*. Lippincott Williams and Wilkins, 2007.
- [11] T.E.J. Behrens, M.W. Woolrich, M. Jenkinson, H. Johnansen-Berg, R.G. Nunes, S. Clare, P.M. Matthews, J.M. Brady, and S.M. Smith. Characterisation and propagation of uncertainty in diffusion-weighted MR imaging. *Magnetic Resonance in Medicine*, 50(5):1077–1088, 2003.
- [12] P.J. Besl and N.D. McKay. A method for registration of 3-d shape. *IEEE Transactions on Pattern Analysis and Machine intelligence*, 14(2):239–256, 1992.
- [13] D.Le Bihan, J-F. Mangin, C. Poupon, C.A. Clark, S. Pappata, N. Molko, and H. Chabriat. MR diffusion tensor imaging: Concepts and applications. *Journal of Magnetic Resonance Imaging*, 13:534–546, 2001.

- [14] F. Bloch, W.W. Hansen, and M. Packad. Nuclear induction. *Physical Review*, 69:127, 1945.
- [15] R. Brown. A brief account of microscopical observations. *Philosophical magazine*, 4:161–173, 1828.
- [16] H.Y. Carr and E.M. Purcell. Effects of diffusion on free precession in nuclear magnetic resonance experiments. *Physical Review*, 94(3):630–638, 1954.
- [17] U. Castellani, P. Mirtuono, V. Murino, M. Bellani, G. Rambaldelli, M. Tansella, and P. Brambilla. A new shape diffusion descriptor for brain classification. *MICCAI 2011, Part II, LNCS*, 6892:426–433, 2011.
- [18] M. Catani. The functional anatomy of white matter: from postmortem dissections to in vivo virtual tractography. In *Diffusion MRI: Theory, Methods, and Applications*, pages 5–18. Oxford University Press, 2011.
- [19] A. Counce and C.J. Taylor. Building 3d sulcal models using local geometry. *Medical Image Analysis*, 5:69–80, 2001.
- [20] C.A. Cocosco, A.P. Zijdenbos, and A.C. Evans. A full automatic and robust brain MRI tissue classification method. *Medical Image Analysis*, 7(4):513–527, 2003.
- [21] T. F. Cootes, C. J. Taylor, D.H. Cooper, and J. Graham. Active shape models - their training and application. *Computer Vision and Image Understanding*, 61(1):38–59, 1995.

- [22] T.F. Cootes, C.J. Taylor, D.H. Cooper, and J. Graham. Training models of shape from sets of examples. *BMVC 1992*, pages 9–18, 1992.
- [23] A. Criminisi, D. Robertson, E. Konukoglu, J. Shtton, S. Pathak, S. White, and K. Siddiqui. Regression forests for efficient anatomy detection and localisation in computed tomography scans. *Medical Image Analysis*, 17:1293–1303, 2013.
- [24] T.J. Crow. Schizophrenia as a transcallosal misconnection syndrome. *Schizophrenia Research*, 30:111–114, 1998.
- [25] W.R. Crum. Spectral clustering and label fusion for 3D tissue classification: sensitivity and consistency analysis. *Annals of BMVA*, 2009(6):1–12, 2009.
- [26] P.A. Devijver and J. Kittler. *Pattern Recognition: A statistical approach*. Prentice Hall International, 1938.
- [27] D.Le Bihan. Magnetic resonance diffusion imaging: introduction and concepts. In *Diffusion MRI: Theory, Methods, and Applications*, pages 57–78. Oxford University Press, 2011.
- [28] D.Le Bihan. Diffusion MR: what water tell us about the brain. *EMBO Molecular Medicine*, 6(5):569–573, 2014.
- [29] D.Le Bihan, E. Breton, D. Lallemand, P. Grenier, E. Cabanis, and M. Laval-Jeantet. MR imaging of intravoxel incoherent motions: application to diffusion and perfusion in neurologic disorders. *Radiology*, 161(2):401–407, 1986.

- [30] M.P. Do Carmo. *Riemannian Geometry*. Birkhuser, 1992.
- [31] L. Euler. Solutio problematis ad geometriam situs pertinentis. *Commentarii academiae scientiarum Petropolitanae*, 8:128–140, 1736.
- [32] R.A. Fisher. The use of multiple measurements in taxonomic problems. *Annals of Eugenics*, 7:179–188, 1936.
- [33] P. Flach. *Machine Learning: The art and science of algorithms that make sense of data*. Cambridge University Press, 2012.
- [34] P.T. Fletcher, C. Lu, S. M. Pizer, and S. Joshi. Principal geodesic analysis for the study of nonlinear statistics of shape. *IEEE Transactions on Medical Imaging*, 23(8):995–1005, 2004.
- [35] K.J. Friston and C.D. Frith. Schizophrenia: A disconnection syndrome? *Clinical Neuroscience*, 3:89–97, 1995.
- [36] G. Galilei. *Dialogues concerning two new sciences*. Lodewijk Elzevir, 1638.
- [37] S.A. Huettel, A.W. Song, and G. McCarthy. *Functional Magnetic Resonance Imaging*. Sinanuer Associates, 2004.
- [38] M. Jenkinson, C.F. Beckmann, T.E. Behrens, M.W. Woolrich, and S.M. Smith. FSL. *NeuroImage*, 62:782–90, 2012.
- [39] B. Jeurissen. *Improved analysis of brain connectivity using high angular resolution diffusion MRI*. PhD thesis, University of Antwerpen, 2012.

- [40] D. G. Kendall. Shape manifolds, procrustean metrics, and complex projective spaces. *Bulltin of London Mathematics Sociaty*, 16:81–121, 1984.
- [41] E. Konukoglu, B. Glocker, D.Hye Ye, A. Criminisi, and K.M. Pohl. Discriminative segmentation-based evaluation through shape dissimilarity. *IEEE Transactions on Neural Networks*, 31(12):2278–2289, 2012.
- [42] P.C. Lauterbur. Image formation by induced local interaction: examples of employing nuclear magnetic resonance. *Nature*, 242:190–191, 1973.
- [43] A. Leemans. Visualization of diffusion MRI data. In *Diffusion MRI: Theory, Methods, and Applications*, pages 354–379. Oxford University Press, 2011.
- [44] C. Lenglet. *Geometric and variational methods for diffusion tensor MRI processing*. PhD thesis, University of Nice-Sophia Antipolis, 2006.
- [45] C. Lenglet, R. Deriche, and O. Faugeras. Inferring white matter geometry from diffusion tensor MRI: application to connectivity mapping. *LNCS 3024*, pages 127–140, 2004.
- [46] P. Mansfield. Multi-planar image formation using nmr spin echoes. *Journal of Physics. C: Solid state physics*, 10:55–58, 1977.
- [47] P. Mansfield. Human whole body line-scan imaging by NMR. *British Journal of Radiology*, 51:921–922, 1978.
- [48] B.D. McKay. Spanning trees in regular graphs. *Europ.J.Combinatorics*, 4:149–160, 1983.

- [49] M. Mesulam. The evolving landscape of human cortical connectivity: Facts and inferences. *NeuroImage*, 62:2182–2189, 2012.
- [50] T. Meynert. A clinical treatise on disease of the fore-brain based upon a study of its structure, function, and nutrition. *Trans. Bernard Sachs.*, pages 1–313, 1885.
- [51] S. Mori and P.C.M.Van Zijl. Fibre tracking: principles and strategies - a technical review. *NMR in Biomedicine*, 15(7-8):468–480, 2002.
- [52] M.E. Moseley, Y. Cohen, and Mintorovitch. Early detection of regional cerebral ischemic injury in cats: evaluation of diffusion and T2-weighted MRI and spectroscopy. *Magnetic resonance medicine*, 14:330–346, 1990.
- [53] K. Pearson. On lines and planes of closest fit to systems of points in space. *Philosophical Magazine*, 2:559–572, 1901.
- [54] X. Pennec and P. Fillard. *Statistical computing on non-linear spaces for computational anatomy*. Springer, 2015.
- [55] X. Pennec, P. Fillard, and N. Ayache. A Riemannian framework for tensor computing. *International Journal of Computer Vision*, 66(1):41–66, 2006.
- [56] E.M. Purcell, H.C. Torrey, and R.V. Pound. Resonance absorption by nuclear magnetic moments in a solid. *Physical Review*, 69:37–38, 1946.
- [57] J. Rademacher, V.S. Caviness, and H. Steinmetz. Topographical variation of the human primary cortices: implications for neuroimag-

- ing, brain mapping, and neurobiology. *Cerebral Cortex*, July/August 1993(3):313–329, 1993.
- [58] J.C. Reil. Das balken-system oder die hirnschenkel-organisation im groen gehirn. *Archiv fr die Physiologie*, 9:172–195, 1809.
- [59] P. Ren, R.C. Wilson, and E.R. Hancock. Graph characterisation via ihara coefficients. *IEEE Transactions on Neural Networks*, 22(2):233–245, 1992.
- [60] S. Rosenberg. *The Laplacian on a Riemannian Manifold: An introduction to analysis on manifolds*. Cambridge University Press, 1997.
- [61] S.L. Rossell, J. Shapleske, R. Fukuda, P. Wooddruff, A. Simmons, and A. S. David. Corpus callosum area and functioning in schizophrenic patients with auditory - verbal hallucinations. *Schizophrenia Research*, 50:9–17, 2001.
- [62] J. Shi and J. Malik. Normalised cuts and image segmentation. *IEEE Transactions on Pattern Analysis and Machine Intelligence*, 22(8):888–905, 2000.
- [63] W. Smith. *Statistical Methods for Facial Shape-from-Shading and Recognition*. PhD thesis, University of York, 2007.
- [64] E. Stejskal and J. Tanner. Spin diffusion measurements: Spin echoes in the presence of a time dependent field gradient. *The Journal of Chemical Physics*, 42:288–292, 1965.

- [65] J. Sun, M. Ovsjanikov, and L. Guibas. A concise and provably informative multi-scale signature based on heat diffusion. *Eurographics Symposium on Geometry Processing 2009*, pages 1383–1392, 2009.
- [66] D.G. Taylor and M.C. Bushell. The spatial mapping of translational diffusion coefficients by the NMR imaging technique. *Physics in medicine and Biology*, 30:345–349, 1985.
- [67] A. Tharwat, T. Gaber, A. Ibrahim, and A. Hassanien. Linear discriminant analysis: A detailed tutorial. *AI Communications*, 30(2):169–190, 2017.
- [68] J-D. Tournier, F. Calamante, and A. Connelly. Robust determination of the fibre orientation distribution in diffusion MRI: Non-negativity constrained super-resolved spherical deconvolution. *NeuroImage*, 35:1459–1472, 2007.
- [69] D.S. Tuch. Q-ball imaging. *Magnetic Resonance in Medicine*, 52:1358–1372, 2004.
- [70] D. C. Van Essen, K. Ugurbil, E. Auerbach, D. Barch, T.E J. Behrens, R. Bucholz, A. Chang, L. Chen, M. Corbetta, S. W. Curtiss, S. D. Penna, D. Feinberg, M. F. Glasser, N. Harel, A. C. Heath, L. Larson-Prior, D. Marcus, G. Michalareas, S. Moeller, R. Oostenveld, S. E. Petersen, F. Prior, B.L. Schlaggar, S. M. Smith, A.Z. Snyder, J. Xu, E. Yacoub, and WU-Minn HCP Consortium. The human connectome project: A data acquisition perspective. *NeuroImage*, 62:2222–2231, 2012.

- [71] V.N. Vapnik. *Statistical Learning Theory*. John Wiley and Sons INC, 1998.
- [72] M. T. Vlaardingerbroek and J.A. Boer. *Magnetic Resonance Imaging: Theory and Practice*. Springer - Verlag Berlin Heidelberg New York, 2003.
- [73] Q. Wang. Kernel principal component analysis and its applications in face recognition and active shape models. *arXiv*, 1207.3538:[cs.CV], 2012.
- [74] C.F. Westin, S.E. Maier, H. Nabavi, F.A. Jolesz, and R. Kikinis. Processing and visualisation for diffusion tensor imaging. *Medical Image Analysis*, 6(2):93–108, 2002.
- [75] L.E. White. Medical Neuroscience lecture course. Coursera. Online; accessed 1 October 2013.
- [76] R. C. Wilson. *Inexact Graph Matching using Symbolic Constraints*. PhD thesis, University of York, 1996.
- [77] R.C. Wilson, E.R. Hancock, and B. Lou. Pattern vectors from algebraic graph theory. *IEEE Transactions on Pattern Analysis and Machine Intelligence*, 27(7):1112–1124, 2005.
- [78] J. Wu. *Statistical approaches to gender classification in the surface normal domain*. PhD thesis, University of York, 2009.
- [79] B. Xiao, E.R. Hancock, and R.C. Wilson. Graph characteristics from the heat kernel trace. *Pattern Recognition*, 42:2589–2606, 2009.

- [80] F. Zhang. *Geometric and Probabilistic Methods for non-Euclidean Image Analysis*. PhD thesis, University of York, 2008.